Spring 2016

Quantitative confocal imaging of nanoporous silica

Yan Hu
University of Iowa

QUANTITATIVE CONFOCAL IMAGING OF NANOPOROUS SILICA

by

Yan Hu

A thesis submitted in partial fulfillment of the
requirements for the Doctor of Philosophy
degree in Chemistry in the
Graduate College of The
University of Iowa

May 2016

Thesis Supervisor: Professor M. Lei Geng

Graduate College
The University of Iowa
Iowa City, Iowa

CERTIFICATE OF APPROVAL

_____

PH.D. THESIS

_____

This is to certify that the Ph.D. thesis of

Yan Hu

has been approved by the Examining Committee for
the thesis requirement for the Doctor of Philosophy degree
in Chemistry at the May 2016 graduation.

Thesis Committee: _____
M. Lei Geng, Thesis Supervisor

_____
Gary W. Small

_____
Leonard R. MacGillivray

_____
Alexei V. Tivanski

_____
Julie L. P. Jessop

To my beloved parents Shuming Hu and Aihong Du
献给我最亲爱的父亲胡舒明和母亲杜艾虹

学而不思则罔，思而不学则殆
(He who learns but does not think is lost. He who thinks but does not learn is in danger)

《孔子·论语》
(Confucius, the Analects of Confucius)

ACKNOWLEDGEMENTS

Am I really at the end of my PhD studies? Yes, almost there! Still cannot believe I could complete this task which was considered as mission impossible when I was a teenager. It has definitely been a long and not easy journey for me to grow from a kindergarten kid with curiosity and passion on everything to a well-educated PhD student. At this moment, I am truly proud of myself for bravely conquering so many challenges and difficulties on the way to pursue this highest degree that one can ever earn. The experience of graduate school in USA is such precious treasure for me that I will cherish forever. In these years, I have learnt not just the broad knowledge of chemistry but also many other things that are so important in my future life. When I look back at the graduate school days, my heart is filled with sincere appreciations to many people who have provided me generous help, friendship and encouragement for achieving this milestone.

Firstly, I want to thank my dear parents for respecting and supporting me all the time. They taught me the first but most important lesson in my entire life, which has shaped me to be a person with a kind heart and positive attitudes in life. They are the harbor of my life that always makes me feel warm and beloved in both good and bad times. They opened my mind towards this beautiful world from all aspects in my childhood and encouraged me to fearlessly pursue all my dreams, including coming to USA which is half globe away from home for graduate studies. Hopefully this achievement of the doctoral degree will be the best gift to them for honoring their endless love.

It is now the time to express my deep gratitude to my thesis advisor, Dr. M. Lei Geng. He offered me the opportunity of doing graduate research here and earning a PhD

degree in chemistry. His intelligence in science provided me tremendous ideas and suggestions in my research works throughout these years. He has taught me not just broad knowledge of chemical science and lab skills but more importantly, he lessoned me the right way of thinking about scientific questions as well as doing research, which plays an central role on the my success in future career. I have truly experienced a wonderful PhD training under his coaching and I am certain that I will not be who I am and have what I have without his help!

I also owe big thanks to Dr. Gary Small, Dr. Leonard MacGillivray, Dr. Alexei Tivanski and Dr. Julie Jessop for serving on my academic committee. Beside the academic advisors, I also want to express my appreciation to the supervisors of internship at GlaxoSmithKline, including Dr. Yu Shi, Dr. Jacek Mozdzanowski and Lucy Xi. They acted as the bridge which linked me from the academic research to industrial pharmaceutical research and it greatly helped me to develop my future career. Also, I will never forget the great friendship with all the Geng group members, Rachel Seurer, Chengxuan Guo, Nan Jin and Yaru Hanrahan. I truly appreciate the helps from Rachel and guidance from former group members Dr. Claudiu Brumaru and Dr. Zhenming Zhong in my research projects. At the end, I would like to especially deliver my thanks and love to my boyfriend Dr. Xiang Zhou. He is always my supporter who accepts all aspects including the “crazy version” of me.

When I first time came to United States six years ago, I could never believe that I would earn a doctoral degree and create such a sparkling life for future. It is my luck to have experienced over five years of the professional PhD training from the department of chemistry of University of Iowa and met so many nice people along the way. This thesis

is written to greatly present my sincere acknowledgement to all these remarkable people in my life.

ABSTRACT

Nanoporous materials have been widely used in the fields of biological and chemical sensing, chemical separation, heterogeneous catalysis and biomedicine due to their merits of high surface area-to-volume ratio, chemical and thermal stabilities, and flexible surface modification. However, as the nature of nanoporous materials, they are inherently heterogeneous in the micro- and nanoenvironments. The environmental heterogeneity plays a decisive role in determining the performance of various applications of nanoporous materials. In order to provide an in-depth understanding of the nanoporous materials, it is of great interest to investigate the environmental heterogeneity in them. Single molecule spectroscopy, combined the quantitative confocal fluorescence imaging which possesses the capability of optical sectioning, has demonstrated to be a powerful tool to approach the environmental heterogeneity inside nanoporous materials.

Single molecule spectroscopy is an ultrasensitive technique for probing molecular transport and properties of individual molecules. This technique has been extensively used in the research of environmental heterogeneity in nanoporous materials since it removes the issues of ensemble averaging and directly approaches detailed information that is obscured in ensemble measurements. In order to proficiently interpret single molecule data, we developed a comprehensive methodology – single molecule counting – for characterizing molecular transport in nanoporous silica. With this methodology as a tool, the nanoenvironmental heterogeneity inside the nanopores of C_{18}-derivatized silica particles was explored by probing single molecular diffusion inside the pores. By employing single molecule ratiometric spectroscopy and a solvatochromic fluorophore as

reporter of local environment, the gradient in nanopolarity as well as the nanoviscosity along the C_{18} layer after the inclusion of solvent was uncovered.

The chemical properties of solute molecules at the nanopore surface are ultimately controlled by the energetics of the solute-interface interactions. The imaging of distribution of energies would be a decisive approach to assess the fundamental heterogeneity of the interface. To this end, we investigated the ΔG distribution of C_{18}-derivatized nanoporous silica particles with quantitative confocal imaging. The pixel-to-pixel and particle-to-particle analysis showed the existence of ΔG heterogeneity between particles as well as within individual particles. The heterogeneity in ΔG could be partially responsible for band broadening in chemical separations and significantly affect overall reaction yield when using nanoporous materials as solid support for heterogeneous catalysis.

PUBLIC ABSTRACT

Nanoporous material is extensively used in fields of scientific research including biological sensing, chemical separation and catalytic science. It possesses several unique properties such as large surface area, flexible surface modification and the most importantly for this thesis, the inherent heterogeneity in the microenvironments. It is of great interest to explore the environmental heterogeneity since it could significantly affect the performance of various applications of nanoporous material. Single molecule spectroscopy, combined with confocal fluorescence microscopy was demonstrated to be a powerful tool to explore the heterogeneity inside nanopores of material.

Single molecule spectroscopy is an ultrasensitive technique that allows the detection of single molecules. Unlike bulk measurement of providing an averaged single number that represents the measurement results of thousands molecules, single molecule measurement reveals a certain level of fluctuation in the measured parameter since only one molecule is measured at a time and each molecule reports unique information of its local microenvironment. Therefore, tremendous information of the heterogeneity in material that is hidden in bulk measurement can be resolved. Single molecule counting was established as a comprehensive methodology for characterizing single molecular transports. A research to apply this methodology to probe heterogeneities in nanopolarity and nanoviscosity of C_{18}-modified nanoporous silica particles was accomplished with single molecule confocal microscopy.

The ΔG heterogeneity between particles as well as within individual particles was also confirmed by quantitative confocal imaging. This heterogeneity could significantly

contribute to several issues in certain applications, for example, the band broadening in chromatographic separation.

TABLE OF CONTENTS

LIST OF TABLES

LIST OF FIGURES

CHAPTER 1

INTRODUCTION

The research presented in this thesis focuses on the methodology developments for probing the physicochemical properties of nanoporous material. Nanoporous material is a type of solid materials permeated by an interconnected network of pores. It can be made by different types of materials such as silica, alumina or sol-gels. The nanoporous materials manifest several distinct properties including high surface area-to-volume ratio, flexible surface modification and the most importantly for the research goal of this thesis, the distributions of some physicochemical properties. In other words, they are heterogeneous in nature. Nanoporous materials have been widely employed in diverse fields such as biosensing, drug delivery, heterogeneous catalysis and chemical separation. And as mentioned in many related research articles, their inherent heterogeneity plays a decisive role on determining the performance of the fundamental applications, for instance, the catalysis efficiency or overall yield when used as solid-support for catalysis and the separation efficiency when applied as the packing materials for chromatographic separation.

In this thesis, the environmental heterogeneity in nanoporous material is investigated by two major tools—single molecule spectroscopy and confocal fluorescence microscopy. Single molecule spectroscopy is demonstrated to be a powerful tool to explore the micro/nanoenvironmental heterogeneity in nanoporous material since it removes the issues of ensemble averaging and directly approaches the distribution of certain parameter without any *priori* hypothesis about the distribution. On the other hand,

quantitative confocal fluorescence imaging is employed throughout the entire research work to provide precise assessment and abundant information of the inherent heterogeneity in nanoporous material. The knowledge of these related techniques is presented in Chapter 2.

Several requirements need to be satisfied in order to perform single molecule detection. The most imperative one is to achieve an experimental system with minimal interfering fluorescent impurities since the emitted fluorescence photons are limited and thus can be easily interfered or even overwhelmed by signal from any fluorescent impurities. Chapter 3 describes the approaches to minimize the fluorescent impurities for various systems and demonstrates a suitable system that can be adopted for single molecule detection.

Tremendous information of nanoporous material is achieved by probing molecular transports at nanopore interface with confocal single molecule spectroscopy. Chapter 4 introduces the single molecule counting as a comprehensive method for characterizing molecular transport in nanoporous silica. Single molecule counting provides the most sensitive measurement of molecular concentration and the variance in measurement is determined by fundamental shot noise. Moreover, the time, height, width and shape of bursts of single molecules carry significant information on molecular distribution, diffusion and adsorption in the network of nanopores and enables the assessment of micro/nanoenvironmental heterogeneity in the nanoporous silica. The information uncovered by single molecule counting is essential in understanding the nature of nanostructures.

After establishing the single molecule counting as a method to characterize molecular transport, Chapter 5 explores the environmental heterogeneity inside the nanopores of C_{18}-modified silica particles by probing individual molecule's transport. Single molecule ratiometric spectroscopy and fluorescence correlation spectroscopy are used to reveal the gradient in nanopolarity and nanoviscosity along the C_{18} layer after the inclusion of solvent molecules. This single molecule approach determines the architectural and solvation heterogeneities without *priori* hypothesis about the distribution which is required in conventional bulk measurement.

Chapter 6 investigates on the ΔG distribution of nanoporous C_{18}-derivatized silica particles by using quantitative confocal imaging. Considering the accuracy and precision of quantitative analysis, the imaging system is thoroughly calibrated and validated upon measurements. The results confirm the existence of ΔG heterogeneity between particles as well as within individual particles. The distribution of ΔG could significantly affect the bandwidth of chromatographic separation and overall reaction yield of heterogeneous catalysis.

A preliminary study of the nanoporous C_{18}-derivatized silica particles as the vehicles of drug delivery was conducted and presented in Chapter 7. As a big breakthrough from previous related research in the group, the bile salt-assisted solubilization of these hydrophobic particles in bio-compatible aqueous environment was investigated. The resulted data demonstrates the capability of bile salt molecules to solubilize these hydrophobic particles in aqueous phase and supports the particles to be promising candidates of drug delivery vehicles. Some potential studies and directions of

future research based on the works presented in this thesis is proposed and briefly presented in Chapter 8.

CHAPTER 2

BACKGROUND

2.1. Introduction to Confocal Microscopy

For decades, confocal microscopy has been intensively employed as a research tool in biological and biomedical imaging as well as in the investigation of nanostructures and nanomaterials [1-8]. Confocal microscopy garnered its popularity in various fields of scientific research because it possesses the capability of acquiring images at high resolution and contrast. With the tremendous merits in optical sectioning, this technique enables three-dimensional imaging deep inside thick biological specimens in *vivo* [4, 5, 9-11]. Among various modes of confocal imaging, confocal microscopy operated in epi-fluorescence mode is the most commonly used due to the high sensitivity of fluorescence detection. The fluorescence confocal microscopy is thus the technique extensively utilized in our research and its principles and advantages are described in the following sections.

2.1.1. Principles of confocal imaging

Generally, to image a thick biological specimen with traditional widefield microscopy, the specimen is placed on the sample stage of the microscope and the excitation light beam is focused into a wide cone which illuminates the specimen over a large region simultaneously, including both in-focus and out-of-focus regions, as shown in Figure 2.1A. The produced image is then a combination of the well-resolved image collected from the focal plane and the "blurred" images collected out of the focal plane, in the out-of-focus region. This leads to a compromise in the image quality, for limited contrast and resolution. This issue can be easily overcome by introducing the confocal

geometry to the imaging system. On one hand, as illustrated in Figure 2.1B, the objective lens of confocal microscope focuses the laser beam into a point-like light source, a diffraction limited volume with lateral diameter about 0.25 to 0.8 μm and axial diameter about 0.5 to 1.5 μm at the focal plane. The exact dimensions of this probe volume are determined by the optical configuration of each component of the microscope system. Compared to the conventional widefield microscopy which provides a large probe volume under illumination, only a small point-like region in the specimen is illuminated at a time in confocal microscopy imaging. Therefore, in order to build a two-dimensional image in confocal microscopy, the focused point-like probe volume needs to scan across the specimen of interest pixel-by-pixel and then line-by-line in a laser beam scanning mode or sample stage scanning mode [12]. Moreover, because of the limited observation volume, the interference from scattering is also minimized.

On the other hand, as an important feature of confocal imaging, by adopting a confocal aperture such as an optical pinhole into the emission light path of the microscopy system, the autofluorescence signal originated from the out-of-focus region can be rejected, and only the fluorescence from the focal plane of the specimen can pass through the aperture and reach the detector. These are the two main reasons that account for the improvements in image resolution and contrast for confocal imaging.

Figure 2.2, presenting the general schematic diagram of light path in confocal microscopy, is introduced to demonstrate the principles of confocal imaging. First of all, the excitation laser beam (shown in green solid lines) is reflected by a dichroic mirror and focused by the objective lens of microscope into a diffraction limited probe volume. The probe volume is located at the focal plane inside the specimen. The emitted fluorescence

is then focused by the lens and transmitted through the dichroic mirror. To effectively reject the autofluorescence generated from the out-of-focus plane and the scattering signal, an optical pinhole is placed in front of the detector. As illustrated in Figure 2.2, only the emitted fluorescence from the focal plane (shown in red solid lines) can successfully pass through the pinhole and reach the detector, while the fluorescence from the out-of-focus regions plane (shown in red dash lines) is excluded from image formation. The constructed image from the confocal microscopy system only contains the information of the focal plane and as a result, the image resolution as well as contrast are significantly improved.

2.1.2. Resolution and contrast of confocal imaging

2.1.2.1. Resolution

In confocal imaging, both the illumination and detection are limited to a point. However, in reality, the image from a point light source is not exactly a single point. Instead, it is a small diffraction pattern which possesses a well-defined bright “disk” at the central region and progressively fainter concentric rings at the peripheral, known as Airy diffraction patterns. The bright (shown in red) and dark rings (shown in white) alternatively appear in the Airy patterns, as illustrated in Figure 2.3A. The function that quantitatively describes this diffraction pattern is known as the point spread function (PSF). This function defines the intensity distribution in the image of a point source in three-dimension (Figure 2.3B). According to the distribution of 3D-PSF, about 84% of total energy is condensed within the region enclosed by the first dark ring (minimum) of the diffraction pattern. And this region is known as the Airy disk. A clear illustration of the two-dimensional projections of a computed ideal 3D-PSF at in the XY and XZ planes

are presented in Figure 2.4. And the Airy disk—the central maximum with the greatest diameter in lateral direction is also indicated in Figure 2.4B. The diameter of the Airy disk is known as the Airy unit (*AU*) and is defined as:

$$d_{Airy} = 1\ AU = \frac{1.22 \times \lambda_{ex}}{NA} \quad [2.1]$$

where λ_{ex} represents the excitation wavelength and *NA* is the numerical aperture of the objective lens. The Airy unit (*AU*) is typically used in the pinhole size normalization and the resolution – the discrimination between two point objects is determined by the Rayleigh criterion.

When imaging a single point object, the confocal microscopy system generates two images of this point. One is due to the projection of the point-like illumination source into the object space and the second is by projecting the emitted fluorescence from the point object into the image space. As a whole, the final resulted point spread function (PSF_{total}) from the confocal microscopy system is thus a convolution of the two PSFs and is denoted as:

$$PSF_{total}(x, y, z) = PSF_{ill}(x, y, z) \otimes PSF_{det}(x, y, z) \quad [2.2]$$

where PSF_{ill} represents the intensity distribution of the point-like excitation laser spot whose size is determined by the wavelength of the excitation laser and the numerical aperture of objective lens, as described by Equation [2.1]. The PSF_{det} corresponds to the intensity distribution of emitted fluorescence collected behind the pinhole. PSF_{det} is a function of the laser probe volume as well as the size of the confocal pinhole placed in front of the detector.

The diameter of pinhole is a decisive parameter in determining the resolution and the thickness of the optical slice (also called depth discrimination) of the point-like fluorescence image of each single point object. This principle is illustrated in Figure 2.5.

In the case when the pinhole diameter is large - greater than 1 *AU*, the image resolution and optical thickness is essentially dominated by the law of geometric-optical confocality. As illustrated in Figure 2.5A and B, as the pinhole diameter decreases, the magnitude of PSF_{det} approaches to that of PSF_{ill}. In other words, when pinhole diameter is greater than 1 *AU*, the resolution is completely determined by PSF_{ill}. The lateral and axial optical resolutions are then defined as:

$$FWHM_{ill,lateral} = \frac{0.51\times\lambda_{ex}}{NA} \quad [2.3]$$

and

$$FWHM_{ill,axial} = \frac{0.88\times\lambda_{ex}}{(n-\sqrt{n^2-NA^2})} \quad [2.4]$$

where $FWHM_{ill,\ lateral}$ and $FWHM_{ill,\ axial}$ represent the full width at half maximum of intensity distribution of PSF_{ill} in the lateral and the axial dimension, respectively. λex is the wavelength of the excitation laser and *n* is the refractive index of the immersion oil. *NA* corresponds to the numerical aperture of the objective. These two equations demonstrate the improvements in spatial resolution in confocal imaging technique since the optical resolution is a function of the excitation wavelength, the refractive index of the immersion oil and the numerical aperture of the objective lens but independent of the emission wavelength like the traditional widefield microscopy. Therefore, depending on the Stoke-shift between the excitation and the emission, the resolution of confocal imaging is improved by a factor of $\lambda_{em}/\lambda_{ex}$ [13]. Thickness of the optical slice, or depth

discrimination, is determined by the intensity distribution of PSF_{det} in the axial dimension which is defined as:

$$FWHM_{det,axial} = \sqrt{\left[\frac{0.88\times\lambda_{em}}{(n-\sqrt{n^2-NA^2})}\right]^2 + \left(\frac{\sqrt{2}\times n\times PH}{NA}\right)^2} \quad [2.5]$$

where PH is the pinhole diameter and λ_{em} represents the emission wavelength. The equation predicts that as the emission wavelength or the pinhole size increases, the optical slice thickness increases as well.

When the pinhole diameter is smaller than 1 AU, in a more extreme case of a diameter of 0.25 AU (Figure 2.5C), the sizes of PSF_{ill} and PSF_{det} are approximately equal and the resolution is now governed by the wave-optical law. Basically, the interaction between PSF_{ill} and PSF_{det} plays an important role in determining resolution. Under this condition, the resolution in the axial dimension and the optical slice thickness are approximately the same and defined as the $FWHM$ of the intensity distribution of PSF_{total} :

$$FWHM_{total,axial} = \frac{F_{axial}\times\bar{\lambda}}{(n-\sqrt{n^2-NA^2})} \quad [2.6]$$

where F_{axial} is the scaling factor of resolution in axial dimension corresponding to a certain pinhole size. $\bar{\lambda}$ represents the averaged wavelength of excitation and emission, defined as:

$$\bar{\lambda} = \sqrt{2}\frac{\lambda_{ex}\times\lambda_{em}}{\sqrt{\lambda_{ex}^2+\lambda_{em}^2}} \quad [2.7].$$

And the resolution in the lateral dimension is calculated as:

$$FWHM_{total,lateral} = \frac{F_{lateral} \times \bar{\lambda}}{NA} \quad [2.8]$$

where $F_{lateral}$ corresponds to the scaling factor of resolution in the lateral dimension. Figure 2.6 illustrates the correlation between the value of applicable scaling factor and the pinhole diameter (between 0 to 1 *AU*), in both the lateral and the axial dimensions.

When imaging two or more point objects, the point-to-point resolution is concerned. In this case, Rayleigh criterion needs to be introduced. In order to differentiate between two point sources, the distance between these two points needs to be greater than the radius of the Airy disk. In other words, according to the definition that describes the Rayleigh criterion:

$$\theta_{min} = sin^{-1} \frac{1.22 \times \lambda}{D} \cong \frac{1.22 \times \lambda}{D} \quad [2.9]$$

where λ is the wavelength of the point light source and D is the diameter of confocal aperture, the two points can only be resolved when their angular separation is greater than the limiting value θ_{min}. A schematic diagram illustrating the Rayleigh criterion is presented in Figure 2.7.

2.1.2.2. Contrast

Beside the optical resolution, contrast is the other component that determines the image quality. As described above, resolution is a "pure" concept that can be directly characterized and measured by the rules from the system's geometry. While contrast usually refers to practical measurements of resolution and in this situation, noise as well as the brightness of adjacent point objects plays a decisive role in determining the image quality.

Contrast indicates the difference in the maximum intensity of two adjacent point objects and the minimum intensity between these two illuminous points. It is described as:

$$C = \frac{n_b - n_d}{n_b + n_d} \quad [2.10]$$

where n_b represents the intensity of the brightest spot (the "peak" of the intensity distribution of *PSF* of a single point object) and n_d corresponds to the intensity of the dim spot (the "dip" between the intensity distributions of *PSF*s of two adjacent point objects) [14, 15]. Since the maximum intensity of PSF is normalized to 1and the minimum intensity can go down to 0, the contrast ranges from 0 up to 1. The concept of image contrast is illustrated in Figure 2.8A.

In the case of two adjacent illuminous point sources with equal intensity, the Rayleigh criterion is translated into a contrast criterion and that states if the contrast *C* is equal to or greater than 26.4%, these two point sources with equal intensity can be resolved in the image.

However, in most imaging experiments, noise is inevitable in the emitted fluorescence signal and the resulted image intensity exhibits a certain level of "noisy" fluctuation, as illustrated in Figure 2.8B. Compared to the signal without noise (Figure 2.8A), visually, the significant fluctuation of signal may affect the differentiation between these two point sources. In other words, the "dip" between the two *PSF*s may not be clearly resolved. The figure demonstrates that in practical imaging where noise is inevitably involved, the distinction between two adjacent illuminous point sources in the image does impair, even though the Rayleigh criterion still holds.

In conclusion, the resolving power of confocal imaging is not solely determined by the optical resolution but also related to the noise level of the practical imaging experiments as well as the brightness of each spot on image.

2.2. Quantitative Confocal Imaging

Confocal Fluorescence microscopy has been employed to image biological structures for years. With the development of novel approaches such as fluorescence resonance energy transfer (FRET) and fluorescence recovery after photobleaching (FRAP) as well as the advances in instrument performance, confocal microscopy nowadays has been extensively used in quantitative investigations of the spatial and temporal information of the fluorophores in specimens [16-23]. For instance, it is widely used to probe time-resolved processes in biological structures. The intracellular binding-diffusion kinetics, a very common interaction occurring in cells, can be approached by quantifying the diffusion coefficients and the binding constants (k_{on} and k_{off}) with confocal FRAP [24].

Even though quantitative confocal imaging provides outstanding merits of in-depth investigations on biological processes and structures of specimen, a thorough understanding of related fundamental parameters that affect the quantitative results as well as some practical limitations to confocal microscopy system is still needed in order to achieve accurate and reliable quantitative information of specimen. Here the main aspects and practical considerations that relate to the quantitative confocal imaging technique are discussed in detail.

2.2.1. Accuracy and precision in quantitative confocal measurement

When discussing the accuracy and precision in quantitative confocal measurement, the first thing of interest is how the quantitative information is presented in the generated digital image. As known, the most commonly used detectors in confocal imaging are charge-coupled devices (CCD), avalanche photodiodes (APD) and photomultiplier tubes (PMT) [25-27]. Even with different mechanisms of transduction, the goal for all detectors is to convert the detected photons into an electrical signal whose intensity is correlated to the photon counts during the image acquisition process. The constructed image is composed of a two-dimensional matrix of pixels with equal size. Each pixel represents a well-defined point like area of the entire image, with intensity destribution governed by the *PSF*. The coordinates of each pixel corresponds to a specific area of the specimen. The detected fluorescence signal at each pixel is thus a function of concentration of fluorophores at the corresponding area of the specimen. Additionally, by continuously collecting images on the 2-D imaging plane overtime, a series of images containing time-dependent information of fluorescent intensity can be approached. Therefore, the quantitative information related to specimen is presented as (1) the spatial information which can be used to quantify or assess the spatial distribution of some properties of the specimen and (2) the temporal information which can reveal time-dependent dynamic processes occurring in the specimen and (3) the intensity of each pixel which can be used to directly quantify the concentration of fluorescent molecules present at each spot of the specimen. By constructing the relationship between spatial, temporal and intensity information, the overall quantitative analysis of the confocal image can be achieved.

Generally, from analytical measurement point of view, the accuracy and precision need to be thoroughly considered for any quantitative analysis in order to draw a reliable conclusion since error inevitably exists in any measurement. The accuracy, indicating the closeness to the true value and the precision, representing the reproducibility of repeated image measurements, are the direct presentations of errors in quantitative measurements.

Accuracy in confocal imaging plays a key role in achieving the correct quantitative information from the original digital images. In the calibration study—an inescapable and primary step for quantitative measurement, for instance, a series of "standard" confocal images need to be collected to build up the calibration curve. If significant level of error is included in the image collecting process, the measured intensity will substantially deviate from the "true" intensity that corresponds to the amount of fluorophores actually in presence. The resulted detection limit and dynamic range of this quantitative methodology will thus be inaccurate and fail to accurately correlate the measured signal intensity with the "true" concentration of fluorophores in the specimen, eventually leading to unreliable conclusions. Precision, on the other hand, is also crucial in quantitative confocal imaging, especially when performing one time-point imaging or tracking time-dependent processes (such as time-lapse imaging in live cells). In these situations, every single image contains different but time-dependent information of the specimen. Image reproducibility becomes decisive in correctly quantifying the temporal information of interest.

Therefore it is imperative to understand the sources that contribute to the inaccuracy and imprecision of quantitative confocal imaging and how they can be avoided or reduced in order to accurately quantify the spatial and temporal information

from the original images. Practically, in quantitative confocal imaging, there are a number of sources that could introduce errors into the measurements, such as the optical geometry of the microscope, variations associated with the measurements as well as the specimen itself. Some of them can be reduced or corrected to improve the precision and accuracy, while some are simply intrinsical to the system and cannot be avoided. The main sources that are closely related to the accuracy and precision of quantitative confocal imaging technique are detailed below.

2.2.2. Signal and noise

In quantitative confocal imaging, the fluorescence emitted from the target fluorophores is of interest. However, the signal level is low compared to conventional widefield fluorescence microscopy. There are three main reasons that contribute to this fact. (1) Because of the limited size of the detection volume, usually at the magnitude of femtoliters, only a small number of fluorescent molecules are present in the detection volume and thus result in low intensity of emitted fluorescence. (2) Image is acquired through pixel-by-pixel scanning across the specimen with the laser probe volume. The time required to collect the entire image is the sum of the time spent on each pixel (the integration time). Therefore the integration time is usually short in order to complete image collection in a reasonable amount of time. This short integration time leads to limited number of photons emitted/detected from fluorophores. (3) When a small size pinhole is used to improve the resolution, the detected fluorescence signal drastically decreases. As illustrated in Figure 2.9, when the pinhole diameter is reduced from 2 *AU* to 0.05 *AU*, the resolution (indicated as *FWHM*) and the contrast are significantly improved (Figure 2.9A), while at the same time, the fluorescence signal is drastically

decreased by ~70% (Figure 2.9B). Some experimental tips have been suggested in order to maximize the signal and optimize image quality for quantitation such as choosing fluorophores with high photo-stability and quantum yield and using objective lens with highnumerical apertures.

However, merely maximizing the fluorescence signal does not necessarily significantly improve the accuracy and precision in quantitative confocal imaging since the acquired image contains not only fluorescence signal of interest but also noise from various sources [28, 29].

Noise exists in many components in confocal microscopy imaging, from the light source—laser beam to the detector. Generally, there are three main sources of noise involved in confocal imaging: the laser noise, the shot noise (also known as the Poisson noise) and the dark noise.

Shot noise or Poisson noise, is attributed to the stochastic quantum nature of light. Photon-counting, as a random event, fundamentally follows Poisson statistics [30, 31]. In other words, when repetitively counting the number of photons in a certain specimen, the number of photons counted each time should result in a Poisson distribution. Hence, the uncertainty or standard deviation in photon counting referred to as the shot noise, is calculated as:

$$\Delta N_{Poisson} = \sqrt{N} \qquad [2.11]$$

where N represents the number of photons detected in on unit of integration time per pixel [32]. The value of N can be estimated by the equation [33]:

$$N = \left(\frac{f}{i_{max}-o}\right) \times (i - o) \quad [2.12]$$

where *f*, i_{max} and *o* correspond to full well capacity of detector, maximum intensity that can be produced by detector and off-set of detector, respectively and all these values can be approached from specifications of the detector in use. *i* is the intensity that has been converted to photons. Additionally, the signal-to-noise ratio (*SNR*) associated with shot noise is defined as:

$$SNR_{Poisson} = \frac{N}{\sqrt{N}} \quad [2.13].$$

Different from other types of noise which can be reduced, shot noise can never be reduced or removed. Therefore, the imprecision and inaccuracy associated with the shot noise cannot be avoided and are always present in quantitative analysis. However, according to the definition of *SNR* (Equation [2.13]), as the number of detected photons *N* increases, *SNR* increases and in other words, the percentage shot noise, known as $\frac{\sqrt{N}}{N} \times 100\%$ decreases. Optimizing the photon collection efficiency is thus a key approach to minimizing the contribution from the shot noise and improving the precision of quantitative confocal measurements.

It is noted that Equation [2.12] describes the digitization of an intrinsic analog signal from the detector into a digital signal. The integrated electrical signal from the transducer, for example, the charges accumulated in a well of the CCD chip or the anodic current of a PMT, is proportional to the input photon counts, and is digitized in image output. For high-precision quantitative imaging, it is imperative to use the highest-resolution digitizers to collect the images. In commercial confocal microscopes, typically 16-bit digitization represents the best resolution and provides 65,536 levels of intensities.

The commonly used 8-bit digitization, corresponding to 256 intensity levels, is rarely sufficient for true quantitative image analysis.

In our home-built confocal fluorescence imaging system, the APD detectors are operated at true photon-counting mode. Each detected photon generates a digital TTL pulse that is directly counted. The fluctuation in the electron pulse heights thus does not influence the photon counts. This detection represents the highest level of precision in light detection.

Dark noise is thermal noise from the detector. The level of dark noise is determined by the thermal electrons generated by the detector. Dark noise can be significantly reduced by coupling the detector with a cooling system. Beside the dark noise, there are other noise sources associated with the electronics in the detector module such as the amplifier noise and the readout noise [25, 30, 34]. When utilizing PMT as the detector, specifically, the multiplicative or secondary emission noise which is generated at the dynodes of PMT during photoelectron multiplying process, which leads to fluctuations in the electron pulse heights at the anode, needs to be considered [35]. The multiplicative noise can be reduced by applying higher voltage on the dynodes since the photon collection efficiency can be improved at high voltage, or by using dynode geometries that focus the electron trajectories, and this leads to an increase in *SNR*.

Overall, considering all main noise sources, the total noise can be expressed as:

$$\Delta N_{total} = \sqrt{\Delta N_{laser}^2 + \Delta N_{shot}^2 + \Delta N_{detector}^2 + \Delta N_{electronics}^2 \cdots} \qquad [2.14].$$

When using PMT as detector, the total SNR is defined as:

$$SNR = \sqrt{\frac{N^2}{se^2 \times (N + N_d) \times (1 + q^2)}} \quad [2.15]$$

where N is the number of photoelectrons per integrated time, se is a noise factor of secondary emission, q represents peak-to-peak noise factor of the laser and N_d corresponds to the number of thermal electrons generated at detector per integrated time.

As described above, the noise exhibited in the quantitative confocal measurements is an overall noise generated by different components of the microscopy system. Some types of noise can be reduced but some cannot be. Moreover, noise is not a constant and therefore cannot be directly subtracted from the original image. In other words, noise is inevitably included in the quantitative analysis of confocal imaging. Therefore, in order to minimize the interference from noise which leads to the decrease in accuracy and precision, the priority consideration in quantitative confocal imaging is to improve the photon collection efficiency and at the same time, reduce the noise level during image acquisition as much as possible.

2.2.3. Other practical considerations in quantitative confocal imaging

2.2.3.1. Ground-state depletion of the fluorophore

In quantitative confocal measurements, in order to understand the performance of the the microscopy system, the first task of interest is to establish the correlation between the excitation laser power and the emitted fluorescence intensity. The fluorescence intensities at a series of excitation laser power thus need to be measured. However, careful consideration needs to be taken in determining the range of laser power applied for this calibrating study. The laser power ought to be low enough to avoid the occurrence of ground-state depletion of fluorophores, especially for those at the focal

plane where they experience the highest photon flux or power density of excitation light. The ground-state depletion leads to a deviation of the actual calibration curve from its ideal linear relationship which is obtained at low laser powers, as illustrated in Figure 2.10. If this situation occurs, the emitted fluorescence from the fluorophores at the focal plane is less than that expected and as a result, the quantitative relationship between the emitted fluorescence intensity and the amount of fluorophores present at specific spot of the specimen is destroyed. It eventually leads to a certain level of inaccuracy of the quantitative confocal measurements. The depletion threshold is determined by the absorption cross section and the excited state lifetimes of the fluorophores and the photon flux. The photon flux needs to be low enough so it does not exceed the level when a large number of molecules are going through the excitation-emission cycles at the maximum rate.

2.2.3.2. Non-uniformity in confocal imaging

In the ideal situation of quantitative confocal imaging, the emitted fluorescence intensity is proportional to the concentration of fluorophores. However, in practice, there are some slight variations involved due to the non-uniformity in both the detectors and the illumination field. These non-uniformities in illumination field and detection system are detrimental to quantitative confocal imaging since the measured fluorescence intensity may not be equal to the "true" intensity and thus fail to indicate the actual concentration of fluorophores present in a certain area of the specimen.

One source of the non-uniformity in confocal imaging is associated with the performance of the detector used. When applying a PMT or an APD as the detector, the non-uniformity on the "detection plane" is caused by the stochastic noise of the thermal

electrons generated within the detector. This generates random fluctuations on the "detection plane", as demonstrated in the "dark" image in Figure 2.11A. When using a CCD as the detector, on the other hand, the non-uniformity is attributed to the unevenly distributed dark current across the entire "detection plane". As illustrated in Figure2.11B, there is a particular fluctuation pattern in the "dark" image. The non-uniformity associated with the CCD detector can be eliminated by directly subtracting the "dark" image from the original image of the specimen since it shows a certain pattern and is a systematic error. By contrast, the non-uniformity associated with a PMT or APD detector cannot be avoided since it is generated by the noise of thermal electrons and the pattern is constantly changing with every single slice of the image, a signature of this random noise By good fortune, compared to the contributions from other sources of noise, the non-uniformity associated with the dark noise is unlikely to significantly interfere with the quantitative confocal measurements [36].

In fact, the major non-uniformity that essentially impairs the accuracy and precision in quantitative confocal measurements is attributed to the optical geometry of the confocal microscopy system. Some intrinsic "defects" in optical configurations generate a certain level of intensity non-uniformity or shift on the illumination field. The fluorophores in different areas of specimen, even at identical concentration, will emit different amount of fluorescence because of the unevenly distributed intensity of excitation light on the illumination field. As a result, the obtained confocal image fails to reflect the "true" distribution of fluorophores in the specimen and the correct quantitative information of specimen cannot be achieved.

Some non-uniformity on illumination field of confocal microscopy system can be corrected in multiple ways [37, 38], however, it is impossible to eliminate all non-uniformity in the system and achieve an evenly distributed illumination since the patterns of some non-uniformity vary day-by-day and slice-by-slice. Therefore in practical confocal imaging, in order to produce reliable quantitative information of the specimen, the level of the overall non-uniformity and its contribution to the results need to be cautiously and specifically evaluated for each image slice.

2.2.3.3. Other considerations

Beside the two major factors that could deteriorate the accuracy and precision in quantitative confocal imaging, there are other factors that need to be taken into consideration in order to approach a trustworthy quantitation of the specimen. For example, (1) the saturation point of the detector. For most detectors, the detected/output photon count decreases at higher incoming signal level and the count at which the output rate starts to decrease is known as saturation point. If measurements are performed beyond the detector saturation point, the microscopy system fails to accurately report the actual number of photons arrived at the detector. Even worse, exposure to intense light source could damage the detector; and (2) photobleaching of fluorophores. During image acquisition, the fluorophores in specimen experience photobleaching because of the exposure to the illumination light source. The rate of photobleaching and its effect on the measurements is dependent on both the intensity of excitation light and the local environment of the fluorophores. In some cases, photobleaching may introduce a significant level of error into the quantitative confocal measurements but it can always be corrected [37, 39, 40]; and (3) autofluorescence in specimen and cross-talk between different

fluorophores. In the application of imaging of biological structures, some naturally fluorescent species contained in the specimen may emit fluorescence signal with the similar wavelength range to the fluorophores used for labeling. On the other hand, in multicolor confocal imaging experiment, more than one type of fluorophores is applied to achieve localization of different components in the specimen. When multiple probe molecules are used, cross-talk is likely to occur, especially emission cross-talk [16] . The cross-talk and autofluorescence are always eliminated or at least reduced by good selection of the filter sets and judicial choices of the fluorophores in quantitative confocal imaging.

2.3. Single Molecule Spectroscopy

Single molecule spectroscopy allows the direct observation of "exactly one" molecule within the sample matrix by applying light radiation. In other words, single molecule spectroscopy represents an ultra-sensitive tool to probe the molecule of interest at the level of ~1.66×10^{-24} moles. However, observing one molecule in reality is not a simple task like drawing a single molecule in elementary chemistry textbook. The challenges of achieving optical probing of single molecule are mainly from two aspects: (1) The limited signal generated by one molecule and the significant interfering background signal make it difficult to observe the single molecule and (2) the optical diffraction limit, which is far beyond the size of most molecules, also hinders the direct resolving of single molecules.

Single molecule has been approached by using several indirect methods in very early times [41, 42]. The first study that demonstrated the direct observation of single molecules was reported by Moerner in 1989 [43, 44]. Moerner and coworkers obtained the

optical-absorption spectra of single molecules of pentacene which was placed in a terphenyl host crystal. The interfering background signal was removed by combing frequent modulation and ultrasonic modulation spectroscopy. The entire measurement was conducted at liquid He temperature. Considering the fact that the capability of fluorophore to absorb photons is decreased because of the drastically reducing absorption cross section [45] as well as the increasing photobleaching of fluorophore at higher temperature, single molecule detection at early stage was usually performed at cryogenic temperature. In 1990, Soper and coworkers demonstrated the first efficient detection of single fluorophore in solution at room temperature by applying repetitively pulsed laser and the time-gating to discriminate between emitted photons [46, 47]. This was the breakthrough in the field of single molecule spectroscopy since it opened the door to approach transport of individual molecule as well as nanoenvironmental heterogeneities in biological samples under physiological condition where the related information is more enriched.

As described above, a number of challenges have been effectively conquered over the years to achieve optical probing of single molecules. Today, single molecule measurements are still a powerful tool for probing molecular systems in bioscience and material sciences. What information does single molecule spectroscopy offer? Under what circumstances does single molecule spectroscopy provide unique information? To answer these questions, several distinctive advantages of single molecule measurements have been addressed in several review articles in the area [48-51].

In short, single molecule measurements provide information on structural and dynamic heterogeneity in the molecular system, and can extract rare molecular events

that typically are buried in the ensemble average in bulk measurements. In conventional bulk measurement, the result is the statistical average value of the parameter being measured since a large number of molecules are interrogated at a time and therefore the experiment yields an ensemble averaging all molecules. In contrast, single molecule spectroscopy samples each individual point of the ensemble and enables the construction of frequency histograms of the heterogeneous distribution of molecular parameters. In systems where each molecule displays different structure and dynamics, single molecule spectroscopy supplies detailed distributional information that is not accessible through any other measurements. The shape and number of peaks in the distribution, for instance, essentially imply heterogeneity of the system [52-56]. Another merit of single molecule spectroscopy is its ability to measure time-dependent processes. Ensemble measurements of time-dependent parameters such as diffusion coefficients and kinetic rates require the synchronization of large number of molecules being measured so they can start at exactly the same state. In single molecule measurements, the synchronization of the "population" of molecules is not necessary as the time trace of the molecular events is monitored one molecule each time. Single molecule methods, with the ability of optical sensing, can directly approach many fast processes such as kinetic pathways of enzymatic reactions [57-61] and the folding-unfolding processes of protein molecules [62-64]. A final advantage for performing optical detection of single molecules is to reveal rare events associated with the molecular system, which is also known as single-molecule nanophotonics or single quantum system since only one molecule gets excited at a time and provides information about itself and its local environment [65]. A surprising fact is that almost all single quantum systems exhibit some form of fluctuating [66-69], blinking [70] and quantum jumps

[71]. These events, although rarely happen, provide diagnostic information and unprecedented insights into the single-molecule system, which are typically obscured in conventional ensemble measurements.

Most optical studies of single molecules are conducted by coupling microscopy with fluorescence spectroscopy because of its outstanding sensitivity. The principles introduced in the next section will be focused on single molecule fluorescence spectroscopy.

2.3.1. Principles of single molecule fluorescence spectroscopy

To detect a single molecule, two experimental requirements need to be satisfied. One is to ensure the observation of only one fluorophore of interest at a time in the laser probe volume; the other is to achieve a reasonable level of signal-to-noise ratio (SNR).

Guaranteeing one molecule in the detection volume is typically achieved by studying samples at very low concentrations, coupled with small probe volume. According to Poisson distribution, for an analyte concentration of 50 *pM* (5×10^{-14} *moles/liter*) and a probe volume of 0.33 *fL* (3.3×10^{-16} *L*), the probability of finding one molecule in the probe volume is 0.99% while the probability of observing two molecules simultaneously in the probe volume is only ~0.005%. The calculation indicates that the chances of multiple molecules to simultaneously reside in the laser focal volume are negligible. Fluorescence signals observed under these conditions are emanated from individual molecules.

A good SNR is crucial in single molecule spectroscopy. The emitted fluorescence from one molecule cannot be distinguished from the background unless a high enough

SNR is achieved. This is accomplished by maximizing the emitted fluorescence signal from the molecule and minimizing the interfering background noise at the same time. Among various detection methods, fluorescence spectroscopy demonstrates its unique advantage in providing an excellent SNR, which can be explained by the fundamental processes in fluorescence emission presented in the Jablonski diagram in Figure 2.12. At the room temperature, vast majority of the molecules are populated in the lowest vibrational state of the electronic ground state (S_0). By absorbing a photon from the excitation light (~ fs process), a molecule is promoted to an excited electronic state (the first excited singlet state S_1 in the diagram). The molecules in the excited vibrational levels of S_1 quickly (~ ps process) relax to the lowest vibrational state through vibrational relaxation. The molecules then return to the electronic ground state at a rate (~ ns process) that is determined by the fluorescence lifetime, followed by vibrational relaxation back to the lowest energy state. The molecule is now ready to be excited again. In single molecule spectroscopy, the molecule is cycled between the ground and the excited states for many times when it traverses the probe volume, emitting a burst of photons that carries information on its diffusion. The maximum number of photons that the molecule can emit per second is governed by its fluorescence lifetime, or how fast it can be cycled. Once in a while, the molecule crosses from S_1 to the excited triplet state T_1 through intersystem crossing, where it becomes fluorescently silent for a relatively long period of time as the transition back to the S_0 state is forbidden and slow (~ μs to ms). The reorientation of the solvent molecules around the excited state dipole lowers the energy of S_1 and in turn raises the energy of S_0, resulting in a smaller energy gap in the fluorescence emission compared to the excitation. This energy loss during the transition

cycle leads to a redshift between the absorption and emission spectra, which is known as the Stokes shift in fluorescence. The Stokes shift leads to a good separation of fluorescence emission from the excitation, and therefore, compared to other spectroscopy methods, a higher SNR is achieved in fluorescence spectroscopy. To maximize the SNR in single molecule fluorescence detection, several experimental factors are considered to maximize the fluorescence signal and minimize the background noise.

In order to maximize the fluorescence signal, two aspects of the fluorescence measurements are optimized. One is to improve the signal collection and detection efficiency, and the other is about the appropriate selection of fluorophores.

Generally, to improve the photon collection efficiency, the first thing to do is to select microscope objectives with high numerical apertures (N.A.). In microscopy, numerical aperture is used to indicate light collection capability. The greater the N.A., the larger the solid angle of collection and thus a higher fraction of emission light can be collected. For example, an objective lens with N.A. of 0.44, 0.80 and 1.45 can collect 5%, 20% and 40% of light, respectively, from a point source radiating in all directions.

The second thing to think about is the choice of fluorophores. Selecting an appropriate dye molecule is a critical step in single molecule measurements since the nature of the molecule determines its photochemical and photophysical properties such as the quantum yield, the absorption cross section and photostability. The quantum yield indicates the photon emission capability of the fluorophore, defined as the number of photons emitted for each absorption event. The absorption cross section can be understood as the effective area of molecule that photon needs to traverse in order to be

absorbed and it implies the probability for fluorophore to be photo-excited. The photostability refers to the fluorophore's level of resistance to photochemical degradation under radiation energy. Generally, in order to maximize the fluorescence emission signal, fluorophores with high quantum yield, absorption cross section and photostability are desirable.

The last thing to do to maximize signal collection efficiency is to select an appropriate detector that adapts to the measurement. In the application of single molecule fluorescence spectroscopy, two categories of detectors are in use—single-channel detectors and two-dimensional array detectors CCD cameras have emerged to be a widely used array detector over years in single molecule fluorescence detection [50, 72], especially in combination with wide-field epi-illumination or total internal reflection (TIR) excitation [50, 73]. Back-illuminated silicon CCD array detectors with liquid-N_2 cooling system are one example of modern CCD detectors used in spectroscopy that boast high photon detection sensitivity [49, 74]. This type of CCD array detectors can achieve a quantum efficiency of ~70% - 80%. The dark counts are drastically reduced to about 1 *electron/pixel/hour* because of the low operation temperature (~ -120 ^{o}C) provided by the cooling system. Major drawbacks of CCD array detectors include (1) fairly high level of readout noise and (2) the speed at which signal can be read out is slow because of the low temperature and this has drastically limited the time resolution (*ms*) of the detector [50]. Thus, CCD array detectors are more commonly used in long-time averaging experiments of single molecules that do not demand fast time resolution. In the applications of probing mobile molecules, single-element detectors are employed. Two types of single-element detectors used in UV and NIR regions are microchannel PMTs, which were

applied in early experiments in the SMD field [75], and avalanche photodiodes (APD) [76]. Compared to CCD array detectors, PMTs provide higher time resolution that is adequate for the observation of molecules diffusing across the laser probe volume. While providing suitable temporal response, PMT detectors are still limited in most single molecule spectroscopy research due to its low quantum efficiency (< 20%) as well as its high level of dark noise, which can usually go up to 100 counts per second. With the advancements in semiconductor technology, the APDs detectors have become the standard detectors in single molecule fluorescence measurements. The APD detectors are manufactured as self-contained single photon counting module (SPCM) that is capable to detect single photons of light over a broad wavelength range, typically from 400 nm to 1100 nm and the sensitivity often outperforms a PMT detector. The APD detectors have extraordinarily high quantum efficiency >60% over entire visible wavelength range and peaks at about 700 nm where the efficiency approaches 90%. The photodiode is both thermoelectrically cooled and temperature controlled, ensuring the stable performance immune to ambient temperature change and at the same time, maintaining the low level of dark noise of ~20-50 counts per second. In terms of temporal response, count speed exceeding 20 million counts per second is achieved, which corresponds to a time resolution of 500 *ns*. The only limitation of the APD detector compared to the PMT detector is the small active area with diameter of up to ~200 μm. Interestingly, the small aperture of the detectors presents an excellent match to the confocal optical geometry of single molecule detection, as the sensitive area of the photodetector can serve as the confocal pinhole. .

While maximizing the collection of the emitted fluorescence signal, the background noise needs to be minimized at the same time. The background noise generated in single molecule fluorescence measurement is complex since it represents an overall noise from various noise sources. Herein, the major noise sources and the corresponding methods for reducing noise are discussed. The background noise can be generally categorized into two groups: sample-related noises and instrument-related noises. The noise arising from the sample is more difficult to suppress. Three types of noises are sample-related. First, elastic Rayleigh scattering occurs when solvent molecules or the host matrix in the probe volume scatters the incident photons at the same frequency. Therefore, Rayleigh scattering usually appears in a different wavelength range from the fluorescence emission and can be effectively reduced in single molecule measurements by using holographic notch filters. Second, besides Rayleigh scattering, the solvent molecules or the host matrix can generate Raman scattering by scattering photons which are typically red-shifted into the spectral region of the fluorescence emission. A suitable filter set can be employed to minimize the Raman scattering from solvent/host matrix. if there is sufficient spectral separation. The Raman signal can be treated by selecting excitation laser frequencies to move the Raman lines away from the fluorescence. Third, residual fluorescence from unwanted impurities can occur when the sample matrix is present in the laser probe volume, the undesired impurity molecules or structural components of the sample matrix, especially in biological samples in which many molecular components naturally fluoresce, could generate autofluorescence. Even if the quantum yield is low, the unwanted autofluorescence could still give rise to certain level of background noise. Similar to Raman scattering, the residual fluorescence can be

attenuated by employing high quality filters if there is sufficient spectral separation between impurity and analyte fluorescence. However, it is hard to completely suppress the residual fluorescence and Raman scattering in sample matrix without sacrificing the fluorescence signal from analyte molecule since both autofluorescence and Raman scattering signals are usually redshifted photons from excitation wavelength and are spectrally overlapping with the precious fluorescence signal from analyte molecule. This issue is solved by using multi-photon fluorescence excitation [77, 78]. When exciting the single analyte molecule by simultaneously using multiple long-wavelength photons, typically longer than emitted fluorescence, the generated Raman scattering does not contribute to the background noise since the scattered photons are redshifted from the excitation laser wavelength, while the fluorescence is blue-shifted.

The non-sample related noises are generally generated by the instrumentation. Major sources include the dark noise of the detector, the laser intensity fluctuation, the shot noise of photon counting and the readout noise in the electronics. The causes of these noises as well as the approaches to minimizing them have been detailed earlier.

The major considerations to improve the SNR of single molecule fluorescence detection have been discussed above. Basche *et al*. provided a quantitative assessment of the SNR for fluorescence detection of a single molecule. The equation is defined as:

$$SNR = \frac{D\Phi_F\left(\frac{\sigma_P}{A}\right)\left(\frac{P_0}{h\nu}\right)T}{\sqrt{\left(\frac{D\Phi_F\sigma_P P_0 T}{Ah\nu}\right)+C_b P_0 T+N_d T}} \qquad [2.16]$$

where Φ_F is the quantum yield of fluorophore, σ_P represents the absorption cross section, T is the time interval of signal acquisition, A is the cross section area of the excitation beam, C_b corresponds to background count rate per watt of laser power, D is an

instrument factor, typically within a range of 1% to 8%, N_d is dark count rate, and $\frac{P_0}{h\nu}$ as a whole, represents the number of incident photons per second [49, 79].

2.3.2. Major techniques for single molecule fluorescence detection

In the previous section, the basic requirements for achieving single molecule detection have been discussed in detail. Then what techniques can satisfy these requirements and lead to the successful probing of single molecules? Several optical microscopy techniques have demonstrated their power in single molecule measurements. Herein, several major types of microscopic techniques are briefly introduced.

2.3.2.1. Near-field scanning optical microscopy (NSOM)

The extraordinary characteristic of NSOM is its small laser probe volume beyond the diffraction limit since the size of the probe volume in NSOM is governed by the diameter of an aperture employed in the system, instead of the optics. Figure 2.13A illustrates the schematic diagram of NSOM. An aperture, typically at tens of nanometers in dimension, is usually created in front of the illumination light source. Since the wavelength of the incident photons is much longer than the diameter of the aperture, only a tiny portion of the light leaked out of the aperture can be applied for detection. An optical fiber (OF) is used to direct the illumination light to the location to be imaged. The light source is kept at a very short distance from the sample, in the near field, to limit the source size. Because of this confinement, NSOM offers a spatial resolution of tens of nanometers. This fact limits the NSOM to be applied in studying biological systems since this technique is not allowed to probe the region deep inside of the system such as the interior of cells [49, 67, 80].

2.3.2.2. Confocal microscopy

Similar to NSOM, confocal microscopy is introduced for single molecule detection as a scanning method. Image collection is accomplished by raster scanning of the laser probe volume across the sample or scanning the piezo-electric stage on which the sample is placed. Its simplified schematic diagram is presented in Figure 2.13B and the detailed principles have been aforementioned. It offers a suitable level of SNR for single molecule detection, similar to that provided by NSOM. In general, a femtoliter-sized laser probe volume is used to reduce the background noise and a pinhole (typically with diameter of tens of micrometers) is applied in front of detector to eliminate the out-of-focus fluorescence emission, which significantly improves resolution and image contrast. Although with a diffraction limited spatial resolution, as a far field imaging technique, confocal microscopy provides the capability of optical sectioning which enables the single molecule detection into a thick specimen.

2.3.2.3. Total internal reflection (TIR) microscopy

Total internal reflection microscopy is another type of far-field microscopy techniques that provide high enough SNR for single molecule detection [81]. In TIR microscopy measurements, the fluorophore is excited by the incident photons in an evanescent field which is generated upon TIR at the boundary between high- and low-refractive index media. The TIR can be achieved by a prism or the objective lens itself, as illustrated in Figure 2.12 C and D. Because of the exponential decay of the evanescent field intensity, the excitation light can only propagate into the low-refractive index medium for ~150 *nm*. Thus, only the fluorophores located within the ~150 *nm* of the boundary can be excited and this confines the probe volume to a thin layer, which greatly

minimizes the interfering background noise. However, with the issue of drastic decrease in excitation intensity, TIR microscopy can only approach a very thin region of specimen [82].

2.3.2.4. Single-molecule localization microscopy

The major conventional techniques for single molecule fluorescence detection have been introduced above. However, the resolutions of these far-field microscopic techniques are all limited by the diffraction limit (e.x. NSOM). In recent years, several super-resolution techniques have revolutionarily emerged to overcome the barrier of optical diffraction limit and achieve superior resolution and sensitivity of single molecule detection. In general, super-resolution imaging of single molecule can be achieved with both near-field and far-field microscopies. The near-field technique such as NSOM has its limitation to in-depth detection of thick samples and therefore, is not as commonly applied as far-field super-resolution microscopy. Herein, the far-field super-resolution microscopy is briefly introduced.

In far-field super-resolution microscopy, there are mainly two approaches to break the diffraction limit—patterned excitation and single-molecule localization. The patterned excitation approach (e.g. stimulated emission depletion microscopy or STED) is designed for imaging an ensemble of fluorophores in the specimen [83]. In contrast, single-molecule localization approach enables the imaging of individual fluorophores that are sparsely distributed in specimen with the distances between each other exceeding the Abbe resolution limit. Several popular super-resolution techniques relying on single-molecule localization include photoactivated localization microscopy (PALM), fluorescence photoactivation localization microscopy (FPALM) and stochastic optical

reconstruction microscopy (STORM) [84, 85]. In general, they are called single-molecule localization microscopy. Figure 2.13 illustrates the basic principles of single-molecule localization in two-dimension. The raw data—CCD image of a pixelated *PSF* of a single fluorophore (Figure 2.13A) is fitted to the Gaussian function by least-squares fit (Figure 2.13B). As a result of this fitting, each pixel on the original image is correlated to a spatial location on the image grid and the position (coordinates) of this fluorophore can be precisely localized as the center of the two-dimensional Gaussian function (Figure 2.13C). The Gaussian fit function is expressed as:

$$N_{xy} = B + N_{00} exp\left[-\frac{(x-x_0)^2}{2Wx^2} - \frac{(y-y_0)^2}{2Wy^2}\right] \quad [2.17]$$

where N_{xy} is the intensity at location (x, y) of the *PSF*, B is the overall background intensity (baseline), N_{00} represents the intensity at the center of *PSF*, (x_0, y_0) corresponds to the centroid of *PSF* and W_x and W_y is the *FWHM* of the *PSF*. With this approach, each single fluorescence emitter in the specimen can be localized with an accuracy of a few nanometers, which is determined by:

$$\sigma_{x,y} = \frac{S}{\sqrt{N}} \quad [2.18]$$

where S is the standard deviation of the intensity distribution of *PSF* of the fluorophore and N represents the number of fluorescence photons collected [86].

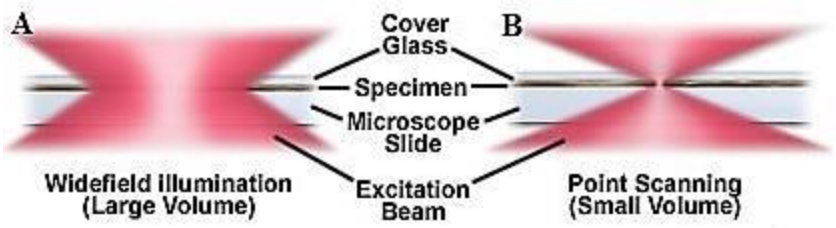

Figure 2. 1 Widefield illumination versus confocal point scanning of specimens

---

Note: (A) Conventional widefield illumination; (B) Confocal point scanning.

Source: http://olympus.magnet.fsu.edu/primer/techniques/confocal/confocalintro.html.

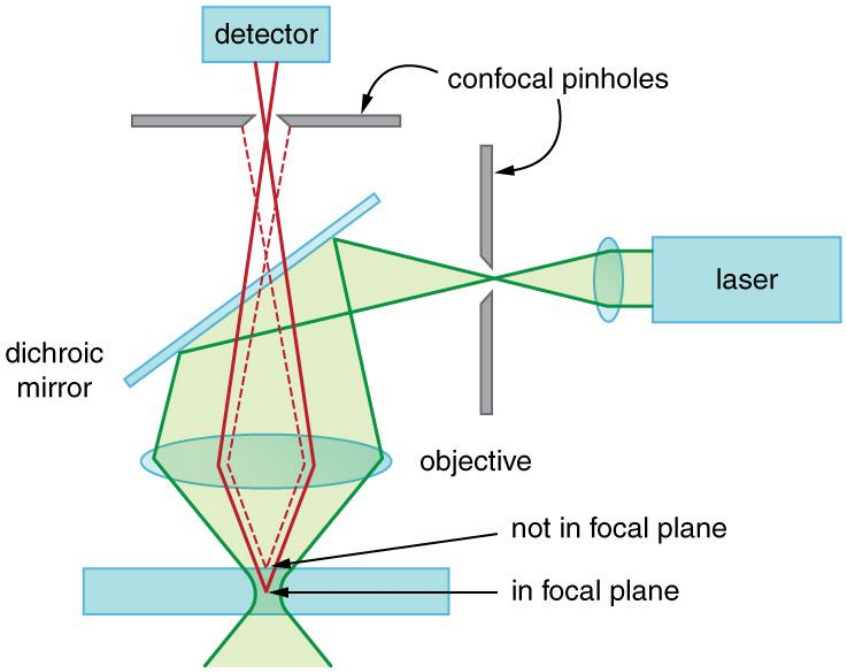

Figure 2. 2 Simplified light path in a typical confocal microscope

---

Note: the green solid lines represent the excitation light beam generated by a laser; the red solid lines represent fluorescence emission in the focal plane; the red dashed lines represent fluorescence emission out of the focal plane.

Source: Duproz A. Magnetic fluorescent nanoparticles for targeted drug delivery and treatment of CNS tumors. http://lppd.bioe.uic.edu/thesis/AlexandraDUPROZ.pdf.

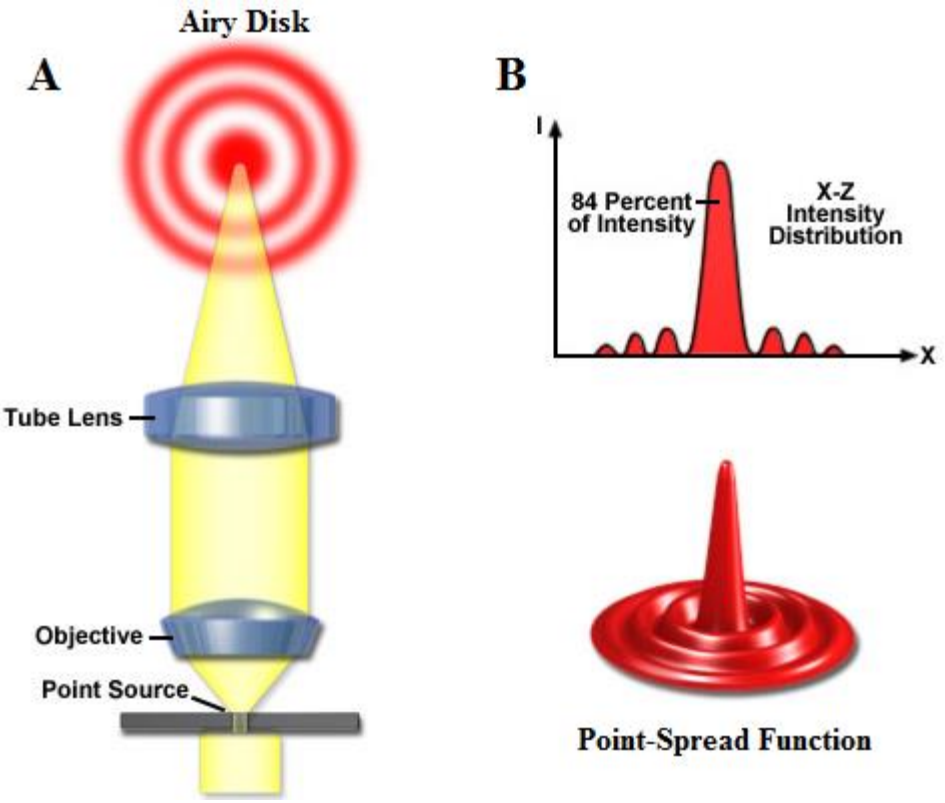

Figure 2. 3 The Airy disk and point spread function (*PSF*)

Note: (A) Illustration of the Airy disks; (B) Three-dimensional representation of the diffraction pattern known as *PSF* and X-Z projection to indicate the intensity distribution of *PSF*.

Source: http://zeiss-campus.magnet.fsu.edu/articles/basics/resolution.html .

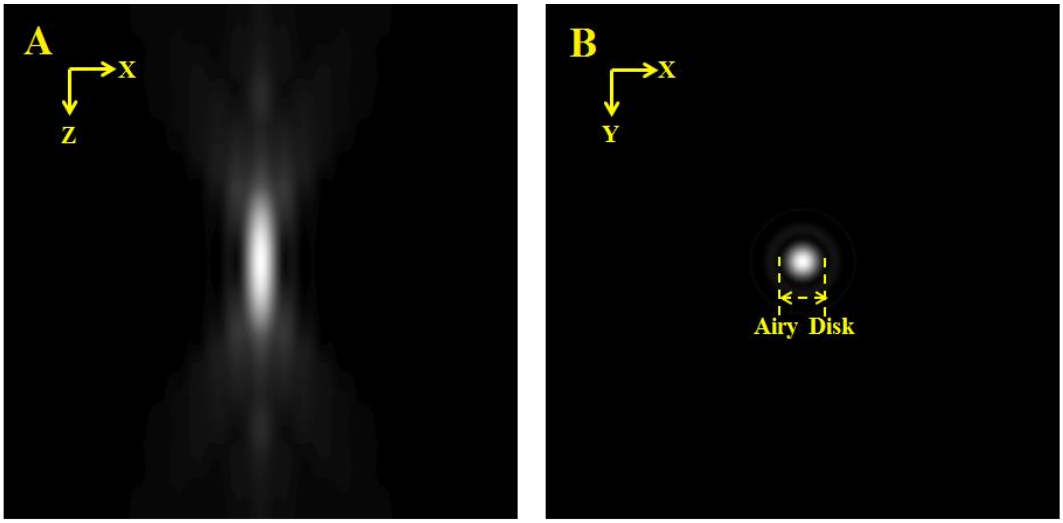

Figure 2. 4 Ideal computation results of 3D-*PSF* of a single point object

---

Note: (A) XZ projection of the 3D-*PSF*; (B) XY projection of the 3D-*PSF*, the central maximum of Airy pattern is defined as the Airy disk and its diameter is known as 1 Airy unit (*AU*).

Source: adapted from [32].

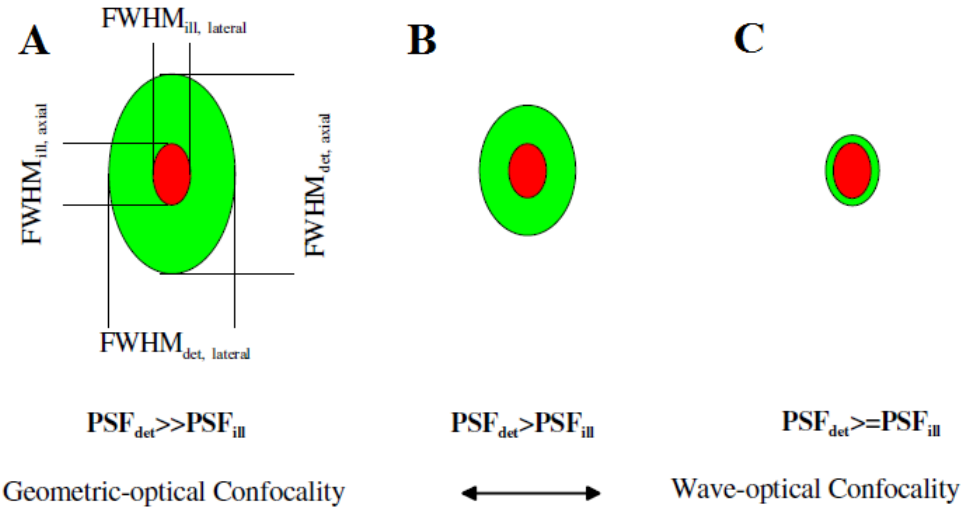

Figure 2. 5 Influence of pinhole diameter on confocality in confocal microscopy

---

Note: (A) Rules of geometric-optical confocality dominate when the pinhole diameter is about several Airy units; (B) Transition from geometric-optical to wave-optical confocality when pinhole diameter is about 1 *AU*; (C) Wave-optical confocality rule dominate when pinhole diameter is much smaller than 1 *AU* (e.g. 0.25 *AU*).

Source: adapted from [32].

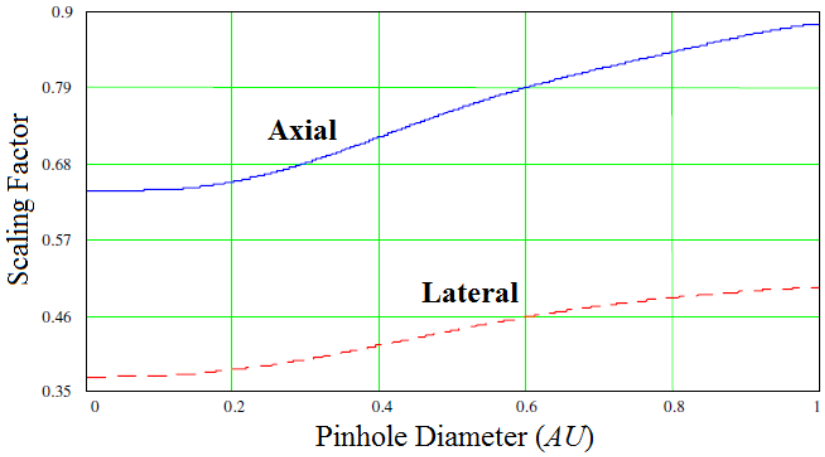

Figure 2. 6 Theoretical scaling factor in equations [2.6] and [2.8] for pinhole diameter between 0 and 1 AU

Source: adapted from [32].

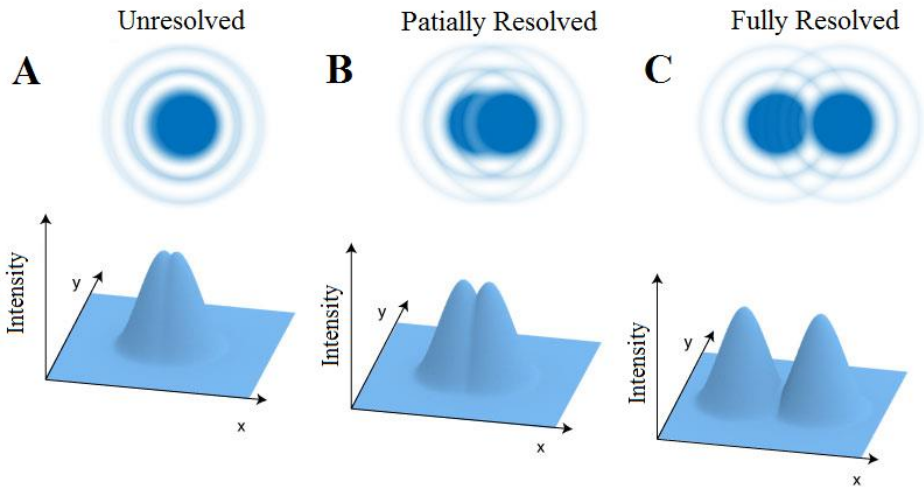

Figure 2. 7 Illustration of the Rayleigh criterion by individual diffraction patterns of two point sources

---

Note: The upper panel represents the diffraction patterns of two point sources and the lower panel shows the intensity distributions of the corresponding 2D-*PSF*. (A) Distance between two sources is so small that two patterns are not resolved; (B) Two sources are partially resolved with such a distance that the angular separation just satisfies the Rayleigh criterion; (C) Two sources are far apart and the two patterns are fully resolved.

Source: http://hedberg.ccnysites.cuny.edu/F15-PHYS208/p/presenter.php?topic=waveoptics&l=cal#/75.

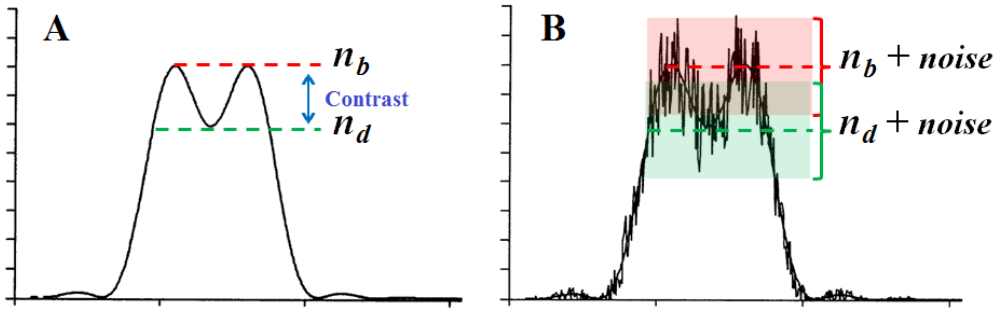

Figure 2. 8 Effects of image contrast and noise on resolving power of confocal imaging

---

Note: Elaboration of image contrast and the role of noise in affecting practical resolving power of confocal imaging. (A) Two points with equal maximum intensity separated by a distance that satisfies Rayleigh criterion. n_b and n_d, the intensities of the brightest spot and the "dip" between the two peaks, are used to define contrast by equation [2.10]; (B) Two equally-bright points with inclusion of noise. Points still resolvable according to the Rayleigh criterion but the "dip" between the two peaks may not be clearly observed because of the interference from noise fluctuation.

Source: adapted from [15].

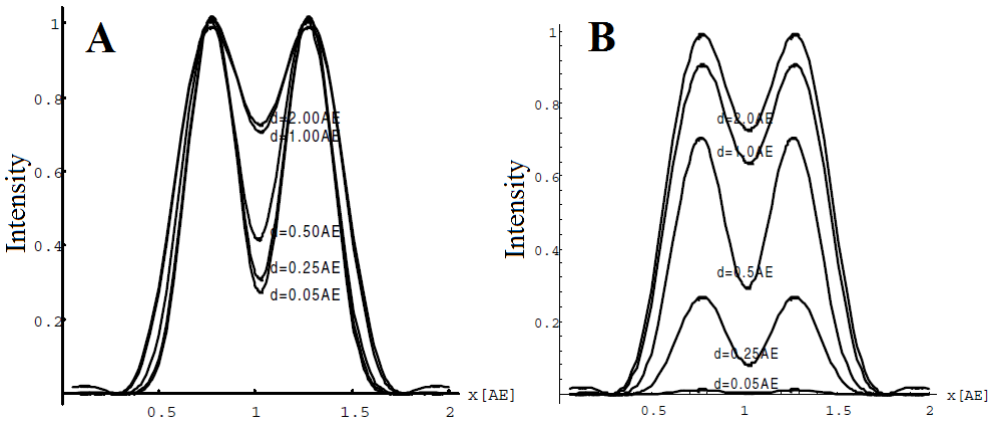

Figure 2. 9 Intensity distributions of PSF_{det} of two point objects collected behind pinhole as the diameter of pinhole varies from 0.05 *AE* to 2.00 *AE* (*AE* = *AU*)

Note: (A) Normalized intensity distribution to demonstrate that smaller diameter of pinhole leads to improved resolution and contrast (smaller *FWHM* and deeper "dip); (B) Non-normalized intensity distribution to show the drastic drop in collected intensity when the pinhole size decreases, especially when the diameter is smaller than 1 *AU*.

Source: adapted from [32].

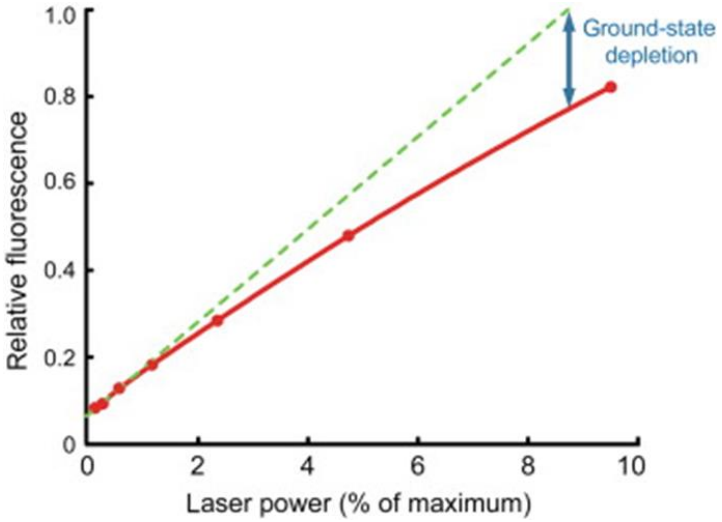

Figure 2. 10 Non-linear response of emitted fluorescence intensity to excitation laser intensity

---

Note: At lower laser power, emitted fluorescence linearly increases as the laser power increases. At higher laser power, emitted fluorescence intensity is less than the predicted value because of the ground-state depletion. The red solid line represents the actual response of emitted fluorescence to excitation laser power and the green dashed line represents the ideal (predicted) results.

Source: adapted from [36].

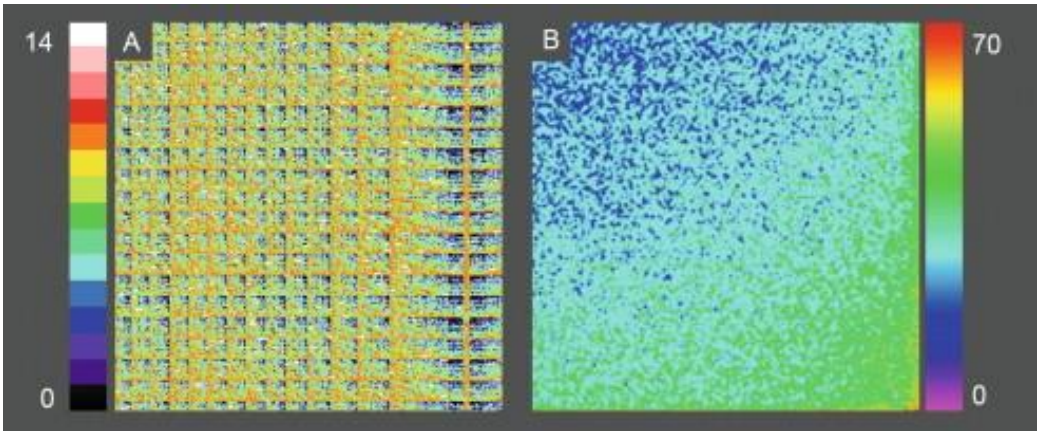

Figure 2. 11 Dark-current images collected by PMT and CCD detectors in confocal microscopy

---

Note: (A) 250 ×250 pixel dark-current image (16-bit) collected by PMT detector in Zeiss LSM510 confocal microscope. Random fluctuation of intensity that is generated by the dark noise of detector is displayed. Intensity ranges from 0 to 14 counts; (B) 512×512 pixel dark-current image (64-bit) collected by CCD detector. A patterned intensity shift is presented as the intensity increases along the lower right corner. Intensity ranges from 0 to 70 counts.

Source: adapted from [36].

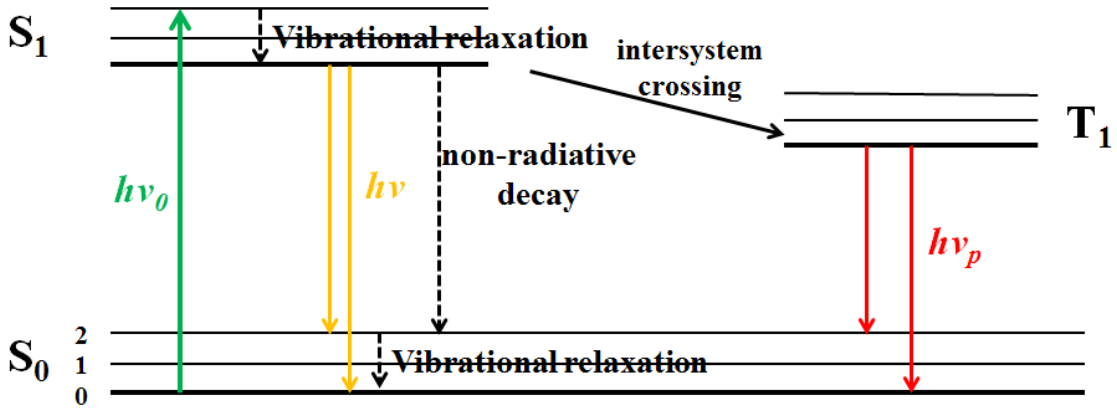

Figure 2. 12 Simplified Jablonski diagram of the electronic energy level structure of fluorescence

---

Note: S_0: electronic ground state; S_1: first excited singlet state; T_1: lowest excited triplet state; $h\upsilon_0$: absorption; $h\upsilon$: fluorescence emission; $h\upsilon_p$: phosphorescence emission.

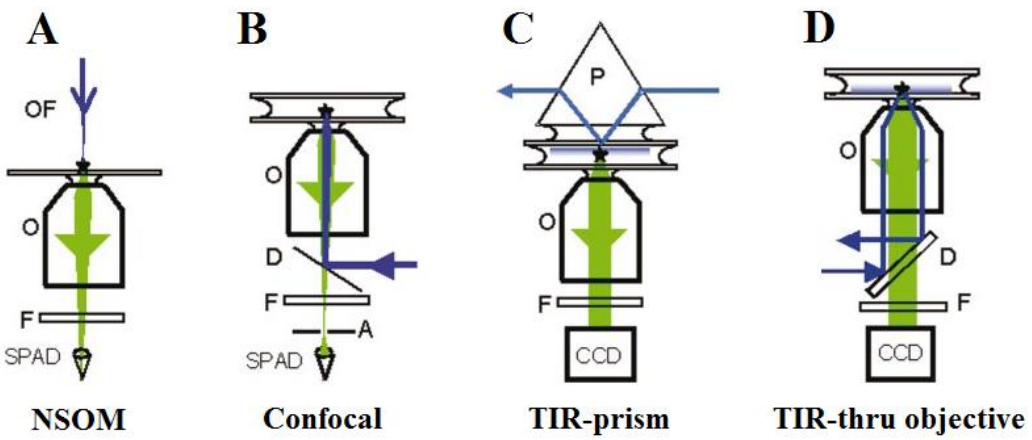

Figure 2. 13 Schematics of the main techniques for single molecule fluorescence detection

---

Note: (A) Near-field scanning optical microscopy. OF: optical fiber representing a illumination source that is closed to the sample surface, O: objective, F: filters, SPAD: single photon avalanche diode; (B) Confocal microscopy. D: dichroic mirror (beamsplitter), A: aperture (pinhole); (C) Total internal reflection microscopy using a prism. P: prism, CCD: charge-coupled device two-dimensional array detector; (D): Through-the-objective configured total internal reflection microscopy.

Source: adapted from [49].

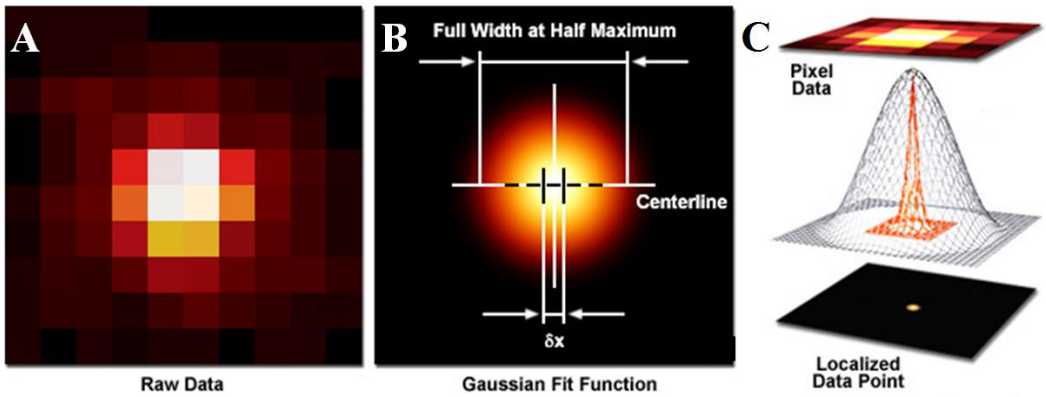

Figure 2. 14 Principles of single-molecule localization microscopy

---

Note: (A) Image of a single point source that is collected by CCD detector; (B) Two-dimensional Gaussian function that is applied as model for fitting; (C) Illustration of single-molecule localization process by showing the Gaussian profile of *PSF* sandwiched between raw data and the localized point after data processing.

Source: http://zeiss-campus.magnet.fsu.edu/print/superresolution/palm/practicalaspects-print.html .

CHAPTER 3

BACKGROUND SIGNAL MINIMIZATION FOR SINGLE MOLECULE FLUORESCENCE SPECTROSCOPY OF SILICA

3.1. Introduction

Initiated in late 1980's, single molecule spectroscopy (SMS) has developed into a powerful spectroscopy method extensively used in the field of biosensing and biological structure characterization. Central to the popularity of SMS is its capability of probing local structural heterogeneity and dynamics of individual molecules, a tremendously useful capability in biological sciences and meterials science.

A number of advantages make single molecule spectroscopy a powerful tool for probing the structure and dynamics of molecular systems. First and most importantly, only one molecule is measured at a time. Therefore, unlike the traditional bulk measurement which leads to an ensemble average, single molecule spectroscopy creates a distribution of molecular properties by monitoring a large number of individual molecules that sample and report all parts of the distribution. Second, synchronization of molecules experiencing time-dependent events, which is required in ensemble measurements, can be eliminated since the dynamics between different states or steps is approachable with single molecule detection. Thirdly, since single molecule spectroscopy monitors individual molecular events by measuring one specific molecule through repetitive excitation or hundreds molecules individually, rarely occurring events are accessible to single molecule spectroscopy [87]. For example, Adams group has studied the rare photoinduced intramolecular electron transfer (a slow charge transfer) in

perylenebisimide chromophores combined with oligophenylene bridges by using single molecule fluorescence spectroscopy [88] .

By taking advantages of the high sensitivity of fluorescence spectroscopic measurements of single molecule events in science have largely relied on fluorescence detection. An early breakthrough using this technique was reported by the Yanagida and coworkers in 1995. This group incorporated epifluorescence with total internal reflection microscopy to approach the visualization of single fluorescent molecules. They labeled ATP and myosin with two different fluorophores and achieved the monitoring of ATP-turnover of myosin at single molecule level [89]. Following this pioneering accomplishment, single molecule fluorescence spectroscopy has been extensively employed in biophysical studies including protein conformational dynamics, folding kinetics and DNA probing in living cells [90-98]. Especially, its combination with Forster resonance energy transfer (FRET) has been widely engaged in the studies of single protein's conformational dynamics including the folding and unfolding process, measurement of intramolecular distances as well as the characterization of structural heterogeneity in biological complexes [94, 99-106]. In a recent report, Schuler group successfully studied fast single protein dynamics in nanosecond scale in live eukaryotic cells by applying confocal single-molecule FRET spectroscopy. To enable the intracellular single molecule spectroscopy, Schuler and co-workers introduced FRET-labeled protein molecules into live eukaryotic cells with microinjection. The microinjection was chosen to ensure best reproducibility of the amount of injected proteins and also, shorten the time delay between injection and fluorescence detection. Dye molecules with excitation wavelength above 520 nm were selected to avoid the

cellular autofluorescence which could be interference on the single molecule signal from target molecules. Their success in measuring the nanosecond scaled dynamics of a naturally disordered protein as well as its conformational distributions has demonstrated the potential of this methodology in resolving sub-nanometer scaled dynamics in *vivo* [98].

Beside the merits demonstrated in various applications, there is always a crucial consideration to achieve single molecule detection- minimizing the background signal and increasing the signal-to-noise ratio (SNR). Among all types of background signals, scattering at the interfaces and in the bulk of the sample used to be one of the major contributors. To reduce or reject the scattered excitation laser light, it is crucial to have a small detection volume to minimize the number of scattering sources. Hence, single molecule spectroscopy with confocal geometry has gained great prestige in the field [107-111]. There are several reasons for the popularity of confocal microscopy in single molecule detection. (1) At the diffraction limit, a confocal microscopy system provides a sub-femtoliter focal volume of the excitation laser to sufficiently reduce the scattering signal. (2) The small probe volume also minimizes the probability of fluorescent impurity molecules from interfering with the measurements. (3) The optical pinhole in the confocal microscopy system is able to significantly reduce the disturbance from out-of-focal-plane autofluorescence. Combining confocal fluorescence microscopy and single-pair FRET, Leuba and coworkers investigated interactions between individual DNA and protein molecules. The DNA and the protein were labeled with a fluorescent donor and acceptor pair and the conformational dynamics of the DNA/protein complex was monitored at single molecule level by following the donor-acceptor distance [110]. Rigler group demonstrated a highly sensitive method of quantitative single-molecule imaging

using confocal laser scanning microscopy. They recorded the images of single diffusing fluorescent molecules through fast scanning and analyzed the molecular events captured on the image according to the fluorescence intensity distribution. This work enabled the direct measurement of single molecule's diffusion coefficient without applying autocorrelation analysis and determination of number of molecules [27].

Our research group has been investigating molecular transport in nanoporous silica with single-molecule confocal fluorescence spectroscopy [109, 112]. Using a home-built stage-scanning confocal microscope with the capability of single molecule detection, our former group member, Dr. Zhenming Zhong studied the reversible molecular adsorption of individual cationic fluorescent molecules Rhodamine 6G at reversed-phase chromatographic interface, nanoporous silica particles surface-modified with a C_{18} hydrocarbon monolayer. His study revealed that these strong adsorptions are very rare events, consisting only 0.3% of the observation time, and that these events possess a broad distribution of desorption time, from several milliseconds up to seconds with an average residence time of 61 *ms*. This work provided an in-depth understanding of the peak tailing issue in chromatographic separation. As a continuation of Dr. Zhong's work, by coupling single molecule fluorescence spectroscopy with confocal ratiometric imaging, Dr. Claudiu Brumaru investigated the polarity distribution in the network of nanopores of C_{18}-derivatized silica particles. He selected Nile Red, a polarity-sensitive fluorophore, as the local environment reporter [113-115] and tracked single Nile Red molecule's reversible adsorption at the nanopore interfaces. A large population of adsorption events was monitored, revealing a multi-modal polarity distribution of the adsorption sites on the nanopore surfaces [116].

The confocal fluorescence single molecule detection is achieved when individual fluorophores or individual fluorescently-labeled biomolecules diffuse through the focal volume of the confocal microscope. As the result of a very small focal volume, the target molecule typically spends a short amount of time (milliseconds) in the beam and before diffusing out of the observation boundary. Fluorescence emission usually occurs at nanosecond time scale, determined by the fluorescence lifetime,and hence, the fluorescent molecule undergoes multiple cycles of excitation and emission before leaving the focal volume. The total fluorescence signal from a single molecule is the accumulation of all emitted photons. However, even with detectors with high quantum efficiency such as avalanche photodiodes (APD) and optimized collection optics, only a few hundreds photons can be collected from each molecule at sub-millisecond integration time dictated by the molecular diffusion [112, 117]. On the other hand, as demonstrated in previous group members' work, the concentration of fluorophores needs to be at picomolar range for single molecule measurements [109, 116]. Based on Poisson statistics, for a 50 *pM* fluorophore solution, the probability of observing one molecule in the focal volume is about 1%. It indicates that for the other 99% of the time, there are no target fluorescent molecules diffusing across the observation volume and therefore any signal in this time period is from fluorescent impurities, if scattering is sufficiently eliminated. These limitations in low intensity of single-molecule photon bursts and in low frequency of target fluorophores lead to a crucial demand for an "absolutely clean" system ideally without any fluorescent impurity molecules in the background. Appearance of impurity molecules even in the picomolar concentrations could easily interfere or even overwhelm the signal from target fluorophores.

The main goal for this chapter is to develop and establish a system with "absolutely clean" background that satisfies the stringent requirements for confocal fluorescence detection of individual molecules. The outcome of this study creates a "standard" sample preparation protocol for experiments at single molecule level in our research group. Previous single-molecule studies of strong adsorption in this research field have been conducted on pristine surfaces of silica slides where background fluorescence can be readily minimized. Our group is the first in the field to probe molecular events in real nanoporous silica particles, advancing the molecular understanding of transport phenomena in the nanopores. Background signal, both scattering and impurity fluorescence, poses a much more challenging issue in these particles. The work described in this chapter builds an important foundation for this research field.

3.2. Experimental

3.2.1. Chemicals and materials

Nile Red was obtained from Acros Organics (New Jersey, USA) and its structure is presented in Figure 3.1. Microscope coverslips (12-545-G, size 50×35 *mm*, thickness 0.13-0.17 *mm* and S175212, size 25×25 *mm*, thickness 0.13-0.17 *mm*) were purchased from Fisher Scientific (Fair Lawn, NJ). The immersion oil (n = 1.515) for microscope objectives was a product from Cargille Laboratories Inc. (Cedar Grove, NJ). Optical glue (NOA 68) was obtained from Norland Products (Cranbury, NJ). Waterproof silicone grease was purchased from Dow Corning. HPLC grade acetonitrile used in this study was purchased from Fisher Scientific. The deionized water used in the experiments was freshly prepared with a MilliQ system procured from Millipore (Bedford, MA).

Two types of nanoporous silica particles were examined in this study. Luna C_{18}-derivatized silica particles were a gift from Phenomenex (Torrance, CA) and Kromasil C_{18}-derivatized silica particles were obtained from Akzo Nobel – EKA Chemicals (Bohus, Sweden). Structural properties of these particles are listed in Table 3.1.

3.2.2. Instrumentation setup

The experiments were performed on a stage scanning confocal microscopy system built on a Nikon Eclipse TE2000-U inverted microscope. This home-built instrument with capability of ratiometric single molecule measurement was designed and constructed by former Geng group members Mark Lowry, Zhenming Zhong and Gufeng Wang. The optical schematic diagram is illustrated in Figure 3.2A [109, 112, 118]. The 514.5 *nm* laser beam used in this study is generated by an air-cooled argon laser (35-LAP-431-220, Melles Griot). A spatial filter and beam expander removes the plasma emission and expands the excitation laser. The beam is directed into the backport of the microscope and reflected by a dichroic mirror (Z514RDC, Chroma) into an objective lens (100×, oil immersion, NA 1.45). The beam expansion ensures slight overfilling of the objective. The objective lens focuses the laser beam to a diffraction-limited point (focal volume) at the focal plane inside the sample which is placed on the piezoelectric scanning stage (Model: P-527.2CL, Physik Instrumente, Germany). The emitted fluorescence from the sample is collected by the same objective, transmitted through the dichroic mirror and a long-pass filter (Q530LP, Chroma) and focused onto the confocal pinhole (50 μm in diameter). After passing through the pinhole, the fluorescence signal is split into two separate channels for different wavelength ranges by a dichroic beam splitter (Q625LP, Chroma). The short-wavelength channel ("600 *nm*" channel) selectively collects

fluorescence signal with wavelength between 550 *nm* to 650 *nm* by using a band-pass filter (HQ600/100m, Chroma), while the long-wavelength channel ("650 *nm*" channel) detects the signal between 612.5 *nm* to 687.5 *nm* with a HQ650/75m band-pass filter from Chroma. The transmission spectra of the filters are shown in Figure 3.2B. The detectors are avalanche photodiodes—APDs (SPCM-AQ, PerkinElmer Optoelectronics) that have photon detection efficiencies of over 65% at 650 *nm*.. For each detected photon, the APD outputs a TTL pulse. The pulses are then counted by multichannel scalars (MCSs) installed in a personal computer. To facilitate ratiometric single-molecule spectroscopy with information from both channels, a trigger signal from one MCS is used to drive the other MCS to enable synchronization in photon counting [118].

3.3. Results and Discussions

Great effort has been brought into play for the minimization of the background signal in confocal single molecule spectroscopy measurements. Two general aspects are evaluated in this study. One was to discover an appropriate sample configuration and preparation procedure. Basically, the goal was to develop "standard" guidelines for sample preparation that satisfies the stringent requirements for single molecule detection. The other aspect was to identify a good combination between particles and solvents to achieve a clean background free system.

3.3.1. Optimization of sample configuration and preparation procedure

At the beginning of this project, based on the advice from a former group member Claudiu Brumaru from the Geng group, samples were prepared following the previously attempted protocol:

(1) weight out ~0.05 *g* of Luna C18-derivatized silica particles and mix into a glass vial with ~3 *mL* of HPLC grade acetonitrile solvent (from Fisher Scientific);

(2) vortex the vial using a vortex mixer (Fisher Scientific, Pittsburgh, PA) at 900 *rpm* for 1min, followed by slow shaking on a rotatory mixer (Glas-Col®, Terre Haute, IN) at 100 *rpm* overnight to ensure complete wetting of particles;

(3) pipet out 10 μL of the suspension and deposit the mixture onto a square microscopic coverslip (25×25 *mm*);

(4) quickly cover the mixture with another square coverslip to avoid the solvent evaporation and seal the edges with silicone grease;

(5) place the prepared sample slide on the piezoelectric stage of instrument, set dwell time to 100 μs for the multichannel scalers, collect fluorescence photon counts at an excitation laser power of 0.3 *mW*.

Unexpectedly, the signal collection of this blank sample generated extraordinarily high fluorescence signal (almost saturating the detectors). The measurement was immediately terminated so as to protect the detectors. Two main sources of impurities were considered to be contributors to this unforeseen and intense background signal. One possibility was the fluorescent impurities from the silicone grease. When sealing the edges of the sample slide with the grease, the solvent in the sample mixture was inevitably in touch with the grease and any fluorescent impurity molecules would have been introduced into the sample. The other possible source of fluorescence background was fluorescent impurities intrinsic to the silica particles.

We identified the background as fluorescence emission instead of scattering because the longer wavelength channel at 650 *nm* showed much higher background photon counts than the shorter wavelength region (Figure 3.3 A and B). The Lorentzian peak of the Rayleigh scattering from the solvent centered at 514.5 *nm* would have shown the opposite trend. The Raman scattering from the solvent was also ruled out as the source of the intense background signal. The four major Raman bands of acetonitrile at 380, 921, 2256 and 2946 cm^{-1} would have appeared at 524.8, 540.1, 582.1 and 606.4 *nm*, and would also have generated stronger signal in the 600 *nm* channel.

To test the hypothesis of impurity in the grease enclosure, samples were prepared by sealing the slide with the N68 optical glue. The background fluorescence signal was drastically reduced to below the detector saturation level and data were acquired under the same instrument settings. Figure 3.3A and B show the background fluorescence signals collected from both "600 *nm*" and "650 *nm*" channels, denoted as MCS1 and MCS2 respectively. As illustrated in the figure, however, the impurity signal from the background is still noticeable and could easily overwhelm the single molecule fluorescent signal from target molecules. Moreover, a band-shaped non-zero background is clearly seen in the data traces for both channels. Indeed, the signal is consistent with the constant residence of molecules inside the probe volume, suggesting a fluorophore concentration far above the single molecule statistics predicted by the 50 *pM* concentration. It demonstrates the existence of inherent fluorescence impurity molecules in the Luna C_{18}-derivatized silica particles, primary source of the unexpected high level of background signal. In order to further minimize the interference of fluorescence impurities from the sample, a photobleaching process was introduced. The prepared sample slide was

exposed to intense laser beam for 10 minutes and during the process, the fluorescent impurity molecules in particles underwent photochemical degradation which permanently prevented them from fluorescing. Hereafter, the background signal of sample was collected, as presented in Figure 3.3C and D. A significant improvement in the "cleanness" of the system was observed. Compared to the samples without photobleaching in Figure 3.3A and B, , the non-zero bands in data traces for both channels have disappeared, and the data traces were now consistent with single-molecule burst structure. As illustrated in Table 3.2, for the data collected from MCS2, for instance, the average photon counts for the background signal without photobleaching is 16.3 *counts/100 μs*, while after photobleaching, it has decreased to 2.4 *counts/100 μs*. Furthermore, the background threshold, calculated as the average background photon counts plus three standard deviations in the background, is decreased from 31.1 *counts/100 μs* to 10.5 *counts/100 μs*. These values directly and quantitatively demonstrate that photobleaching is an effective approach in removing the fluorescence background.

Nonetheless, as shown in Figure 3.3C and D, photon bursts frequently appeared in the data traces after photobleaching. Each photon burst represents an individual fluorescent molecule diffusing through the nanopores across the laser probe volume. For the MCS2 channel, 0.59 % of photon bursts are above the threshold (Table 3.2), meaning that 0.59 % of the bursts are emission from the fluorescent impurities, rather than noise fluctuation.

These fluorescent impurity molecules were at equilibrium between the nanopore interfaces of particles and the solvent. In order to move the impurity molecules out of the

C_{18}interface, multiple washing steps were performed. Each washing step involved the overnight mixing of the suspension on a rotatory mixer to allow the system to reach equilibrium. The particles were precipitated out of the solution and the acetonitrile solvent containing impurity fluorophores was removed. The washing procedure was conducted three times for each sample. The particles were further treated by photobleaching before data collection. The resulting data was displayed in Figure 3.3E and F. The data traces denote a pronounced decrease in the frequency of photon bursts compared with Figure 3.3A-D, for both two detection channels. Quantitatively, the photon bursts arise from impurities eventually decreases from 0.59 % to 0.32 % for MCS2 (Table 3.2). The other significant benefit of the background reduction is the lowering of the threshold for single molecule detection. In the untreated particles, many photon bursts from the target molecules would have been buried in the background. Many more individual molecules are detected and stuied in each data trace after the cleaning procedure.

Even though the background signal was greatly minimized after these sample cleaning procedures and a relatively "clean" particle blank was achieved for single molecule spectroscopy, the system was still not the ideal choice for two reasons. (1) the photobleaching which was used to "kill" the naturally embedded fluorescent impurities in particles could also bleach the target molecules and (2) the particle washing procedure was cumbersome and time consuming. For these reasons, another brand (Kromasil) of C_{18}-derivatized silica particles was brought into investigation to determine if it could be an alternative of the Luna particles.

3.3.2. Effect of particle selection on background signal

The sample slide was prepared following the improved procedure described above for the Kromail C_{18}-derivatized silica particles. The detected signal in the time period of one data trace (~6.5 *sec*) for both MCS1 and MCS2 channels were presented in Figure 3.4A and B. There is no non-zero band in either data trace and photon bursts are few and far between in both detection channels. It demonstrates that Kromasil C_{18}-derivatized silica particles are free of inherent fluorescent impurity molecules and the developed sample preparation procedure does not bring additional fluorescent impurity into the particle-solvent system. Shown in Table 3.2, based on background photon counts in MCS2, Kromasil C_{18}-derivatized silica particles are the more suitable system for single molecule detection owing to a lower background threshold (6.4 *counts/100 μs*) and percentage of photon bursts originated from fluorescent impurities (0.29 %).

To further confirm the appropriateness of this particle-solvent system, single-molecule fluorescence studies were conducted in comparison with the background. Nile Red solution at 100 *pM* was freshly prepared in acetonitrile to ensure the single molecule level of measurements. 0.05 *g* of Kromasil particles were then added into 3 *mL* of this fresh solution and mixed overnight on the rotatory mixer. The sample slide of the 100 *pM* Nile Red particle mixture (denoted as Nile Red sample) was prepared and fluorescence photon bursts from individual Nile Red molecules were collected in both MCS1 and MCS2 channels (Figure 3.4C and D). The Nile Red fluorescence traces present a manifested difference from the signal of the background. Visually, it is clear that the photon bursts in the Nile Red data traces are much more frequent and intense. The percentage of photon bursts (generated from the diffusing Nile Red molecules) above

background threshold value of 6.4 *counts/100 μs* was calculated to be 7.46 %, which was much greater than 0.29 % for the background signal. It implied that the vast majority of the detected photon bursts were fluorescence signal from individual Nile Red molecules when they diffused through the network of nanopores within the laser probe volume.

Molecular diffusion was subsequently investigated since it was the most typical and common events the molecules undertake in the network of nanopores. The fluorescence intensity fluctuations in the data traces (Figure 3.4), attributed to random Brownian diffusion of the molecules through the nanopores across the probe volume, were correlated to reveal the occurrence of molecular diffusion as well as to estimate the average diffusion coefficient of molecules by applying fluorescence correlation spectroscopy (FCS). The fluorescence time correlation function is defined as

$$G(\tau) = \frac{\langle \delta F(t) \cdot \delta F(t+\tau) \rangle}{\langle F(t) \rangle^2} \qquad [3.1]$$

where <> denotes time average, *F(t)* is the fluorescence intensity, and *δF(t)* stands for the fluctuation of fluorescence intensity as deviation from the temporal average intensity. When molecules undergo translational diffusion through the Gaussian distributed probe volume, the autocorrelation function is described by

$$G(\tau) = \frac{1}{N}\left(1+\frac{4D\tau}{\omega^2}\right)^{-1}\left(1+\frac{4D\tau}{l^2}\right) \qquad [3.2]$$

where *N* represents the average number of molecules in the probe volume, *D* is the diffusion coefficient, ω and *l* are the lateral and axial radii of the probe volume, respectively. They were determined to be 0.24 μm and 1.01 μm at locations where the laser intensity drops to $1/e^2$ of its maximum value [112]. Figure 3.5A and B illustrate the

average autocorrelation functions of 200 data traces collected both in the blank and Nile Red sample. Both functions were fitted to the 3-D diffusion model in Equation [3.2] by non-linear least squares (NLLS) fitting and the fitting curves were also displayed in the figures. With known parameters of laser beam ω and l, the average diffusion coefficient D of fluorescent impurity molecules was calculated to be $2.74\times10^{-7}\ cm^2s^{-1}$ (Figure 3.5A) while the average D for Nile Red molecules was $9.33\times10^{-7}\ cm^2s^{-1}$ (Figure 3.5B). The fit for Nile Red correlation function was excellent and a second diffusion term was unnecessary. This fact provided further evidence that the molecular diffusion inside the nanopores was dominated by the Nile Red molecules and the interference from impurity molecules was negligible for single molecule detection.

3.4. Conclusions

In this chapter, "clean" blank systems were successfully developed and they were demonstrated to be suitable for molecular transport studies in confocal single molecule fluorescence measurements.

A sample preparation protocol for minimizing the background signal has been estabilished. Multiple extractive washing of particles with organic solvents followed by photobleaching can help decrease the background signal significantly.

Moreover, a better system was achieved for single molecule detection by using Kromasil C_{18}-derivatized silica particles which were free of embedded fluorescence impurities. This newly developed system allowed completing sample preparation in a facile and timely fashion since neither photobleaching nor washing was necessary. Comparison between blank system (Kromasil particle-acetonitrile) and 100 *pM* Nile Red

probed system was conducted by applying FCS. The results confirmed the suitability of this system for single molecule studies of molecular transport in nanopores.

Table 3. 1 Physicochemical parameters of the silica particles used in this thesis

Parameter	10 μm Luna C_{18} silica particle	10 μm Kromasil C_{18} silica particle
Pore diameter ($\AA$)	73 [a]	110 [b]
Pore volume (mL/g)	0.47 [a]	0.9 [b]
Total carbon (%)	17.84 [a]	20.10 [b]
Surface coverage ($\mu mol/m^2$)	3.04 [c]	3.46 [b]
Surface area (m^2/g)	256 [a]	320 [b]

Note: [a]: adapted from [116]; [b]: adapted from [119]; [c]: adapted from [120].

Table 3. 2 Summary of background signal minimization for single molecule fluorescence measurement

Particle type	No extra treatment		Photobleaching		Multiple washing and photobleaching	
Luna C_{18} silica particle	Ave. counts (counts/ 100μs)	16.3	Ave. counts (counts/ 100μs)	2.4	Ave. counts (counts/ 100μs)	2.5
	Detection threshold (counts/ 100μs)	31.1	Detection threshold (counts/ 100μs)	10.5	Detection threshold (counts/ 100μs)	10.1
	Burst (%)	0.98	Burst (%)	0.59	Burst (%)	0.32
	Comment: Non-zero bands; High frequency of impurity photon bursts		Comment: Non-zero bands eliminated; High frequency of impurity photon bursts		Comment: Non-zero bands eliminated; Low enough frequency of impurity photon bursts	
Kromasil C_{18} silica particle	Ave. counts (counts/ 100μs)	1.9	Not applied		Not applied	
	Detection threshold	6.4				
	Burst (%)	0.29				
	Comment: Non-zero bands eliminated; Much lower detection threshold; Low enough frequency of impurity photon bursts					

Note: The photon counts analysis listed above is indicated by the computational results of data collected in MCS2.

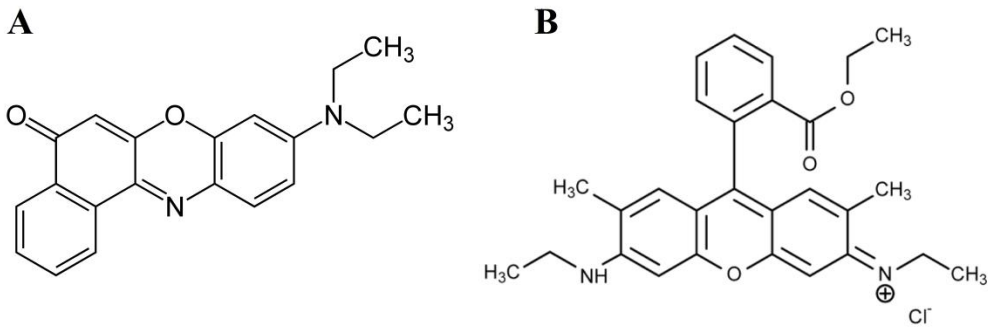

Figure 3. 1 Chemical structures of the main fluorescent molecules used in this thesis

---

Note: (A) Nile Red molecule, mainly used in Chapter 3 and 5; (B) Rhodamine 6G molecule, mainly used in Chapter 4 and 5.

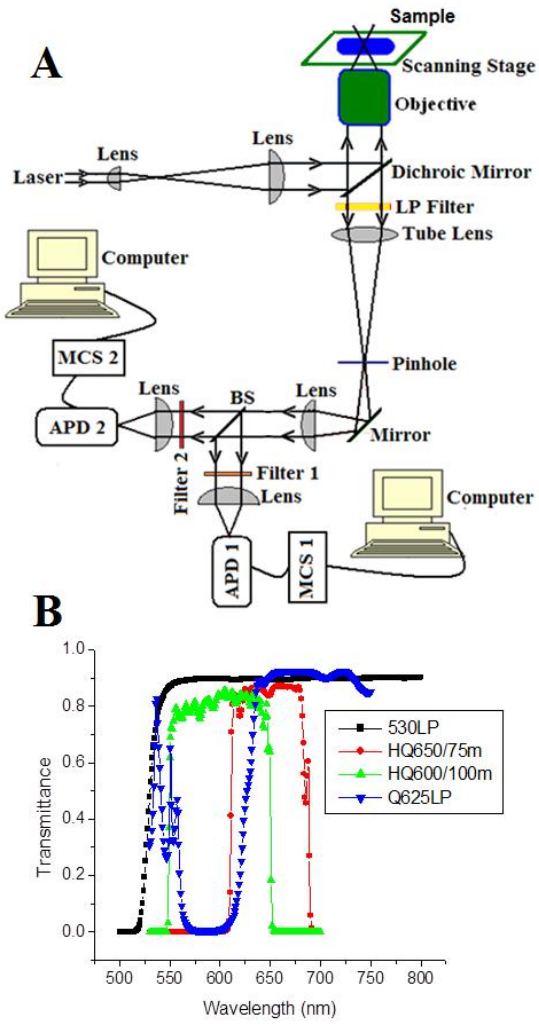

Figure 3. 2 Home-built confocal microscopy system for single molecule ratiometric detection

---

Note: (A) Schematic of the confocal imaging system. LP (LP530): long-pass filter with cut-on wavelength of 530 *nm*; BS (Q625LP): dichroic beam splitter (wavelength 625 *nm*); Filter 1 (HQ600/100 *nm*): band-pass filter centered at 600 *nm* with a bandwidth of 100 *nm*; Filter 2 (HQ650/75 *nm*): band-pass filter centered at 650 *nm* with a bandwidth of 75 *nm*; APD: avalanche photodiode detector; MCS: multichannel scalar; (B) Transmission spectra of LP, BS, Filter 1 and Filter 2 shown in (A).

Source: adapted from [109, 118].

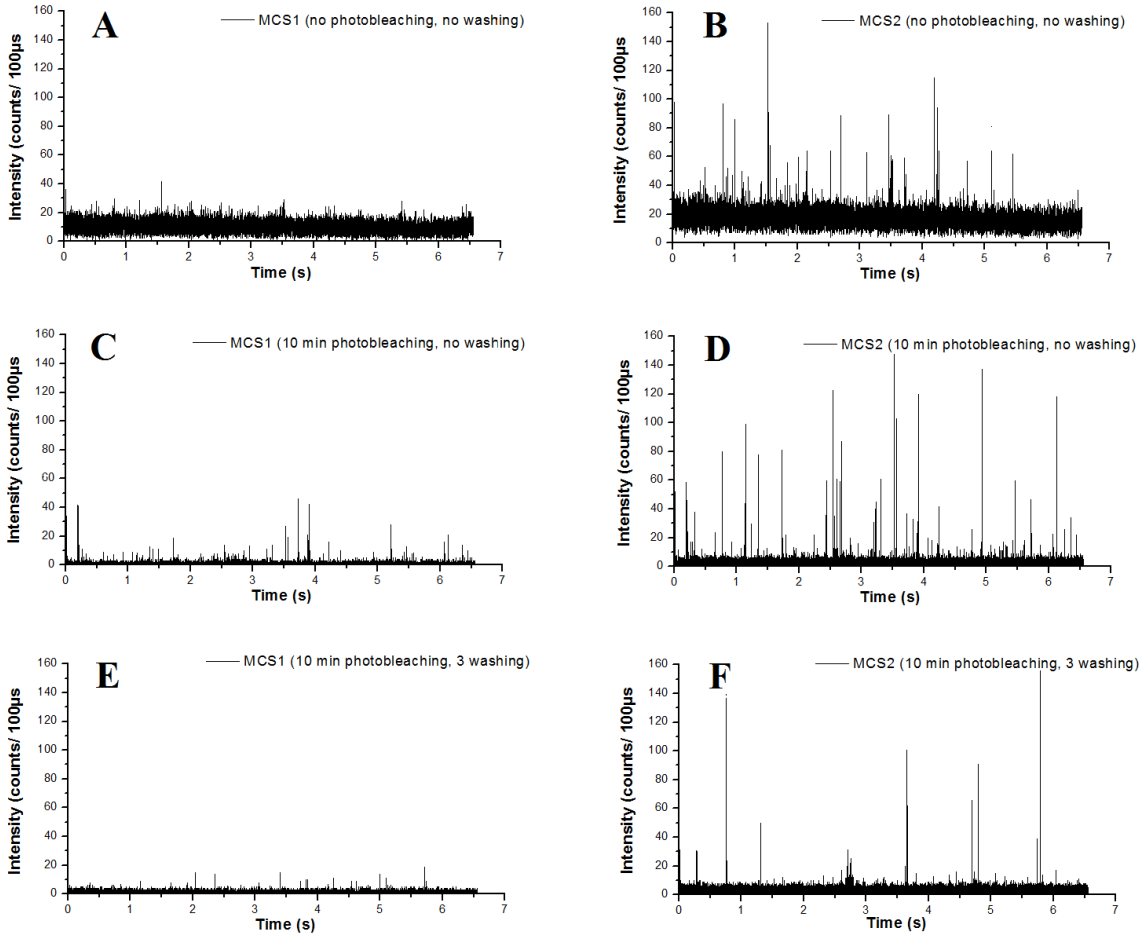

Figure 3. 3 Background signal minimizations of Luna C_{18} silica-acetonitrile system for single molecule fluorescence measurement

---

Note: (A) and (B): background signal without either photobleaching or washing of particles; (C) and (D): background signal with 10 minutes pre-photobleaching but without washing of particles; (E) and (F): background signal with 10 minutes pre-photobleaching as well as three times washing steps.

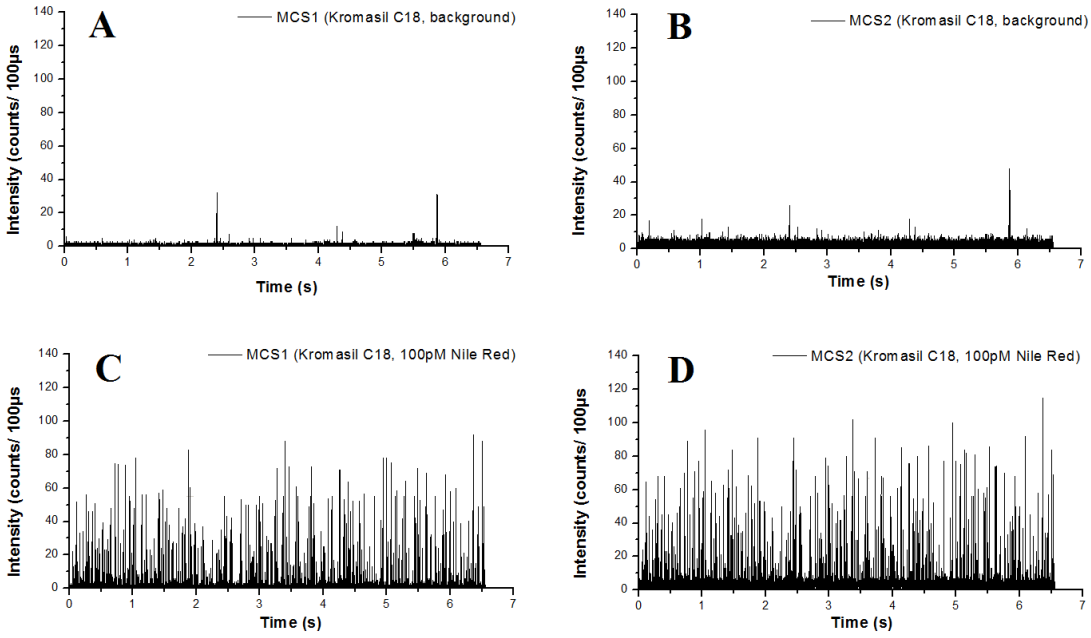

Figure 3. 4 Comparison between background and 100 *pM* Nile Red signal of the Kromasil C_{18}-acetonitrile system for single molecule fluorescence detection

---

Note: (A) and (B): background signal of the Kromasil C_{18}-acetonitrile system; (C) and (D): fluorescence photon bursts from 100 *pM* Nile Red in this system.

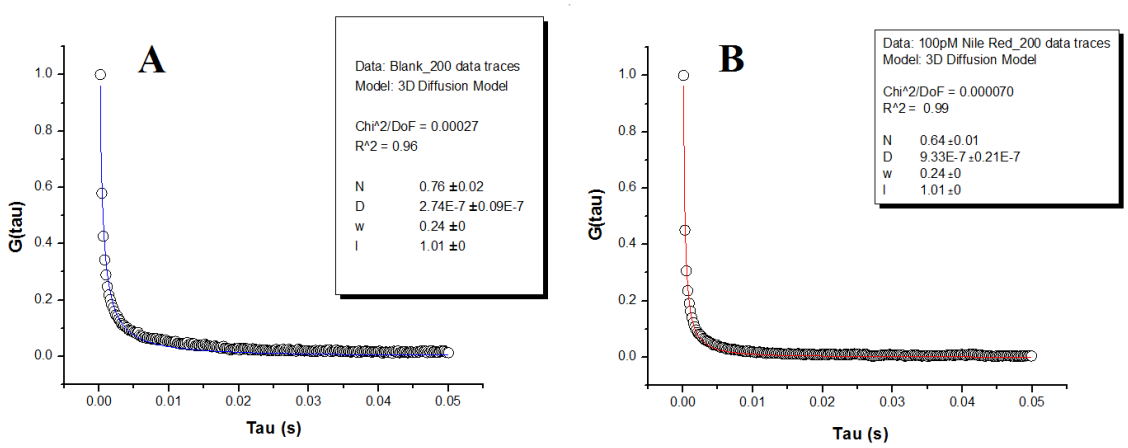

Figure 3. 5 Average autocorrelation functions of 200 data traces and corresponding NLLS fittings to the 3-D diffusion model

---

Note: (A) Average autocorrelation function of 200 data traces for blank sample of Kromasil C_{18}-acetonitrile and corresponding NLLS fitting to 3-D diffusion model. The average *D* of fluorescent impurity molecules in the probe volume is estimated to be ~2.74×10^{-7} cm^2s^{-1}; (B) Average autocorrelation function of 200 data traces for 100 *pM* Nile Red in Kromasil C_{18}-acetonirile system and corresponding NLLS fitting to 3-D diffusion model. The average *D* of individual Nile Red molecules in the probe volume is estimated to be ~9.33×10^{-7} cm^2s^{-1}. The lateral and axial radii of the beam are fixed in the NLLS fitting.

CHAPTER 4

SINGLE MOLECULE COUNTING IN NANOPORES

4.1. Introduction

As the evolutionary development of material technologies, the nanostructured materials have been widely employed in the applications of biosensing, chemical separation and drug delivery because of several unique properties, including high surface to volume ratio, great chemical and thermal stability, flexible surface modification as well as the intrinsic heterogeneities. The related physicochemical properties and microenvironments of various types of nanostructures have been extensively investigated for better understanding of the intrinsic features associated with materials and molecular interactions between the "host" material and "guest" molecules in certain applications. At early stage, for instance, mesoporous material has been characterized by X-ray diffraction (XRD) and transmission electron microscopy (TEM) [121, 122]. However, the kinetics information of the interactions between "guest" molecule and mesoporous material could not be approached since these techniques did not provide sufficient time resolution.

In the last decades, single molecule spectroscopy (SMS) has emerged to be a powerful tool with ultra-sensitivity to explore molecular behaviors at single molecule level. Because of its high spatial and time resolutions, SMS has been adopted for ultra-sensitive detection of single molecules in different fields [54, 123-131]. Compared to ensemble measurements, SMS is of great interest and exhibit superior advantages in probing heterogeneities of micro/nanoenvironments of the "host" material. When "guest" molecules are introduced into "host" material, they act as reporters of local environments, the unique features and properties of material thus can be revealed through the

measurements of "guest-host" interactions. This information is often obscured in bulk measurement due to the problem of ensemble averaging. With single molecule detection, on the other hand, the kinetics of the "guest-host" interactions as well as the heterogeneity of micro/nanoenvironments of "host" material can be resolved by measuring certain property of individual "guest" molecules overtime, which is always presented by an average value in bulk measurements. For example, the unsynchronized, sequence-dependent dynamics of HIV-1 reverse transcriptase during DNA polymerization process has been approached by monitoring the conversion of single-stranded DNA to double-stranded DNA overtime at single molecule level [132]. This information of enzymatic activity cannot be achieved in ensemble measurement.

One of the pioneered applications of single molecule detection in chemical separation science was to investigate the "defects" on the chromatographic interface [112, 130, 133]. Wirth group successfully detected the rare reversible adsorptions of "guest" molecules at surface of C_{18}-derivatized silica substrate by combining SMS and fluorescence autocorrelation spectroscopy [130]. By combining SMS and confocal microscopy, we have also reported the studies of reversible adsorptions of single molecules at interface of chromatographic beads which are rare, comprising only 0.3% of observation time, but play an important role on peak tailing issue in chromatographic separation [112].

Following the success of the first single molecule detection in biological sample in 1981 [134], this technique has been tremendously applied to look into various biological systems [126, 127, 135-137], migrating from in-*vitro* [138] to in-*vivo* [127, 139] studies. The information of many macromolecules with low quantity in live cells could then be

approached. The cellular processes of these macromolecules, such as transcription, translation and gene expression always exhibit high stochasticity and single molecule detection was proved to be a powerful tool to approach these stochastic processes [126]. For instance, the production of single protein molecule was directly observed in real-time [140]. The dynamics of transcription factor during gene expression, such as specific and non-specific bindings between single transcription factor and DNA molecule was explored [135]. The single molecule technique was also employed to reveal the genotypic switching happened in live cell [141].

Single molecule detection has also demonstrated its advantages in investigating environmental heterogeneity of nanostructured material [54, 125, 142-144]. Higgins group reported a study to reveal dynamics of acidity of microenvironments within sol-gel-derived silicate thin film by detecting individual pH-sensitive fluorophores at each single sites of the film substrate [54, 125]. Many nanostructures such as nanochannels and nanopores were characterized by tracking the transports of single molecules. For example, with single molecule confocal imaging, the diffusions of single molecules were directly visualized. The microscopic properties, structural defects, micro/nanoenvironmental heterogeneities of the material were uncovered by analyzing the trajectories of single molecular diffusion [123, 145].

In all categories of applications mentioned above, single molecule detection requires accurate counting of individual molecules, which is very challenging in practice because of the limited signal from single molecule and the significant contribution from interfering background signal. Several techniques such as total internal reflection and confocal microscopy are popular in single molecule counting. These two techniques earn

the popularity by providing small probe volume which helps decrease the Raman scattering from solvent/sample subtracts and increase single-to-noise ratio (SNR) which is essential to ensure accuracy of single molecule counting. Many researches were conducted and improvements were made to achieve precise counting of single molecules in various systems [146-152]. For example, Craighead group performed single molecule detection in sub-micron sized fluidic channels. This device presented great performance since it created smaller effective probe volume which significantly improved *SNR* and thus enabled the accurate counting of single molecule [146, 147].

In addition to improving SNR, single molecule counting also requires comprehensive analysis of photon bursts, which are the output signals and containing crucial information of individual molecules crossing probe volume. For instance, in the study of DNA fragment sizing at single molecule level, the information of sizes of DNA molecules were directly from the analysis of heights and widths of photon bursts [147].

Herein, in this chapter, we developed single molecule counting as a comprehensive analytical method to probe molecular transports in nanopores of silica with confocal single molecule spectroscopy, aiming to provide a protocol of interpreting photon burst data and better understandings of characteristics of molecules, photons as well as noise in single molecule counting.

Individual molecules were counted and localized into super-resolution ellipsoidal shells. The spatial distribution of molecules, the single molecule counting statistics and dependence on excitation power and molecular concentration were evaluated. The method provided fast time resolution for microsecond kinetic processes including

diffusion and adsorption, high spatial resolution for locating diffusing molecules into nanometer domains, and molecular resolution to record the distributions of physicochemical properties of the nanopores. The crossing of individual molecules through the confocal probe volume was examined with coefficient of clustering of photon bursts. The randomness of the crossing signified the absence of structural obstruction in the network of nanopores. The burst heights scaled linearly with the excitation power but not with molecular population. Instead, the molecular concentration was analyzed through single molecule counting. The statistics of single molecule counting was characterized by shot noise distribution that was reduced at higher concentration. The maximum intensities of photon bursts correlated with the trajectories of molecules with the ones diffusing closer to the center of the Gaussian beam emitting stronger bursts while ones crossing the peripheral of the beam emitting weaker bursts. Probability distribution function were established for the localization of molecules into super-resolution ellipsoidal shells that exhibited equal photon counts. Single molecule analysis showed that the nanostructures in the particle were uniformly distributed within the probe volume of ~460 *nm* and that there were no large obstacles of the molecular diffusion in the network of pores. Single molecule counting provides a powerful analytical tool enabling studies of physicochemical properties of nanopores.

4.2. Experimental

4.2.1. Chemicals and materials

Rhodamine 6G was purchased from Aldrich (Milwaukee, WI) and used as received. HPLC grade acetonitrile and microscope coverslips (12-545-G, size 50×35 *mm*, thickness 0.13-0.17 *mm*) were obtained from Fisher Scientific (Fair Lawn, NJ). The

deionized water used in single molecule measurements was purified by MilliQ system (MilliQ-Plus, Millipore, Bedford, MA). Immersion oil obtained from Cargille Laboratories Inc. (Cedar Grove, NJ) had a refractive index of 1.515. The 10-µm unmodified porous silica particles (Kromasil particles) were purchased from Akzo Nobel EKA Chemicals (Bohus, Sweden). The particles had an average pore size of 100 *Å*, surface area of 329 m^2/g and pore volume of 0.91 *mL/g*. A solvent composed of 90% acetonitrile and 10% water was used throughout the experiments in order to minimize background fluorescence signal.

4.2.2. Instrumentation and measurements

4.2.2.1. Sample preparation

The samples were prepared by adding dry Kromasil silica particles to 3 *mL* of Rhodamine 6G solution in 90% acetonitrile. The sample was sonicated for three minutes, followed by two hours of mixing on a rotatory mixer to ensure that the pores were completely wetted by the solvent. Approximately 15 μL of the prepared suspension was sandwiched between two microscope coverslips and sealed using optical adhesive to prevent solvent evaporation and movements of particles during fluorescence measurements.

4.2.2.2. Instrumentation and measurements

Single molecule counting was performed on a home-built confocal imaging system based on an inverted microscope (Eclipse TE2000-U, Nikon) [112]. The 514.5 *nm* laser beam provided by an air-cooled argon ion laser (Model: 35-LAP-431-220, Melles Griot) was expanded by a beam expander to slightly overfill the back of an oil immersion

objective (100×, 1.45 NA) for the optimal spatial resolution. The laser beam with a Gaussian profile was introduced into the backport of the microscope and reflected by a dichroic mirror (Z514RDC, Chroma) towards the sample stage. A microscope objective focused the beam to a diffraction-limited spot into the sample. The three-dimensional localization of the focal point was achieved by a piezoelectric microscope objective stepper along the axial (*z*) direction and a two-dimensional piezoflexure stage (Physik Instrumente, Germany) in the lateral (*x* and *y*) directions. The fluorescence emission from Rhodamine 6G was collected by the objective, transmitted through the dichroic mirror and focused on a 50-μm confocal pinhole at the image plane to reject the out-of-focus emission. The fluorescence was collimated and then split into two channels by a dichroic beam splitter (Q625LP, Chroma). The reflected fluorescence passed through a band-pass filter HQ600/100m and was focused onto the active area of an avalanche photodiode (SPCM-AQ, PerkinElmer Optoelectronics). The transmitted fluorescence passed through a band-pass filter HQ650/75m and was focused onto the active area of a second avalanche photodiode. The data acquisition was achieved by using multichannel scalers (MCS, Stanford Research System, Sunnyvale, CA) running on a personal computer to count individual fluorescence photons for each avalanche photodiode detector. The dwell (integration) time for data acquisition was 100 μs to ensure that the integration time is shorter than the characteristic diffusion time of Rhodamine 6G molecules across the probe volume.

4.3. Results and Discussions

We reported single molecule counting in nanopores for the characterization of molecular transport in porous silica particles. We firstly established that the molecular

distribution and diffusion in the nanopores were random processes in time and in space, with the temporal behavior of molecules closely following Poisson statistics, and spatial distribution modeled accurately by the point spread function (*PSF*) of the probe volume. Indeed, the photon counts of each molecule enable super-resolution localization of the molecule into an ellipsoidal shell a few nanometers in thickness. We then established the accuracy of single molecule counting by investigating the excitation power and concentration dependence. An interesting finding was that the noise in single molecule counting was described by the fundamental shot noise.

4.3.1. Temporal and spatial distribution of molecules in nanopores

Single molecule fluorescence data has the characteristic feature of burst structure. In the fluorescence time trace collected inside a nanoporous silica particle (Figure 4.1A), most of the time the background signal is below a few counts, generated from light scattering by the porous structure in the particle (inset of Figure 4.1A). When a molecule diffuses across the probe volume of the Gaussian laser beam, a burst of photons are emitted. Enumeration of molecules involves the counting of the number of photon bursts within a predefined integration time. In our confocal geometry of the single molecule experiment, a probe volume of ~0.3 fL is defined by a lateral beam waist of 0.23 μm and an axial length of 1.0 μm. A fluorephore concentration of 50 pM dictates a probability of 99%, 0.99% and < 0.005% for 0, 1 and 2 molecules in the probe volume, respectively. A low concentration of 50 pM thus ensures the discrete arrival of individual molecules through random walk, giving rise to discrete photon bursts. In the time window of 6.55 seconds in a fluorescence data trace in Figure 4.1A, about 2000 molecules were counted in the data trace. Fluorescence data in a 0.22 ms time window (Figure 4.1B and C)

demonstrated the protocol of single molecule counting. A burst searching program was applied to locate the photon bursts in the fluorescence data (Figure 4.1B), and the time of the burst at the peak location as well as the burst height was recorded. The molecule counting signal is plotted in Figure 4.1C with each molecule identified by its peak time and peak height. The burst times contain information about the randomness (or the lack of) of the molecular arrival; the peak heights information about the spatial locations of the molecules inside the probe volume; and the peak widths and shapes information about molecular diffusion [112, 153]. These parameters were explored and discussed in the following sections to probe the physicochemical properties of the nanopores.

The Brownian diffusion of the molecules in the nanopores is a random process and the temporal distribution—the molecules' arrival times in the probe volume—should follow Poisson statistics, leading to a Poisson distribution of the burst times. To test the randomness of single molecules, the fluorescence data trace was separated into a series of time windows (Figure 4.2A), the number of molecules in each time window was counted and the coefficient of clustering (CoC) for each time trace was calculated. The coefficient of clustering is a statistical parameter for analyzing the dispersion of events, and is calculated as the ratio of the variance to the mean of number of molecules in these time windows, $= \frac{S^2}{n}$, where n is the average number of molecules in each time window and S^2 is variance in the number of molecules. If the molecules are uniformly distributed into the time window, with exactly identical number of molecules in each window, the coefficient is zero. Figure 4.3A simulated this distribution of molecules. For random arrival of molecules into the prove volume, the number of molecules are described by Poisson statistics, and the coefficient should be close to unity. Figure 4.3B simulated the random

temporal distribution of molecules with an average of 10 molecules in each time window. The coefficient of clustering of 1.1 for this time trace signaled the randomness in the molecular events in the simulation. If there is molecular clustering or bunching in time, the coefficient will be significantly larger than one. This situation was simulated in Figure 4.3C, where the molecular events took an exponential decrease over time. The clustering was evaluated statistically by a coefficient of clustering at 2.8. Although the nanoporous particles were in equilibrium with a solution at constant concentration and thus a constant concentration was expected inside the nanopores, the molecular counts in 300 representative time windows in a time series in Figure 4.2B demonstrated the substantial fluctuations in the number of molecules, consistent with random arrival of the molecules into the probe volume. A 110 *ms* stretch of burst data shown in the inset of Figure 4.2B demonstrated the substantial fluctuations in molecular counts. In the five consecutive time windows, the number of molecules crossing the probe volume varied from 3 to 23 in each 22 *ms* window. The coefficients of clustering for 200 data traces were shown in Figure 4.2C, each calculated from 300 time windows in a trace. Their closeness to unity signified the randomness in the temporal distribution of the molecules and that the molecules navigated freely through the network of interconnected nanopores when they diffused in the particle, without significant hindrance or traps.

Intuitively, it has been hypothesized in burst analysis of single molecule spectroscopy that the heights of the photon bursts are determined by the trajectories of the diffusing molecules. If a molecule diffuses close to the center of the Gaussian laser beam, the strong excitation intensity leads to higher frequency of cycling the molecules between the ground and excited states and thus more intense photon bursts, while a molecule

diffusing through the peripheral areas of the laser beam experiences a lower excitation intensity and thus emits fewer photons.

To establish the trajectory theory of burst heights, extensive analysis of photon statistics in the single-molecule fluorescence data traces was performed. The confocal prove volume of the excitation laser beam is a three-dimensional Gaussian [154]:

$$I = I_m e^{-\left[\frac{x^2+y^2}{w_{x,y}^2}+\frac{z^2}{w_z^2}\right]} \qquad [4.1]$$

where I is the intensity at location (x, y, z) in space, I_m is the maximum intensity at the focal point of the beam (*0, 0, 0*), $w_{x,y}$ is the beam waist in the lateral dimensions (x and y) and w_z is in the axial (z) dimension along the optical axis of the microscope objective. The beam waist is defined as the location where the intensity has decreased to $1/e^2$ of the maximum intensity. The burst height of a diffusing molecule N in photon counts is proportional to the excitation intensity I.

$$N = N_m e^{-\left[\frac{x^2+y^2}{w_{x,y}^2}+\frac{z^2}{w_z^2}\right]} \qquad [4.2]$$

where N_m is the maximum burst height for a molecule when it diffuses through the center of the probe volume. Interestingly, a molecule that emits N photons at the peak of the burst can thus be located by

$$\frac{x^2+y^2}{w_{x,y}^2}+\frac{z^2}{w_z^2} = -\ln\left(\frac{N}{N_m}\right) \qquad [4.3]$$

or on the surface of a prolate ellipsoid defined by semi-principal axes of

$a = b = w_{x,y}\sqrt{-\ln(N/N_m)}$ and $c = w_z\sqrt{-\ln(N/N_m)}$.

In single molecule imaging, fluorescence intensity is in discrete photon counts, and a certain photon counts *N* corresponds to molecules that are located in an ellipsoidal shell confined by an inner surface $\frac{x^2+y^2}{\left(r_{in}w_{x,y}\right)^2}+\frac{z^2}{\left(r_{in}w_z\right)^2}=1$ defined by semi-principal axes of $a_{in}=b_{in}=w_{x,y}r_{in}$ and $c_{in}=w_z r_{in}$, and an outer surface $\frac{x^2+y^2}{\left(r_{out}w_{x,y}\right)^2}+\frac{z^2}{\left(r_{out}w_z\right)^2}=1$ defined by $a_{out}=b_{out}=w_{x,y}r_{out}$ and $c_{out}=w_z r_{out}$, where $r_{in}=\sqrt{-\ln\left[\left(N-0.5\right)/N_m\right]}$ and $r_{out}=\sqrt{-\ln\left[\left(N+0.5\right)/N_m\right]}$. The probability of finding molecules that emit *N* photons is thus proportional to the volume of this ellipsoidal shell:

$$P(N)=K\iiint_{U_{out}}\rho(x,y,z)dxdydz-K\iiint_{U_{in}}\rho(x,y,z)dxdydz \qquad [4.4]$$

in which *K* is the normalization constant for a unity probability over space, *ρ(x, y, z)* is the density distribution of the molecules in space determined by the structure of the pore network, and the regions U_{in} and U_{out} are bound by the two ellipsoids.

For a porous membrane when the optical axis is aligned with the pore direction, the molecular density distribution is a two-dimensional function and the probability reduces to

$$\begin{aligned}P(N)=&K\int_{-r_{out}w_{x,y}}^{r_{out}w_{x,y}}\int_{-\sqrt{r_{out}^2w_{x,y}^2-x^2}}^{\sqrt{r_{out}^2w_{x,y}^2-x^2}}2\sqrt{r_{out}^2w_z^2-\left(x^2+y^2\right)w_z^2/w_{x,y}^2}\,\rho(x,y)dydx\\&-K\int_{-r_{in}w_{x,y}}^{r_{in}w_{x,y}}\int_{-\sqrt{r_{in}^2w_{x,y}^2-x^2}}^{\sqrt{r_{in}^2w_{x,y}^2-x^2}}2\sqrt{r_{in}^2w_z^2-\left(x^2+y^2\right)w_z^2/w_{x,y}^2}\,\rho(x,y)dydx\end{aligned} \qquad [4.5].$$

For a freely diffusing sample, the density distribution is unity throughout space and the probability is:

$$P(N) = \frac{4}{3} K \pi w_{x,y}^2 w_z \left(r_{out}^3 - r_{in}^3 \right) \quad [4.6].$$

The probability distribution of burst heights was plotted in Figure 4.4A for three representative single-molecule fluorescence data traces, and fitted to the above probability with nonlinear least squares (NLLS) fittings, assuming a uniform density distribution of molecules in space. Each data trace produced the spatial distribution of over 2,000 molecules that crossed the probe volume within 6.5 seconds. All three fits had R^2 values of over 0.96, indicative of excellent consistency between the model and experimental data. We have analyzed hundreds of data files and the fit has been consistently good, with small χ^2 values for the fits. The root mean squared residues between the experimental probabilities and the theoretical model were displayed in Figure 4.4B for 100 data traces. The small fitting residues compared to the experimental probabilities clearly demonstrated the goodness of fitting.

That the single molecules closely follow the photon statistics is a significant finding. First we concluded that the heights of the photon bursts indeed reflected the locations of the diffusing molecules. These locations corresponded to the positions where the molecules experienced the strongest excitation during their random walk through the probe volume. More precisely, molecules that emitted a certain number of photons (N) were located inside an ellipsoidal shell that is a few nanometers in thickness. This localization was at super-resolution, beyond the diffraction limit. Second, the excellent agreement of the burst statistics with the theoretical model showed that there were no large structural features inside the porous particles that would hinder the random distribution of molecules in space. In other words, any structural blocks in the particle,

for example, the solid silica phase separating the nanopores, should be substantially smaller than the size of the probe volume that is ~230 *nm* in the lateral dimension.

4.3.2. Single molecule counting in nanopores

To establish the methodology of single molecule counting in nanopores, the concentration dependence and the signal-to-noise ratio of counting were evaluated. Photon burst data for two representative concentrations, 5 *pM* and 30 *pM*, were shown in Figure 4.5A. An interesting feature of the single molecule burst data is that the intensity or the height of the photon bursts is independent of the fluorophore concentration, as demonstrated by the average burst heights for all concentrations in Figure 4.5B. The molecular concentration was manifested in the number of bursts observed in the data trace. In the two representative concentrations shown in Figure 4.5B, the 30 *pM* data trace recorded a much higher frequency of photon bursts than the 5 *pM* one, while the burst heights were quite similar. Indeed, the burst counts exhibits linear dependence on the fluorophore concentration (Figure 4.5B), forming the basis for quantification in nanopores using single molecule counting.

For single molecule counting to be used as a general methodology for probing molecular transport in the nanopores, an understanding of the counting statistics and noise is necessary. To perform this assessment, the number of molecules in different time intervals, from 10 *ms* to 6.5 *s*, for ten data traces, has been counted. As expected, the average number of molecules in the ten data traces increases linearly with the counting time, with a correlation coefficient of 1.00 (Figure 4.6A). The noise in single molecule counting is modeled by calculating the standard deviations of the ten data traces. The average molecule counts exhibit a quadratic dependence on the noise (Figure 4.6B). To

understand the noise distribution, it is useful to consider the particle nature of the individual molecules. The single molecule counting experiments involve enumerating molecules that diffuse through the ellipsoidal probe volume. The phenomenon of discrete particles crossing a boundary in space dictates that single molecule counting should follow Poisson statistics. The noise in counting then is expected to exhibit shot noise distribution and scales with the square root of the molecule counts. The signal-to-noise ratio (*SNR*) of the measurement or the ratio of the number of molecules to the noise would also scale with the square root of the counts. As illustrated in Figure 4.6C, both the noise and the *SNR* show this linear dependence in the time window investigated. However, the noise is not exactly predicted by the signal level, indicated by the non-unity slope of the plot. The discrepancy in the slope was attributed to the procedure of counting molecules. A thresholding procedure was applied in searching single molecules in the fluorescence data trace to ensure that the photon bursts enumerated were at least three standard deviations above the background and thus ensure that they were true photon bursts (Figure 4.1). As a consequence, a fraction of molecules that emitted photons below the threshold were ignored by the counting program. This fraction was determined by the intensity distribution in Figure 4.4 and was constant across all time intervals. The number of molecules counted in the experiment S_m is a fraction of the total number of molecules S: $S_m = fS$, where f is the fraction. $1 - f$ is the portion of molecules missed in counting by intensity thresholding. The measured single molecule counts, however, exhibited a noise level consistent with the real number of molecules $N = \sqrt{S} = \sqrt{S_m} / \sqrt{f}$ and thus scaled with the square root of the measured counts, but with a slope that is off by a factor of $\sqrt{f}$. The fraction f was determined by fitting the noise to shot noise distribution. For the

fluorescence traces in Figure 4.6, both the noise and the *SNR* show excellent Poisson dependence on the single molecule counts when f is 0.60; the linear fit of both lines resulted in slopes of unity. The measured numbers of molecules were corrected to yield the actual number of molecules in the probe volume and plotted in Figure 4.6D. This correction protocol proved to be very useful in accurate single molecule counting. With the protocol of f evaluation, the exact number of molecules was measured, even when many molecules were hidden in the background noise. Consequently, the exactly molecular concentration was determined without the need of concentration calibration.

The dependence of single molecule counting on the excitation laser power was also investigated. When the excitation intensity is elevated, it is expected that the burst heights will increase accordingly, as a molecule diffusing through the probe volume will experience higher photon flux density, undergo more frequent excitation, and emit higher number of photons. The number of molecules observed will not vary with the laser power. Single molecule counting was performed at seven laser powers from 0.1 mW to 0.7 mW. The fluorescence burst data for the lowest and highest power were shown in Figure 4.7A. According to the figure, the higher excitation intensity clearly induces much stronger photon bursts from individual molecules, with the burst frequency unchanged. The average burst heights for the 2,000 observed molecules in a time trace display the expected dependence on the excitation laser power (Figure 4.7B). Three sets of replicates showed good consistency in the average burst heights. Interestingly, the maximum photon counts of the corresponding individual data traces do not show the expected excitation power dependence, as illustrated in Figure 4.7B. The three calibration graphs constructed with single trace maxima exhibit a general trend of increasing photon counts

at higher laser power, but a linear dependence for single photon excitation is not evident. A close examination of the molecule statistics showed that a single data trace had not generated enough individual molecules to ensure that at least one of them had crossed the center of the probe volume in their random walks through the probe volume. Indeed, with the volume of the center ellipsoid defined as ~ 0.0001 *fL*, the probability of finding a molecule at the center of the laser beam is 0.0002. With 2,000 molecules observed in 6.5 seconds, a burst data trace does not definitively find a molecule at the focal point. When a global maximum in photon bursts was found from 20 time series, corresponding to 40,000 molecules observed, at each laser power, the global maximum photon counts show good linear dependence on the excitation intensity (Figure 4.7C).

4.3.3. Localization of molecules in ellipsoidal shells of nanometer thickness

In single molecule imaging experiments, localization of the molecule is achieved in the lateral dimensions by fitting the image with a two-dimensional Gaussian function [84, 155] [81] and in the axial dimension by computation of the evanescent wave intensity [81] or by analyzing the *PSF* generated with a cylindrical lens inserted [84]. Super-resolution localization is usually achieved with these approaches.

In our experiments, intensity traces were collected over time from diffusing molecules in the confocal geometry, without immobilization of the molecules or image acquisition. To evaluate the capability in localizing molecules by this confocal approach, it was instructive to analyze the thickness of the ellipsoidal shells in which the individual molecules were distributed. The distances of the molecules from the center of the probe volume in both the lateral and axial dimensions were plotted as a function of the observed burst height in Figure 4.8. Molecules emitting 9 to 120 (maximum) photons at the peak

were located from the center of the probe volume to ~250 *nm* in the lateral and ~1.1 μm in the axial dimensions. With 110 discrete intensity levels, or 110 ellipsoidal shells, in between, the average shell thickness was ~2.4 *nm* and ~9 *nm*, respectively. If the intensity level is thresholded above 100 photons per molecule, to maintain a signal-to-noise ratio of at least ten, the average spatial resolutions are ~3.5 *nm* (20 shells spanning 70 *nm*) and ~ 17 *nm* (20 shells spanning 330 *nm*) in the lateral and axial dimensions. In other words, the confocal burst intensities enable the super-resolution localization of the molecules into thin ellipsoidal shells. The benefits of not acquiring an image of the molecule are the capability of observing microsecond kinetics at super-resolution. The time resolution of the kinetic measurements is dictated by the photophysics of the single molecule fluorescence. The fluorophore used in this study, Rhodamine 6G, has a lifetime of ~4 *ns*, and will emit ~250 photons in a microsecond at maximum excitation. With the allowance in collection and detection efficiency, the time resolution is in microsecond regime at adequate signal-to-noise ratios. If fluorescent molecules with picosecond lifetimes are selected as the probe, the time resolution can be improved to sub-microseconds in kinetic studies. To be able to observe fast kinetics with super-resolution localization is a valuable method in probing molecular systems in the nanopores.

4.4. Conclusions

In this work, we have established single molecule counting as an analytical method for probing molecular transport in nanopores. It is an enabling technology for studying nanoporous materials, with resolution to observe microsecond kinetics and localizing molecules into super-resolution ellipsoidal shells. Single molecule counting shares the tremendous merits of single photon counting in optical detection in that it is

the most sensitive method for measuring molecular concentration and that the variance in the measurements is determined by fundamental shot noise. The time, height, width and shape of the bursts of single molecules carry information on molecular distribution, diffusion, and adsorption and enable the determination of partition coefficients and adsorption energy. Counting molecules location-by-location inside a particle and particle-by-particle within a sample provide a powerful approach to assess the heterogeneity of the micro- and nanoenvironments inside the network of nanopores.

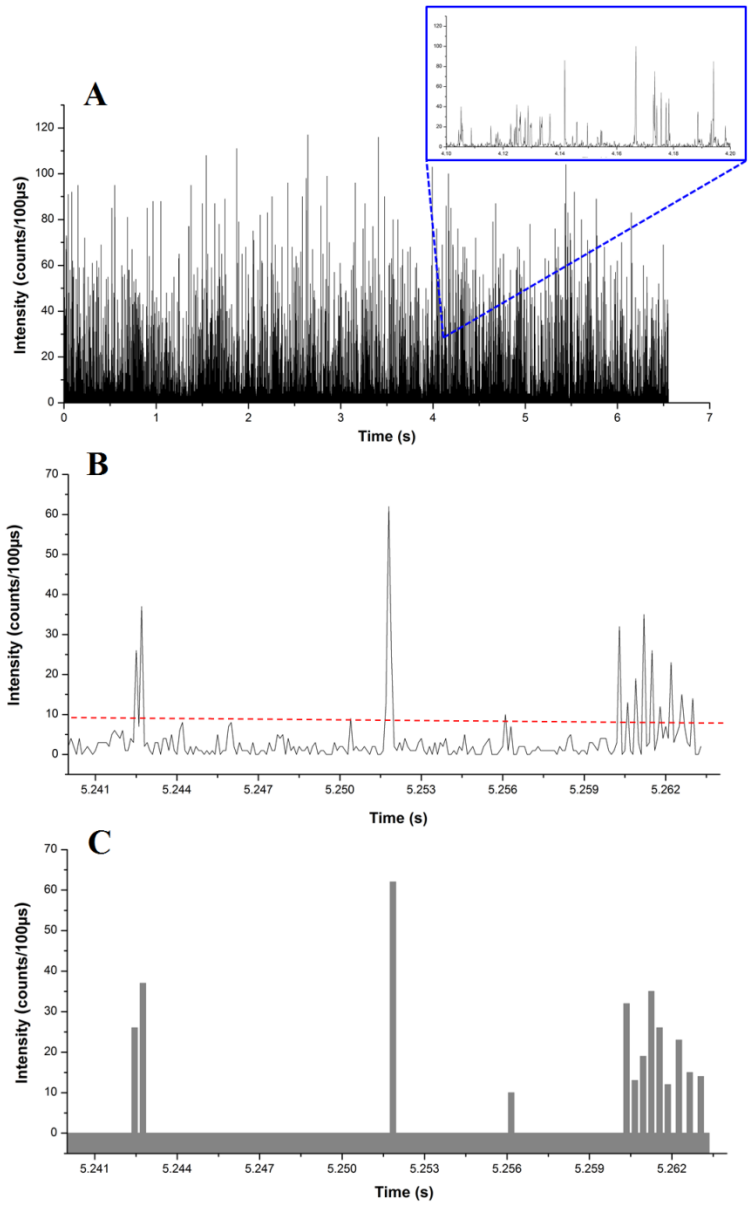

Figure 4. 1 Single molecule fluorescent data trace and the protocol of single molecule counting

---

Note: (A) Single molecule fluorescent time trace collected inside a nanoporous silica particle; (B) Demonstration of the burst searching program to locate photon bursts in data trace. The red dash line represents the threshold limit for burst selection. Bursts above this limit are defined as photon bursts of target molecule, while bursts below this limit are treated as background signal; (C) Molecule counting signal with each molecule defined by peak time and height.

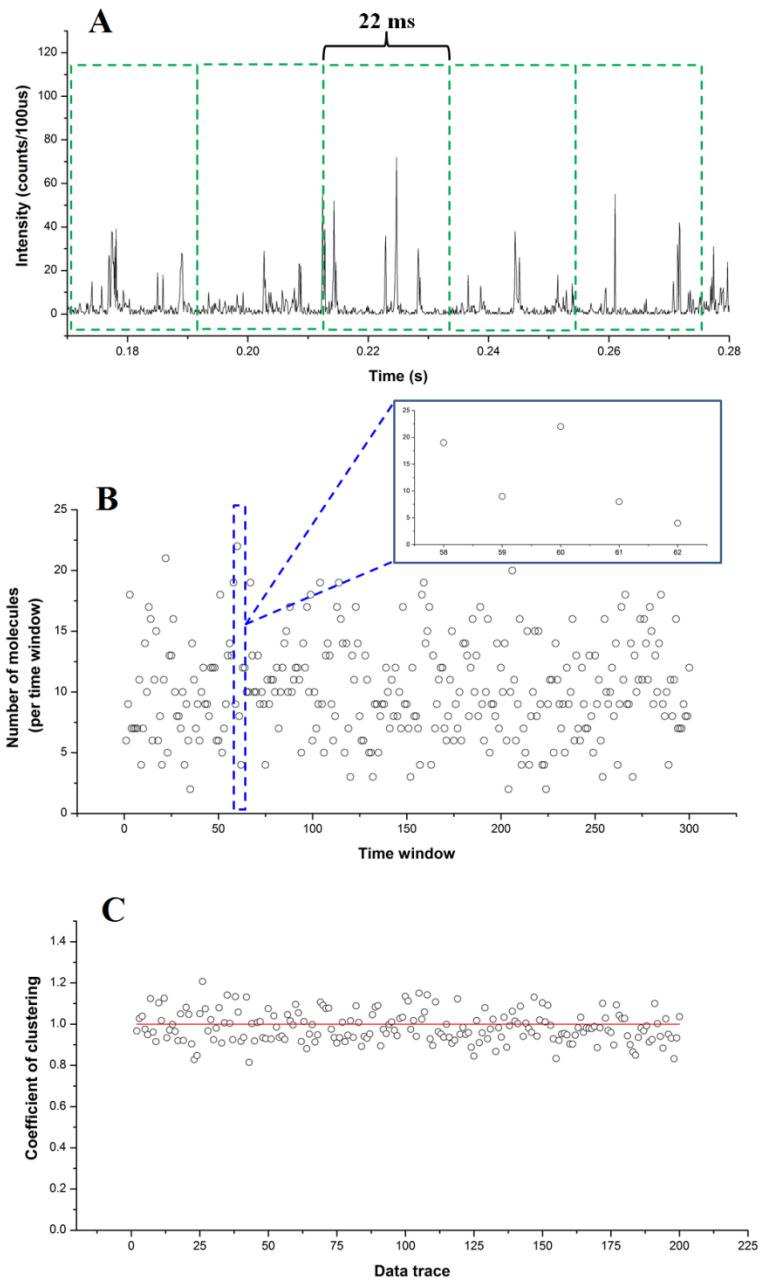

Figure 4. 2 Test of the randomness of single molecules' arrivals in the probe volume

---

Note: (A) Separating the fluorescent data trace into a series of time windows of 22 *ms*; (B) Molecular counts of 300 representative time windows in a time series. Inset: the numbers of molecules in 58th to 62nd time windows; (C) The coefficients of clustering (CoC) of 200 data traces, with closeness to unity. Each coefficient was calculated from 300 time windows in a data trace.

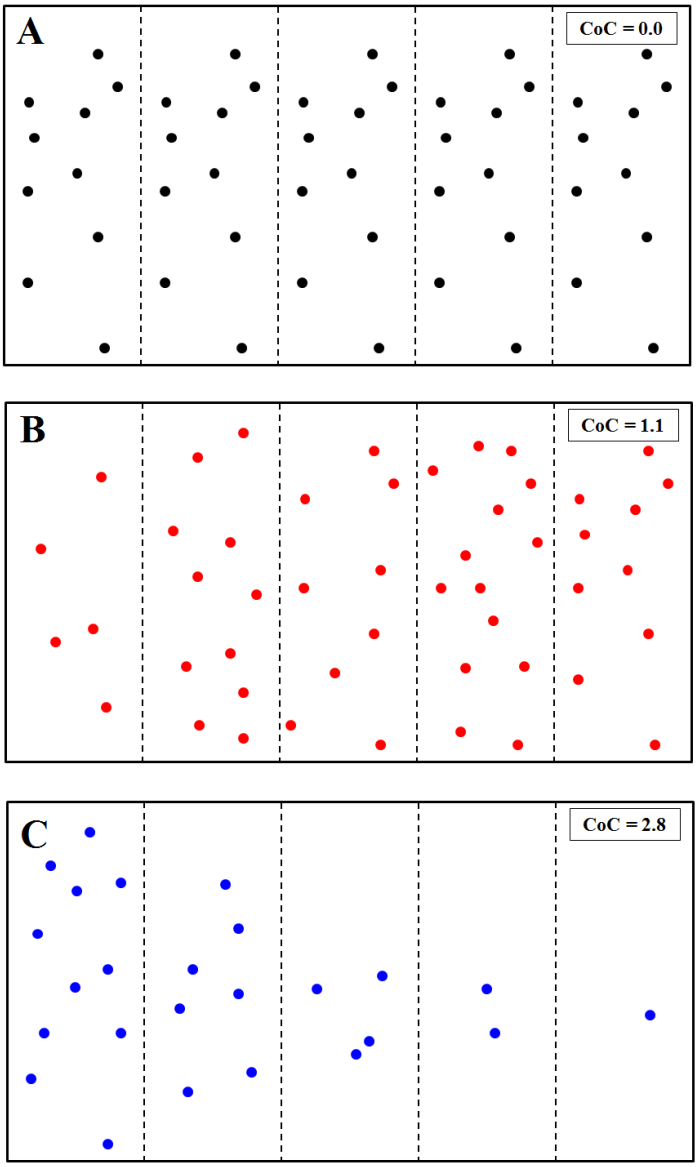

Figure 4. 3 Simulations of molecular distribution with various coefficients of clustering

---

Note: (A) Uniform distribution of molecules with exactly ten molecules in each time window; (B) Random temporal distribution of molecules with an average of ten molecules in each time window; (C) Molecular events with an exponential decay.

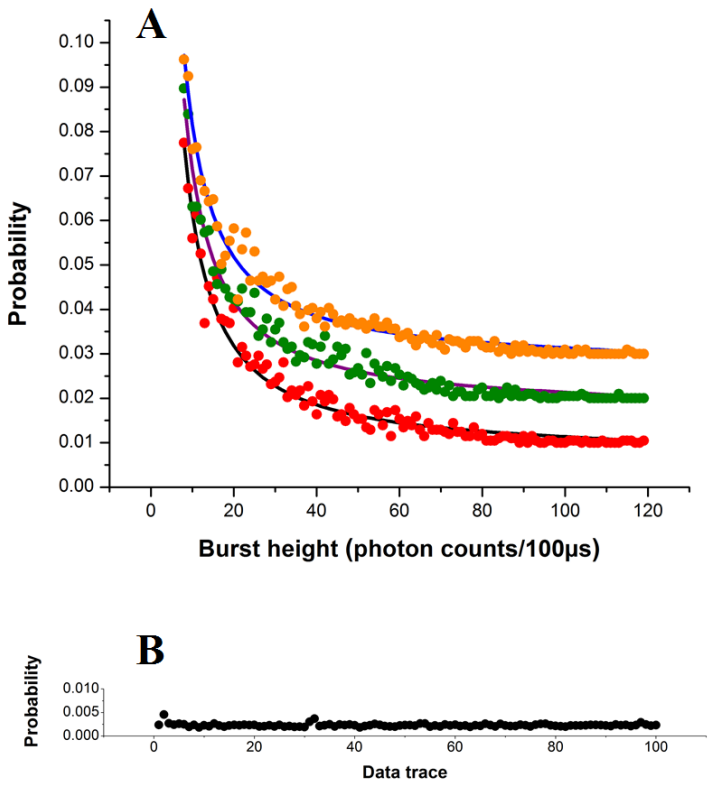

Figure 4. 4 The probability distribution of photon burst heights

---

Note: (A) Probability distributions for three representative single molecule fluorescent data traces and the corresponding NLLS fittings to the derived probability model ([4.6]); (B) The plot of root mean squared residues between the experimental probabilities and the theoretical model for 100 data traces.

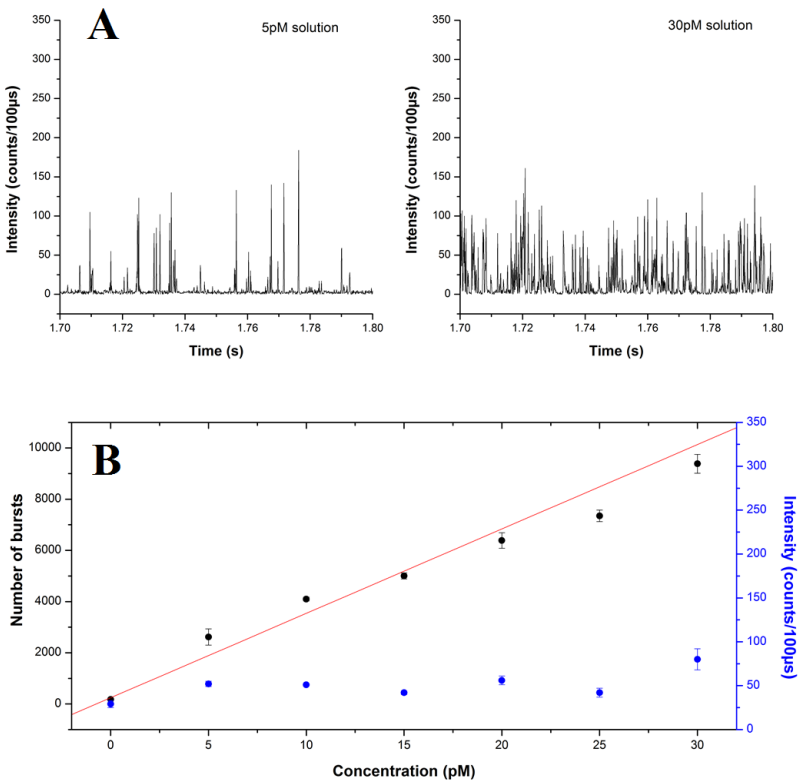

Figure 4. 5 Concentration dependence of single molecule counting

---

Note: (A) Photon burst data for 5 *pM* and 30 *pM* solution; (B) Black panel: Dependence of burst frequency on concentration. Blue panel: Independence of average intensity (burst height) on concentration.

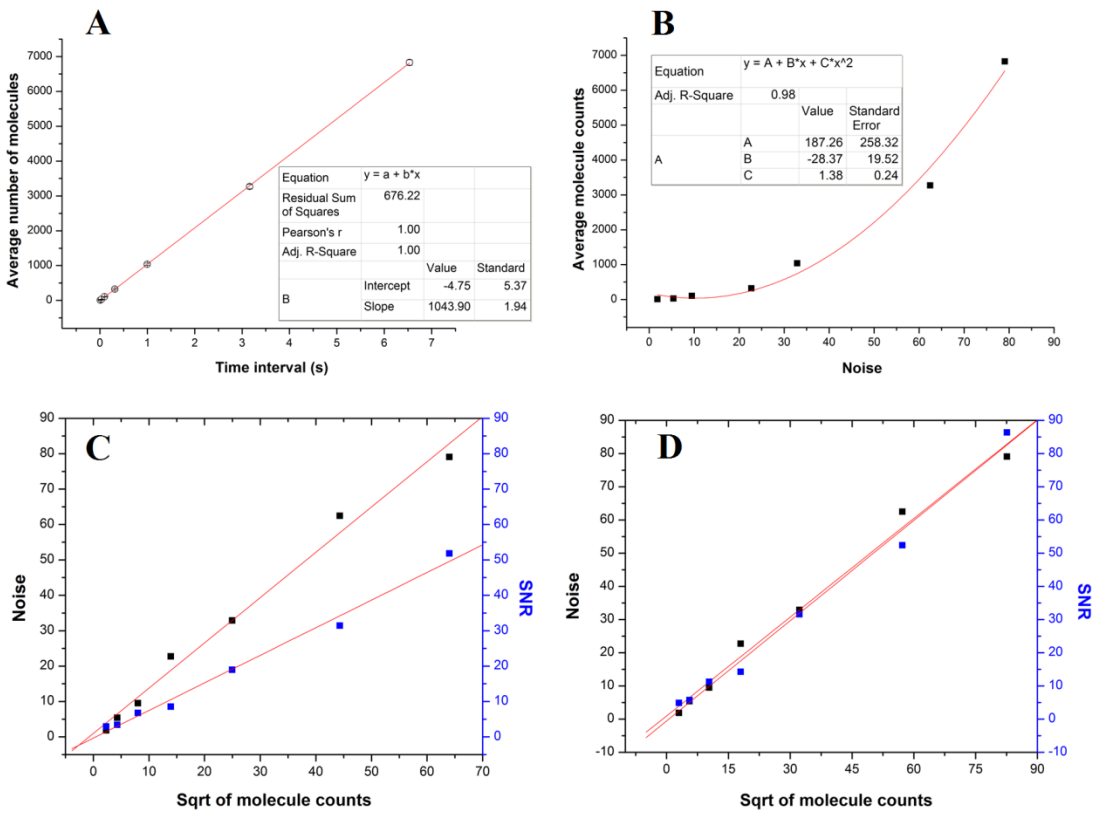

Figure 4. 6 Assessments of counting statistics and noise distribution

---

Note: (A) Linear dependence of average number of molecules on counting time (*s*); (B) Quadratic dependence of average molecule counts on the level of noise; (C) and (D): Linear dependence of noise and *SNR* on square root of molecule counts. (C): The discrepancy in the slopes due to the thresholding procedure for burst searching; (D): The unity of slopes after applying correction protocol (*f* evaluation) and it indicates the accurate measurement of the number of molecules in the probe volume.

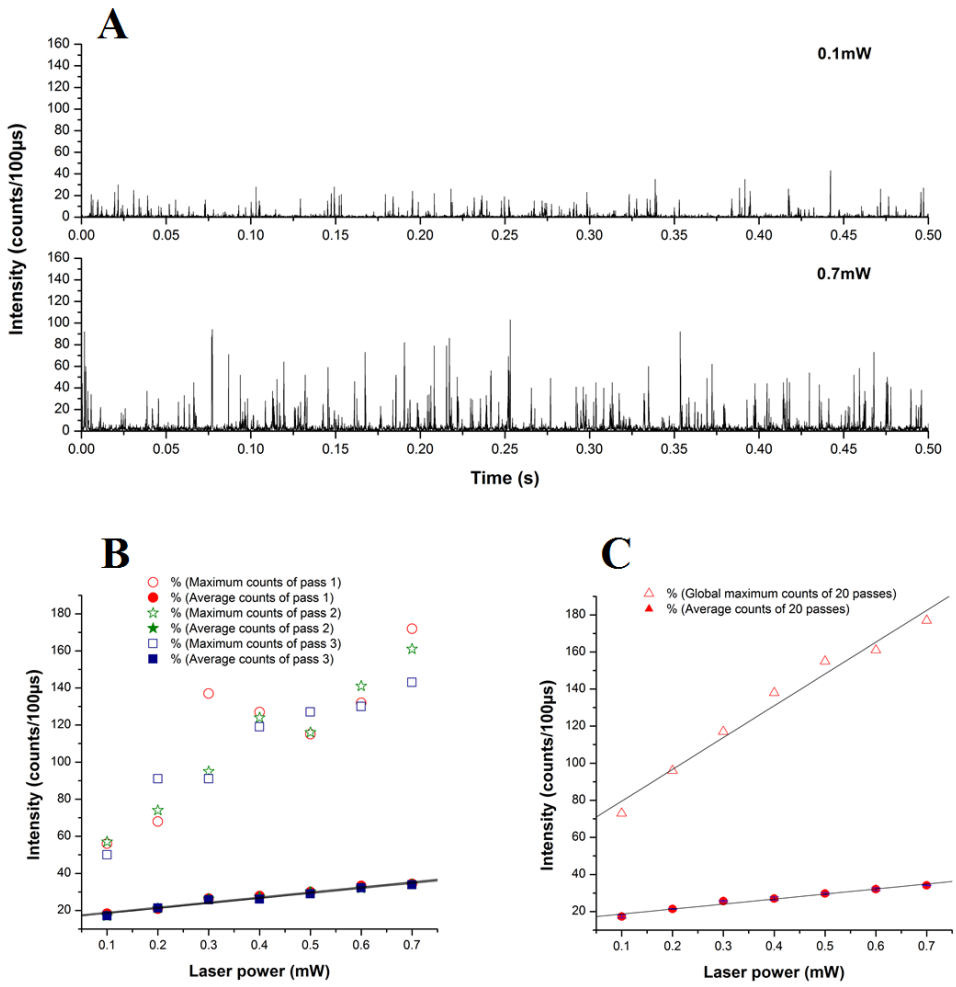

Figure 4. 7 Excitation laser power dependence of single molecule counting

---

Note: (A) Photon burst data at lowest (0.1 mW) and highest (0.7 mW) laser power; (B) Dependence of average and maximum intensities (photon counts/ 100 μs) on excitation laser power (mW) for three representative data traces (passes); (C) Linear dependence of global average and maximum intensities (photon counts/ 100 μs) on excitation laser power (mW) for 20 data traces in time series.

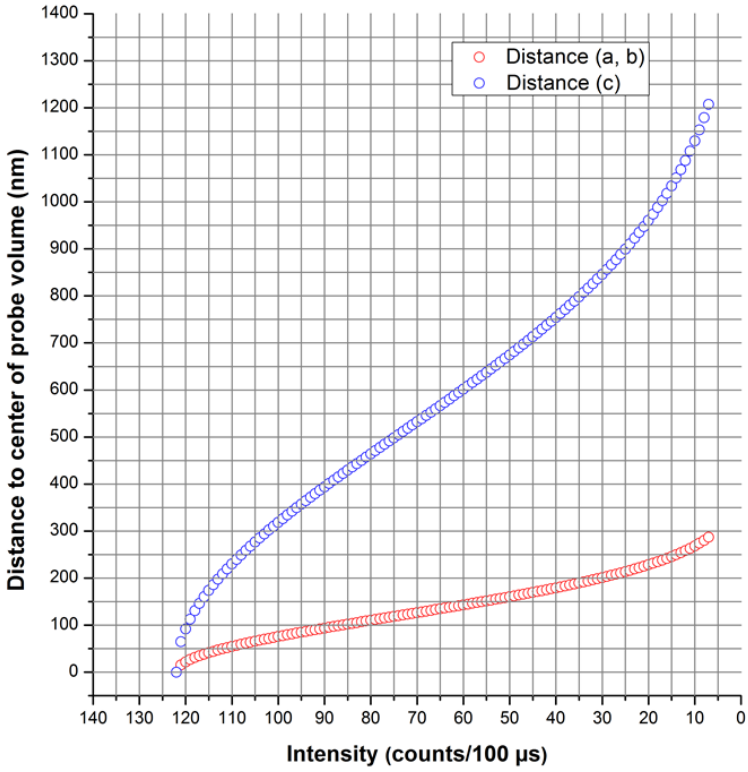

Figure 4. 8 Super-resolution localization of single molecules into ellipsoidal shells with average thickness of a few nanometers

CHAPTER 5

PROBING HETEROGENEITY IN NANOPOROUS SILICA BY SINGLE MOLECULAR DIFFUSION

5.1. Introduction

The study of environmental heterogeneity is of great interest especially in the field of biological and biophysical science since the knowledge of heterogeneities in local environments of biological system or complex, such as the intracellular heterogeneity and the conformational heterogeneity of biological macromolecules, would help the understanding of the nature of biological processes and functions in the cells or other biological system [156-158]. For instance, the alcoholic liver disease, associated with the decrease in erythrocyte deformability and the abnormalities of membrane lipid compositions was able to be diagnosed and monitored by measuring the changes in erythrocyte membrane viscosity [159]. Zick and Ulberth have observed a continuous increase in the viscosity of red blood cells (RBC) and platelet membranes in diabetic patients. By probing this intracellular heterogeneity in viscosity, they revealed the fact that the change in viscosity significantly contributed to the inhibition of the activation of the hepatic insulin receptor kinase (IRK) [160, 161].

In the past decades, the studies of microenvironmental heterogeneity have been mainly focused on two areas: (1) probing the conformational heterogeneity and structural dynamics of biomolecules, such as folding and unfolding processes of protein and (2) measuring the heterogeneity in intracellular physicochemical properties, such as the distribution of micro/nanoviscosity in cells and biological membranes.

Nuclear magnetic resonance (NMR) has emerged to be one of the most important approaches for probing the conformational heterogeneity of biomolecules [162-167]. The nuclear magnetic resonance spectroscopy has demonstrated its capability in detecting unfolded and partially folded protein conformations as well as the dynamics of protein motions [166, 168-171]. The Oas and coworkers probed slow conformational dynamics of Bacillus subtilis ribonuclease P protein at millisecond time scale by conducting ^{15}N NMR relaxation experiments in the ensemble. They demonstrated the existence of the backbone conformational heterogeneity in the P proteins [164]. The characterization of unfolded and partially folded proteins is usually achieved through the dispersion of the ^{13}C and ^{15}N nuclei due to their sensitivities to the local amino acid sequence [172-174]. A study that really highlighted the power of NMR relaxation dispersion spectroscopy as a tool for approaching the conformational heterogeneity in proteins was reported by Kay group in 2010. They successfully conquered the limitations of low occupancies of proteins and achieved direct measurements of folding dynamics and conformation heterogeneity in sparsely populated small protein at atomic resolution by using chemical shifts and bond-vector orientation constraints which were directly obtained from the NMR detection [175]. However, with millisecond time resolution, NMR relaxation dispersion spectroscopy has its limitation to detect the conformational heterogeneity associated with fast dynamics such as the interconversion processes between various conformations of protein. The information of fast (i.e. nanosecond, microsecond) conformational dynamics is then unable to be resolved through this approach. Time-resolved fluorescence spectroscopy, with nanosecond time resolution, has gain its popularity in probing the conformational heterogeneity associated with fast interconversion process between different

conformational states of proteins [176-178]. Fluorescence resonance energy transfer (FRET) has been extensively employed to approach the conformational heterogeneity and microsecond kinetics in protein molecules [179-183]. The time dependent fluorescence intensity decay is usually monitored at the donor site of target protein and the corresponding fluorescence lifetime is obtained from fitting. Since the decay rate is determined by the distance between the donor and acceptor, the resultant fluorescence lifetime thus serves as an indicator of the changes in the donor-acceptor distance that associates with structural changes of protein. The distribution of fluorescence lifetimes then indicates the conformational heterogeneity of protein molecules during the short-time folding and unfolding processes.

Beside the conformational heterogeneity, the distribution of physicochemical properties of biological microenvironments is the other area of interest. For example, the microviscosity distribution in live cells and biological membranes has been tremendously investigated [184-190]. In-depth understanding of the distribution of microviscosity is essential since the heterogeneity in microenvironmental viscosity plays an important role in determining the biochemical processes and intracellular events undergoing in live cells or biological structures [188, 191].

Viscosity, a direct indicator to the local environment, is usually approached by measuring molecular diffusion since the diffusing molecule can be treated as the reporter of the viscosity of local environments. By tracking the diffusion of fluorescence dye molecule in cells, the heterogeneity in the intracellular viscosity has been investigated with fluorescence microscopy imaging [192-196]. The intracellular molecular diffusion evidences the transports and motions of fluorescence probe molecules in the interstitial

substance and hence, provides the information of changes in microviscosity in the cell. The fluorescence recovery after photobleaching is one of the early-reported techniques used for probing molecular diffusion and microviscosity distribution in cell [185, 197]. In an early work published by Jacobson group, the diffusion of microinjected macromolecules was measured in the cytoplasm of human fibrolasts by the fluorescence recovery after photobleaching (FRAP). By monitoring the molecular diffusion at different locations of cytoplasm, they demonstrated the heterogeneity in the viscosities of various elements of cytoplasmic structures evidenced by the changes in the measured diffusion coefficient of the injected macromolecules. With the detailed understanding of the distribution of intracellular microviscosities, they revealed the fact that microenvironments of some filamentous structures in cytoplasm such as microtubules and microfilaments possessed greater viscosity that could restrict the molecular diffusion [197].

In the past years, a novel biosensor—molecular rotor has been invented and widely employed to probe the heterogeneity in microenvironments [158, 188, 198-200]. The molecular rotor is a fluorescent molecule that forms twisted intramolecular charge transfer (TICT) state upon photoexcitation. The emitted fluorescence intensity is viscosity-sensitive since the formation of TICT state depends on the microenvironmental viscosity of where the rotor molecule diffuses in. the fluorescence lifetime of the molecular rotor is thus a function of the viscosity of its microenvironment. The distribution of microviscosities of biological complex has been mapped by applying the fluorescence lifetime imaging (FLIM) of the molecular rotors [190, 201]. The fluorescence lifetime distribution was obtained by fitting the fluorescence decay in each pixel of the image to exponential decay model and the information of environmental heterogeneity

existed in biological structures was then acquired by correlating the fluorescence quantum yield, fluorescence lifetime of the molecular rotor and the microviscosity through Fȍrster-Hoffmann equation [202]. However, as a limitation of this methodology, the calibration curve is needed for the determination of viscosity. A ratiometric fluorescent viscosity sensor which possesses a dual-dye configuration has then been developed. One of the fluorescent dyes serves as the internal intensity reference whose intensity is independent on the environmental viscosity. The second dye molecule which is viscosity-sensitive, serves as the reporter of local viscosity. This ratiometric sensor provides access to the accurate and self-calibrating measurement of microviscosity [187, 203, 204].

The environmental heterogeneity in biological structures has been extensively investigated because of its important role in the functions of protein, cells and membranes. The research reported so far, however, relies on ensemble measurements which are established upon an assumption that the heterogeneity in microenvironments does exist and moreover, the distribution of the properties of the structure is constructed by fitting the experimental data to a pre-determined distribution. For instance, Chattopadhyay and coworkers have conducted a study on the depth-dependent heterogeneity in membrane at nanometer dimension by approaching fluorescence lifetime distribution along the hydrocarbon chains of the fatty acid-formed bilayer membrane. They monitored the fluorescence intensity decay at four different positions of the hydrocarbon chains and solved the fluorescence lifetime for each position through NLLS fitting to the model of continuous distribution of lifetime. Since the decay kinetics of the fluorescent probe molecule involved in the nanoenvironments of membrane generally shows a significant level of heterogeneity, the fluorescence lifetime distribution would

indicate and characterize the heterogeneity in nanoenvironments of the membrane. In order to obtain the lifetime distribution from the limited number of fluorescence lifetime (only 4 data points available), the maximum entropy method—a method to achieve the optimal distribution of the quantities by taking multiple iterations to minimize χ^2 value and maximize entropy of system, was introduced for constructing the distribution of the fluorescence lifetimes [189]. This makes the measurements of nano/microenvironmental heterogeneity indirect. Herein, it is of great interest to develop a methodology that allows the direct measurements of the nano/microenvironmental heterogeneity in a system. In this chapter, a novel approach of using confocal fluorescence single molecule spectroscopy to investigate the environmental heterogeneity inside the nanopores of organically-modified silica particles is presented. The distributions in the nanoenvironmental polarities and viscosities are directly assessed by single molecule ratiometric spectroscopy of a solvatochromic probe and fluorescence correlation spectroscopy. Our single molecule approach directly measures the architectural and solvation heterogeneities without any a *priori* hypothesis about the distribution which is always required for traditionally ensemble measurements. Since the nanoenvironmental properties determine how substrate molecules interact with the nanostructures, this approach thus provides an excellent source of information for applications of nanostructures and more significantly, serves as a tool to probe the heterogeneity existed in biological membranes and live cells which would enhances the understandings of biological functions and processes.

5.2. Experimental

5.2.1. Chemicals and materials

Rhodamine 6G was purchased from Aldrich (Milwaukee, WI). Nile Red was obtained from Acros Organics (New Jersey, USA). The chemical structures were listed in Figure 3.1. HPLC grade acetonitrile and microscope coverslips (12-545-G, size 50×35 *mm*, thickness 0.13-0.17 *mm*) were purchased from Fisher Scientific (Fair Lawn, NJ). Immersion oil (refractive index 1.515) was obtained from Cargille Laboratories Inc. (Cedar Grove, NJ). The nanoporous silica particles were purchased from Akzo Nobel – EKA Chemicals (Bohus, Sweden). The particles were surface derivatized with C_{18} monolayer and endcapped to remove residual silanol groups on the surface. The pore wall and the exterior surface are all covered by a layer of C_{18} hydrocarbon chains. They had a nominal diameter of 10 μm, an average pore size of 100 Å, a carbon loading of 17.5% and a surface area of 400 m^2/g. The nanopore surfaces were covered with a C_{18} layer at a density of 3.00 $\mu mol/m^2$. Acetonitrile was sued as the solvent throughout the experiments.

5.2.2. Instrumentation and measurements

5.2.2.1. Sample preparation

Nanoporous silica particles were mixed with solutions (Rhodamine 6G or Nile Red in 100% acetonitrile). After thoroughly mixing, 15 μL of the prepared suspension was sandwiched between two microscope coverslips and sealed using optical adhesive to prevent the movements of particles and solvent evaporation during the experiment. Fluorescence impurities inside of the C_{18}-derivatized silica particles were minimized following the self-developed "standard" protocol stated in Chapter 3. Few photon bursts

were observed for the blank C_{18}-derivatized silica particles. The concentrations of fluorescent probes used throughout the experiments were kept at 50 *pM*, a concentration low enough to assure single molecule observation based on Poisson distribution of molecules in the confocal probe volume.

5.2.2.2. Instrumentation and measurements

The setup of the confocal microscope used for single molecule spectroscopy has been described in the previous chapter and more details can be located in other published articles [112, 118]. In brief, the 514.5 *nm* laser beam provided by an air-cooled argon ion laser (35-LAP-431-220, Melles Griot) was expanded by a beam expander to slightly overfill the back of an oil immersion objective with numerical aperture (N.A.) of 1.45 and 100 times of magnification. The expanded Gaussian beam was introduced into the back port of the microscope and reflected by a dichroic mirror (Z514RDC, Chroma). A microscope objective (100×, N.A. 1.45) focused the beam to a diffraction-limited spot into the sample which was placed on a two-dimensional piezoflexure stage (Physik Instrumente, Germany). The three-dimensional movement of the focal point inside the sample was achieved by a piezoelectric microscope objective stepper along the axial direction and the piezoflexure stage along lateral directions, both with sub-nanometer resolution. The emitted fluorescence from Nile Red or Rhodamine 6G was collected by the same objective, passed through the dichroic mirror and a long-pass filter at 530 *nm* (LP 530, Chroma), and then focused onto a 50-μm confocal pinhole in the image plane to remove the out-of-focus light. The confocal volume has a dimension of ~250 *nm* in the lateral directions and 1 μm in the axial direction [112, 205]. The confocality is essential in the experiments to ensure that the probe volume is completely inside the silica particles to

probe molecular motions in the network of pores, without the signal being overwhelmed by the solvent [112]. The fluorescence was collimated with a lens and then split into two channels by a dichroic beam splitter (Q625LP, Chroma) in the Nile Red experiments. The reflected fluorescence passed through a band-pass filter HQ600/100 nm (centered at 600 nm with a bandpass of 100 nm) and was focused onto the active area of an avalanche photodiode (SPCM-AQ, PerkinElmer Optoelectronics). The transmitted fluorescence passed through a band-pass filter HQ650/75 nm (centered at 650 nm with a bandpass of 75 nm) and was focused onto the active area of a second avalanche photodiode [118]. Some optical components of the instrument were replaced for the collection of the fluorescence from Rhodamine 6G in order to maximize the signal collection efficiency according to its emission spectrum [112]. Time-dependent photoelectron pulses for each detector were counted by a multichannel scaler (MCS) running on a personal computer.

The fluorescence autocorrelation functions were evaluated with programs written in MatLab (Mathworks Inc., Natick, MA). The autocorrelation functions were fitted with nonlinear least squares method (NLLS) in Origin (OriginLab, Northhampton, MA) using the Marquardt algorithm.

5.3. Results and Discussions

With single molecule spectroscopy and confocal microscopy, this study demonstrated a method to investigate environmental heterogeneity at nanometer dimension by probing individual molecules diffusing through the nanoporous structures. The method allowed direct measurements of heterogeneity in the physicochemical parameters of the environments.

In the experimental system, the dye molecules randomly diffused through the network of nanopores in the particle. When a dye molecule diffused across the probe volume of the Gaussian laser beam, it was excited and emitted a burst of photons. The shape and intensity of the photon burst were determined by the trajectory of the molecular diffusion.

At the concentration of 50 *pM*, the probability of finding 0, 1 or 2 molecules in the 0.3 *fL* probe volume are 99%, 0.99% and 0.005%, respectively, according to Poisson distribution. The probability of observing more than one molecules simultaneously is negligible. Each photon burst in the resulting fluorescence data trace thus signifies an individual molecule and contains the information of single molecule diffusion. The molecular diffusion is sensitive to local environment, specifically, to the local viscosity. By using individual diffusing molecules to probe the changes of viscosity inside nanopores, the environmental heterogeneity at nanometer dimension can be explored.

5.3.1. Fluorescence correlation spectroscopy (FCS)

Fluorescence data traces collected inside the C_{18}-derivatized nanoporous silica particles have the unique characteristic of burst structure for single molecules. In the majority of the time, the data trace shows a background signal that is below a few counts. When a fluorescent molecule diffuses across the probe volume, a burst of photons appears. In the data trace shown in Figure 5.1A, approximately 500 molecules were counted within the 1.31second time window. The fluorescence intensity fluctuations in the data trace (Figure 5.1A) were attributed to random Brownian diffusion of the molecules through the nanopores across the probe volume, and could be correlated to reveal the occurrence of molecular diffusion and estimate the average diffusion

coefficient of these 500 molecules by fluorescence correlation spectroscopy (FCS). The fluorescence autocorrelation function was introduced in the previous chapter. Briefly, it is defined as

$$G(\tau) = \frac{\langle \delta F(t) \cdot \delta F(t+\tau) \rangle}{\langle F(t) \rangle^2} \quad [3.1].$$

In the case of molecular translational diffusion across the Gaussian distributed probe volume, the function is then expressed by a three-dimensional diffusion model

$$G(\tau) = \frac{1}{N}\left(1+\frac{4D\tau}{\omega^2}\right)^{-1}\left(1+\frac{4D\tau}{l^2}\right) \quad [3.2]$$

and the definition of each term in the model were stated in previous chapter.

Fluorescence data traces were continuously collected for 50 *pM* Rhodamine 6G in solution in acetonitrile and inside wetted nanopores, at the C_{18}/acetonitrile interfaces, respectively. Average autocorrelation functions of 100 random-chosen data traces for Rhodamine 6G in solution and inside nanopores were both shown in Figure 5.1B. According to the figure, the correlation function for molecules inside the nanopores displays a longer decay indicating slower diffusion when the molecules move through the nanopores compared to free diffusion in the solvent. Nonlinear least squares (NLLS) fittings to the three-dimensional diffusion model described by Equation [3.2] were also illustrated in Figure 5.1B. Using the known beam parameters ω and l, the diffusion coefficient D was determined from the fitting. The slower decay for the autocorrelation function of Rhodamine 6G inside of nanopores resulted in a smaller diffusion coefficient. It demonstrated the partition of Rhodamine 6G molecules into the C_{18} monolayer on the pore wall surface when they diffused at the interface. The 3-D diffusion model

adequately described the decay of the fluorescence correlation function, as indicated by the excellent overlap between the data and the fitting function (Figure 5.1B), and the residues randomly distributed around zero (Figure 5.1C).

Additionally, the ratio of the number of molecules diffusing at C18/acetonitrile interface to the number of molecules diffusing in the acetonitrile occupied in nanopores was estimated, from the partition coefficient of Rhodamine 6G between acetonitrile and C_{18} monolayer, the pore volume and the volume of the C_{18} layer. In details, the average diameter of C_{18}-derivatized pore was about 73 *Å* and 93 *Å* for unmodified pore [116]. With an assumption of perfect tubed geometry of nanopores, the ratio of the volume of C_{18} to the volume occupied by acetonitrile inside pore was estimated as

$$\frac{V_{c18}}{V_{acetonitrile}} = \frac{\pi\times(46.5^2-36.5^2)\times L}{\pi\times 36.5^2\times L} = \frac{830}{1332.2} \qquad [5.1]$$

where *L* represents the total length of nanopores, 46.5 (*Å*) and 36.5 (*Å*) are the average radius of C_{18}-derivatized nanopore and underivatized nanopore, respectively. The average distribution constant *K* for Rhodamine 6G between C_{18} monolayer and acetonitrile was estimated to be about 20 (see Chapter 6 for details). Then the ratio was calculated as

$$Ratio = \frac{\text{\# of molecules at C18/acetonitrile interface}}{\text{\# of molecules in the acetonitrile occupied in nanopores}} = \frac{V_{C18}\times K}{V_{acetonitrile}} = \frac{830\times 20}{133\ 2.2} = 12.5 \quad [5.2].$$

It indicated that 92% Rhodamine 6G molecules diffusing through the probe volume inside the hydrocarbon C_{18} layer. In other words, the calculated diffusion coefficients accurately reflected the diffusion of individual Rhodamine 6G molecules at the C_{18}/acetonitrile interface and specifically characterized the local environments at the

interface. The contribution from the Rhodamine 6G molecules in the acetonitrile inside the nanopores is negligible.

5.3.2. Distribution of diffusion coefficients from single molecule fluorescence correlation spectroscopy (*FCS*)

At each probe location, 200 fluorescence data traces were collected. Each of the data traces was analyzed by calculating the correlation function of the fluorescence intensity fluctuation and the correlation function was fitted to the 3-D diffusion model. The diffusion coefficient of Rhodamine 6G molecules in each data trace was determined. The fitting results of 5 representative data traces collected at a single probe location were shown in Table 5.1, with the diffusion coefficients and their corresponding uncertainties. A very interesting finding was that the diffusion coefficients for each of the 200 data trace were significantly different from each other. If the observation time was long enough for the 500 molecules to sample all environments in the nanopores, the calculated diffusion coefficient would represent an ensemble average of the C_{18}/acetonitrile interface. The 200 diffusion coefficients determined from the 200 data traces collected at a single probe location would then be identical within experimental errors. The fact that the 200 diffusion coefficients were different revealed that (1) the environments inside the nanopores were heterogeneous and that (2) the molecules only sampled a small fraction of these environments in a single data trace. This presented a tremendous opportunity for probing the heterogeneity of the environments in the nanopores.

In order to construct the distributions of diffusion coefficients of individual diffusing Rhodamine 6G molecules to reveal the environmental heterogeneity, 3200 data traces were collected in total at the C_{18}/acetonitrile interface to probe the diffusion of

Rhodamine 6G molecules. Data was collected from 7 randomly selected particles, 10 pixels (probe location) in the first particle at a spacing of 0.*4 μm/pixel* and a pixel in each of the other 6 particles. The distributions for two representative pixels were constructed and displayed in Figure 5.2A and B. Each distribution was composed of 200 diffusion coefficients each evaluated from ~500 diffusing molecules. Although the two pixels shows clearly different distributions, as illustrated as their Gaussian fitting curves in Figure 5.2C, there could be the possibility that they actually derive from the same population of viscosity environments and that 200 data traces are not sufficient to represent the entire population space. In other words, the two probed locations may be characterized by the same broad viscosity distribution, but the molecules have sampled only a fraction of the viscosity environments in both histograms.

To test this possibility, the efficiency of sampling was evaluated by increasing the number of data traces or molecules in the analysis. Figure 5.3 elaborates the testing procedure in detail. For example, in Figure 5.3A, 5 of the 200 data traces collected from single pixel were randomly selected. The mean and standard deviation of the 5 diffusion coefficients were calculated, and the corresponding Gaussian distribution of these 5 coefficients was plotted. It is important to note that the uncertainty in each coefficient from the NLLS fitting (Table 5.1) is about an order of magnitude smaller than the standard deviation of the Gaussian distribution. The width of the Gaussian illustrated in Figure 5.3A thus reflects the heterogeneity in the viscosity environments sampled by the 2500 molecules (in five data traces). Another set of five data traces were then randomly selected and the corresponding Gaussian distribution was plotted and also shown in Figure 5.3A. This process was repeated for 100 times to generate the 100 Gaussian

curves in Figure 5.3A. Clearly, each set of 2500 molecules sampled a different viscosity population inside the nanopores, characterized by their distinctive means and widths of the Gaussian distributions. These results revealed an important picture of the nanoscopic environments inside the pores: within the interconnected network of nanopores permeating the laser probe volume (~0.3 *fL*), the nanopores were not built equivalent. Although all observed single molecules freely diffused through the entire probe volume, their movements were somewhat restrictive in that they traversed specific trajectories in the network and encountered different sets of nanopores. The fact that they exhibited distinctive diffusion coefficients revealed that the individual nanopores possessed completely different nanoviscosity environments.

Based on this understanding, the number of data traces included in the population analysis was increased. With 5, 10, 30, 70, 100 and 190 (an extreme case) data traces, corresponding to ~2500, 5000, 15000, 35000, 50000, and 95000 molecules observed, the distributions evolved from Gaussians with completely different mean diffusion coefficients and widths to converged Gaussian curves with fairly similar means and standard deviations. This was attributed to the larger fraction of the nanoviscosity population sampled by the greater number of diffusing molecules. Indeed, when the number of molecules reached ~50,000, the molecules effectively sampled the entire ensemble of the nanoviscosity environments. At this point, any combination of data traces would provide the same information about the physicochemical environments in the nanopores.

It was imperative to consider the statistical overlap of the data sampling between the distributions in drawing this conclusion. When five data traces were randomly chosen

from 200 (Figure 5.3A), the probability that the same data trace was selected for two specific Gaussian distribution is very small. When 100 data traces were randomly selected from 200 (Figure 5.3E), however, the probability was that any two Gaussian distributions in Figure 5.4E might contain 50% overlap in the data traces between them. In other words, 50% of the nanoenvironments that the molecules sampled in these Gaussians were thus identical, which could naturally make the two distributions more similar than those in Figure 5.3A. Importantly, the fact that 50% difference in the data, or the nanoenvironments sampled, did not result in significant differences between Gaussians suggested that the number of environments sampled in Figure 5.4E approached the entire ensemble.

It was instructive to consider the movements of the molecules inside the nanopores in understanding the environment sampling. The silica particles used in the experiments have a density of 1 *g/mL*, indicating that the pores occupy ~60% of the total volume of the particles, considering the density of silica is 2.4 *g/mL*. Within the 0.3 *fL* of the confocal probe volume in single molecule spectroscopy, the nanopores occupy 0.18 *fL* of volume while solid silica counts for the rest 0.12 *fL*. For an average pore diameter of 10 *nm*, the total length of the pores inside the probe volume was then estimated to be ~2.4 *mm*. In the single molecule fluorescence correlation spectroscopy experiments presented in Figure 5.3, ~500 molecules (photon bursts) were observed in a single data trace. Each photon burst was created by a single molecule's trajectory, starting with the entry of the molecule and ending with its departure from the probe volume in its random walk through the nanopores. Statistically, on average each molecule has traversed the 500 nm diameter of the probe volume in the lateral dimensions during the photon burst. When

100 data traces were analyzed, 50,000 molecules were observed. These molecules traveled 25 mm of distance in the nanopores. In other words, these 50,000 molecules sampled up to ten times of the length of all nanopores in the probe volume. This oversampling allowed the molecules to visit and report on the viscosity of all the nanoenvironments. Statistically, any 50,000 molecules would report on the entire population of the heterogeneous sited, which counted for the fact that distributions in Figure 5.3E were all similar to each other.

Single molecule studies have been established to be an excellent method to discover the existence of heterogeneous populations and recover the distributions by building up the ensemble population with a large number of single molecules. The single molecule events, by nature of the experiments and/or the intrinsic characteristics of the molecular processes being studied, are generally quite rare. As a consequence, some of the population distributions constructed in single molecule studies consist of tens of molecules, or hundreds of molecules. An interesting question is if sufficient number of molecules has been observed to sample all the heterogeneous sites/conformations of the ensemble. In other words, is the population constructed truly the ensemble population, or is it a subset of the ensemble? Is it necessary to observe 1000 molecules? If the system is truly random, with all the sites equally approachable during the observation time, the same distribution is constructed regardless of the number of molecules; a larger number of molecules would only help reveal more details of the distribution. If the system has a structure that somewhat restricts the accessibility of all sites at the experiment time scale, it becomes necessary to observe a large number of molecules in order to access the ensemble population. Figure 5.3 outlines a good protocol to check the ensemble

population. Once the all subpopulations become identical, the ensemble population has been reached, as in Figure 5.3E. Clearly, over 50,000 molecules need to be observed in this experiment to adequately construct the total population of sites in the nanopores. Figure 5.3 demonstrates the power of using single molecule diffusion to decipher the heterogeneity in the nanoenvironmental properties. Single molecule diffusion directly reports the distribution of nanoviscosity. This information is not available from ensemble experiment, which would typically provide information on the average viscosity of all the nanoenvironments.

With the knowledge that 100,000 molecules in the 200 data traces effectively sampled the entire population of nanoviscosities, the two distinctive distributions in Figure 5.2 A and B pointed to different distributions of nanoenvironments within two pixels. With a broader distribution centered at higher diffusion coefficient (shown in Figure 5.2C), pixel 1 in particle 3 shows generally lower viscosities and more heterogeneous nanoenvironments.

Population analysis was performed for all 16 pixels in seven silica particles. Based on the diffusion coefficient distribution summarized in Table 5.2, it is concluded that (1) the nanoviscosities of the local environments in which the Rhodamine 6G molecules diffuse change dramatically. It suggests that the environmental heterogeneity exists for each single pixel; (2) the level of heterogeneity is high and fairly uniform across the pixels, with the relative standard deviations (*RSD*) of distribution close to 26% for all pixels; (3) the environment exhibits heterogeneity between pixels as signified by their substantially different average diffusion coefficients.

5.3.3. Distribution of nanoviscosity

5.3.3.1. Construction of nanoviscosity distributions

With known diffusion coefficients, the viscosities of the local environments were estimated from the Stoke-Einstein equation [206]:

$$D = \frac{k_B T}{6\pi\eta r} \quad [5.3]$$

where k_B is the Boltzmann's constant, T is the absolute temperature, η is the viscosity of the medium, r is the solvated radius of Rhodamine 6G molecule and D is the diffusion coefficient of Rhodamine 6G molecule in the medium [206, 207]. An environmental viscosity was calculated for each diffusion coefficient from each data trace. The nanoviscosity distributions of the two pixels in Figure 5.2 A and B were then constructed and presented in Figure 5.4A and B, correspondingly.

5.3.3.2. Interpretation of nanoenvironmental heterogeneity origins

The heterogeneity in the nanoenvironmental properties arise from the intrinsic structure of the nanopores and of the solid-liquid interface. In the interconnected network of nanopores inside the silica particles, the architecture dictates the existence of heterogeneous sites—architectural heterogeneity. It is expected that the density of the C_{18} chains in the organic layer is higher along the straight nanopores and lower at the curved surfaces at the junctions where the nanopores connect. Wirth and coworkers have shown that the viscosity in the densely packed hydrocarbon core of micelles is an order of magnitude higher than that of the solvent [208]. The surface density of hydrocarbon chains in the nanopores is 3 $\mu mol/m^2$ for these particles. In the straight nanopore regions, the tails of the hydrocarbon chains extend into the nanopore space, and occupy a slightly

smaller area than their “roots". This geometry results in a high density packing of the C_{18} chains creating sites with high nanoviscosities. On the other hand, at the corners of the intersections where nanopores connect, the C_{18} chains extend out of the curved surface. The tails of the hydrocarbon chains occupy a larger surface area than the “roots”, creating sites with sparser packing and correspondingly lower viscosities. The second source of the nanoenvironmental heterogeneity originates from the C_{18}-acetonitrile interface—solvation heterogeneity. Although the highly hydrophobic environment in the C_{18} layer prevents the polar solvent acetonitrile from thoroughly partitioning into the hydrocarbon phase, the solvent molecules can penetrate into the outer region of the C_{18} hydrophobic layer. These solvent molecules result in a reduced viscosity. The inclusion of solvent molecules is at the highest concentration at the outermost carbon and decreases continuously along the carbon chain towards the silica surface. The gradient of solvent molecules creates a gradient in nanoviscosity along the carbon chains, as illustrated in Figure 5.5. When a fluorescent molecule diffuses through the pores, it samples the nanoenvironments and reports the nanoviscosity distribution (Figure 5.4). Since the fluorescent probe Rhodamine 6G is positively charged, it stays at the solvent- C_{18} interface and does not partition deeply into the C_{18} phase. The distribution of nanoviscosity in the Rhodamine 6G experiments thus primarily reveals the heterogeneity in the nanopore architecture, but not the solvation in the C_{18} phase. This is evidenced by the distinctive diffusion coefficients reported by the single molecules when they sample different sampled different subpopulations of the nanopores in Figure 5.3A.

5.3.4. Distribution of nanopolarity from ratiometric single molecule spectroscopy

To assess solvation heterogeneity, a fluorescent probe that could be solvated in all nanoenvironments was required to sample the entire population. A charged probe such as Rhodamine 6G, though an excellent reporter of the distribution in architectural sites, was primarily located at the spatial region right between the solvent and the hydrophobic C_{18} layer, with its hydrophobic moiety buried in C_{18} and its charged side extended into the polar acetonitrile solvent. A neutral fluorophore presented a good choice for probing solvation heterogeneity as it could be positioned at all locations inside the C_{18} layer. As the solvation gradient along the hydrocarbon chain of the C_{18} layer would a gradient in nanopolarity, a polarity-sensitive solvatochromic fluorophore, Nile Red, was employed as the probe molecule in single molecule ratiometric measurements.

As illustrated in Figure 5.6, the fluorescence emission spectrum of Nile Red shows a red shift when environmental polarity is elevated, with a concurrent reduction in fluorescence quantum yield [118]. This bathochromic effect was captured by ratiometric single molecule fluorescence spectroscopy. The fluorescence emission of Nile Red was split into two wavelength regions collected in two separate detection channels. The ratio of fluorescence intensities at the short-wavelength region (centered at 600 *nm*, I_{600}) and the long-wavelength region (centered at 650 *nm*, I_{650}) was shown to decrease with increasing environmental polarity [118] and was defined as the polarity ratio *R*. As only a few tens of photons were detected in each transient photon burst when a molecule diffused through the confocal probe volume, it was impractical to measure the entire emission spectrum of each individual molecule. Instead, the photons were integrated in

the two wavelength regions in ratiometric single molecule spectroscopy to capture the spectral shifts at the highest signal-to-noise ration possible.

In ratiometric single molecule measurements, 50 *pM* Nile Red in 100% acetonitrile permeated into the nanopores in the silica particles whose wall surface was lined with a C18 layer. A total of 1200 fluorescence data traces, evenly distributed in 6 different pixels (200 data traces/pixel), were collected to probe the diffusion of single Nile Red molecules at the C_{18}/acetonitrile interface. The fluorescence correlation analysis has been performed for all the 1200 photon-burst data traces to treat the diffusion of single Nile Red molecules. The distributions of diffusion coefficients were resolved and summarized in Table 5.3.

Results in Table 5.3 demonstrate that (1) the nanoviscosities of the local environments in which Nile Red molecules diffuse are much higher than that of Rhodamine 6G molecules, evidenced by the slower average diffusion coefficients of Nile Red, although the two molecules are of similar size; (2) the relative standard deviations of the distributions for all six pixels are between 50% and 61%, much broader than the 26% for Rhodamine 6G. This phenomenon was attributed to the higher level of heterogeneity of the nanoenvironments that Nile Red molecules probed.

The polarity ratio (R) was characterized as the photon counts collected in the short-wavelength channel (I_{600}) ratioed to the photon counts collected in the long-wavelength channel (I_{650}) for each individual molecule, expressed as

$$R = \frac{I_{600}}{I_{650}} \qquad [5.4].$$

According to this equation, when Nile Red molecule diffuses in a high-polarity

environment in the nanopores, the fluorescence emission spectrum shifts to longer wavelength, associated with a low intensity ratio $R(I_{600}/I_{650})$. When Nile Red molecule diffuses in low-polarity environment, $R(I_{600}/I_{650})$ increases. Polarity calibration was performed using a series of solutions of 1 μM Nile Red in acetonitrile-water mixture ranging from 100% to 50% acetonitrile. A relationship between the intensity ratio $R(I_{600}/I_{650})$ and polarity index was also established [116]. In brief, the polarity index for the binary mixtures was calculated as

$$P'_{mixture} = \Phi_W P'_W + \Phi_{ACN} P'_{ACN} \quad [5.5]$$

where Φ_W and Φ_{ACN} represent the volume fractions of water and acetonitrile in the mixture. P'_W and P'_{ACN} are the polarity indices of water, 10.2, and acetonitrile, 5.8, respectively. Additionally, the $R(I_{600}/I_{650})$ values for Nile Red in 100% octane, acetonitrile-wetted nanoporous silica particles with and without C_{18} layers were also measured to be 4.5, 1.3 and 0.8 respectively, to indicate the low polarity in a hydrocarbon environment, the polarity at the C_{18}/acetonitrile interface and the polarity at the bare silica/acetonitrile interface. The constructed calibration curve [116] clearly illustrates that as the water content and the polarity of the acetonitrile-water mixture increases, the intensity ratio $R(I_{600}/I_{650})$ decreases monotonically. This calibration demonstrated the $R(I_{600}/I_{650})$ as an appropriate index for environmental polarity.

To assess the nanoenvironments, first of all, distributions of diffusion coefficients of Nile Red molecules were constructed for each pixel. A representative distribution for a single pixel shown in Figure 5.7A reveals some essential characteristics: (1) The broad distribution indicates the existence of environmental heterogeneity in which the Nile Red molecule diffuses; (2) Compared to Rhodamine 6G, Nile Red molecule exhibits slower

diffusion at C_{18}/acetonitrile interface since its average diffusion coefficient is ~8.81×10^{-7} cm^2s^{-1} (Table 5.3), slower than the diffusion coefficient of Rhodamine 6G (~1.24×10^{-6} $cm^2\ s^{-1}$, Table 5.2). Considering the similarity in sizes of the Nile Red and Rhodamine 6G molecules, this observation suggested that Nile Red molecules on average diffused in the environments of higher local viscosity. As illustrated in Figure 5.5, at the C_{18}/acetonitrile interface on the nanopores wall, acetonitrile molecules penetrate into the C_{18} layer. The nanopolarity decreases along the direction of penetration since the amount of solvated acetonitrile decreases at deeper penetration depth. Meanwhile, the nanoviscosity increases, resulting in slower molecular diffusion. With the results of single molecule FCS, it was concluded that the Nile Red molecules indeed were distributed deeper into the C_{18} layer than the Rhodamine 6G molecules as evidenced by the slower diffusion. This partitioning of Nile Red molecules along the hydrocarbon chains provided an opportunity to access the depth-dependent heterogeneity at the interface—the solvation heterogeneity.

The distributions of diffusion coefficients of Nile Red molecules and that of the Rhodamine 6G molecules at the C_{18}/acetonitrile interface were then compared. Five hundred data traces for Nile Red and Rhodamine 6G molecules were randomly selected out from the entire acquired data pool. Each data trace was analyzed by calculating the fluorescence autocorrelation function and fitting to the 3-D diffusion model (Eq. [3.2]). The distributions of the resultant diffusion coefficients were constructed and compared in Figure 5.7B. For the purpose of visualization, these two histograms were fitted to Gaussian distributions. With a broader distribution of diffusion coefficients for Nile Red molecule, Figure 5.7B clearly presents a higher level of environmental heterogeneity for

Nile Red molecules diffusing at the C_{18}/acetonitrile interface. The details of the distributions were summarized in Table 5.4. A corresponding schematic diagram illustrating the differences in the molecular behaviors of Nile Red and Rhodamine 6G molecules at C_{18}/acetonitrile interface was also presented in Figure 5.8.

According to Table 5.4 and Figure 5.8, the broader distribution for Nile Red molecule, as expressed as the relative standard deviation of the Gaussian fitting curve, originate from the fact that Nile Red is able to penetrate deeply into the C_{18} layer instead of just staying at the interface (Figure 5.8A). So it can probe the heterogeneity along the C_{18} chain—solvation heterogeneity, in addition to the architectural distribution. While Rhodamine 6G molecule only diffuses at the C_{18}/acetonitrile interface and almost exclusively reports the architectural heterogeneity due to its positive charge (Figure 5.8B). Although it was impractical to directly measure the solvation heterogeneity alone, because the molecules always probed the heterogeneous architecture inside the 0.3 *fL* confocal probe volume, Nile Red and Rhodamine 6G probes together provided the possibility of estimating the solvation heterogeneity. With the assumption that the nanopores architecture and solvation were two independent sources of heterogeneity, the variance in the Nile Red distribution, denoted as $S^2_{Nile\ Red}$, was then the sum of variances from the two sources. The relative standard deviation in solvation heterogeneity ($S_{solvation}$) was estimated from the variance in architectural heterogeneity ($S_{Rhodamine\ 6G}$) and the variance in both architecture and solvation heterogeneity ($S_{Nile\ Red}$):

$$S^2_{Nile\ Red} = S^2_{Rhodamine\ 6G} + S^2_{solvation} \quad [5.6].$$

$S_{solvation}$ was estimated to be 47.6% based on the 28.7% for architectural ($S_{Rhodamine\ 6G}$) and 55.6% for both architectural and solvation ($S_{Nile\ Red}$) heterogeneities (Table 5.4). Although

the two environmental characteristics were likely not independent, for example, the high and low density sites (straight nanopores and the corners in the nanopore network) would have quite different solvation properties, this evaluation provided an estimation of the level of heterogeneity generated by solvation process. Specifically, it appeared that the nanopore architecture and the solvent penetration contributed to the nanoenvironmental distribution at a similar extent.

As one of the pronounced advantages for the single molecule measurements, this methodology provided sufficient spatial and temporal resolution, as well as sensitivity to approach the nanometer scaled gradient of depth-dependent heterogeneity at the C_{18}/acetonitrile interface through the correlation between nanopolarity and diffusion coefficient. Figure 5.9 shows the distribution of fluorescence intensity ratio $R(I_{600}/I_{650})$ of Nile Red photon bursts for 200 randomly selected data traces. With the calculated $R(I_{600}/I_{650})$ values ranging from 0.25 to 8.00, the figure clearly states that the diffusing molecules are able to scan over the entire polarity range elaborated in calibration curve within the time period of one data trace. It also signifies that the entire profile of heterogeneous nanopolarity at the interface can be thoroughly described by the individual diffusing molecules in one data trace. Since burst with different ratio $R(I_{600}/I_{650})$ indicates the molecular diffusion in the environment with different nanopolarity, in order to correlate the nanopolarity to diffusion coefficient, photon bursts in the data trace were firstly divided into five different groups according to their $R(I_{600}/I_{650})$ values. The boundaries of $R(I_{600}/I_{650})$ values for the five groups were listed in Table 5.5. The boundaries were designed to resolve the information of molecular diffusion in the signature polarity regions which were also referred to in Table 5.5. The diffusion

coefficients of Nile Red molecules of the 5 grouped polarity regions were then intended to be approached. Practically, to obtain the diffusion coefficient of the Nile Red molecules diffusing in a certain polarity region, the group of photon bursts within the assigned region based on their $R(I_{600}/I_{650})$ value was selected out, followed by calculating the autocorrelation function of the intensity fluctuations associated with the selected bursts and the fitting of calculated results to the 3-D diffusion model. The burst selection process was performed with a program written in Matlab (Mathworks Inc., Natick, MA). The diffusion coefficients of Nile Red molecules diffusing in the five polarity regions were respectively extracted from the original data traces as the method describe above. 50 randomly selected fluorescence data traces were analyzed to demonstrate the reproducibility of the results. According to the data listed in Table 5.5, the correlation between nanopolarity and diffusion coefficient were plotted in Figure 5.10. The figure demonstrates the decrease in diffusion coefficient with the decrease in nanopolarity at the C_{18}/acetonitrile interface. The significance of this curve was concluded as (1) it demonstrated the existence and nature of environmental heterogeneity by elaborating the gradient of nanopolarity along the penetration direction of Nile Red molecule/acetonitrile into C_{18} layer at nanometer dimension; (2) it served as the calibration to achieve the quantitation of the depth-dependent heterogeneity at the C_{18}/acetonitrile interface through the measurement of diffusion coefficient of individual dye molecules.

5.4. Conclusions

In this work, a powerful approach to probe the nanoenvironmental heterogeneity in nanopores using single molecule fluorescence measurements has been established. Environmental heterogeneity has been explored extensively because it plays an important

role in the biological functions of proteins, vesicles and membranes. The studies so far, however, have relied upon bulk measurements. The ensemble measurements have necessitated that a hypothesis is made that environmental heterogeneity does exist in the system and the experimental data are fit with a predetermined distribution. The single molecule approach stated in this work directly (1) reveals if a distribution of nanoenvironments exists and (2) measures the shape and nature of the distribution. Although it is intuitive that in biological structures, protected hydrophobic regions, such as the interior of a protein molecule and the central region of a membrane possess lower polarity and higher viscosity than the interfacial regions, such as the solvent exposed surfaces where water inclusion occurs, it is difficult to measure the two biophysical parameters simultaneously. Our single molecule approach provides a direct correlation between the nanoenvironmental polarity and viscosity. Significantly, since the two environmental parameters are with the same probe (Nile Red) in the same experiment, the correlation directly validates the long-standing hypothesis that the same structural feature—the inclusion of the solvent molecules—is responsible for the gradients in nanopolarity and nanoviscosity. With this capability, it is envisioned that the single molecule ratiometric spectroscopy can become an excellent tool of information for biological structures and nanosystems.

Table 5. 1 Fitting results of five representative data traces

Trace Number	D (cm^2/s)	Error (D)	R^2
1	1.035×10^{-6}	0.042×10^{-6}	0.96
2	2.081×10^{-6}	0.083×10^{-6}	0.98
3	1.580×10^{-6}	0.072×10^{-6}	0.96
4	1.270×10^{-6}	0.056×10^{-6}	0.96
5	0.965×10^{-6}	0.033×10^{-6}	0.97

Table 5. 2 Distributions of diffusion coefficients of Rhodamine 6G in the 16 spatial locations

Particle number	Pixel number	Average D (cm^2/s)	Standard deviation of D (cm^2/s)	Relative standard deviation (%)
1	1	1.183×10^{-6}	0.360×10^{-6}	30.4
	2	1.179×10^{-6}	0.279×10^{-6}	23.7
	3	1.084×10^{-6}	0.250×10^{-6}	23.1
	4	1.011×10^{-6}	0.231×10^{-6}	22.8
	5	0.925×10^{-7}	0.225×10^{-6}	24.3
	6	1.328×10^{-6}	0.377×10^{-6}	28.4
	7	1.389×10^{-6}	0.364×10^{-6}	26.2
	8	1.422×10^{-6}	0.330×10^{-6}	23.2
	9	1.355×10^{-6}	0.345×10^{-6}	25.4
	10	1.216×10^{-6}	0.246×10^{-6}	20.2
2	1	1.271×10^{-6}	0.392×10^{-6}	30.9
3	1	1.550×10^{-6}	0.438×10^{-6}	28.3
4	1	1.339×10^{-6}	0.326×10^{-6}	24.3
5	1	1.146×10^{-6}	0.323×10^{-6}	28.2
6	1	1.177×10^{-6}	0.351×10^{-6}	29.8
7	1	1.210×10^{-6}	0.332×10^{-6}	27.5
Global average		1.237×10^{-6}	0.323×10^{-6}	26.1

Table 5. 3 Distributions of diffusion coefficients of Nile Red molecules

Particle number	Pixel number	Average D (cm^2/s)	Standard deviation of D (cm^2/s)	Relative standard deviation (%)
1	1	9.62×10^{-7}	4.85×10^{-7}	50.4
	2	9.44×10^{-7}	4.96×10^{-7}	52.5
	3	8.32×10^{-7}	4.53×10^{-7}	54.4
	4	9.43×10^{-7}	4.76×10^{-7}	50.4
2	1	7.99×10^{-7}	4.85×10^{-7}	60.7
	2	8.05×10^{-7}	4.94×10^{-7}	61.4
Global average		8.81×10^{-7}	4.82×10^{-7}	54.7

Table 5. 4 Comparison between the distributions of diffusion coefficients of Rhodamine 6G and Nile Red

Probe molecule	Average D (cm^2/s)	Standard deviation of D (cm^2/s)	Relative standard deviation (%)	physical significance of *RSD*
Rhodamine 6G	1.33×10^{-6}	3.83×10^{-7}	28.7	$S_{rhodamine\ 6G}$: architectural heterogeneity
Nile red	8.45×10^{-7}	4.70×10^{-7}	55.6	$S_{Nile\ red}$: architectural and solvation heterogeneity

Table 5. 5 Summaries of the five different polarity regions for nanopolarity studies

Region number	$R(I_{600}/I_{650})$	Average $R(I_{600}/I_{650})$	Average D (cm^2/s)	Signature of polarity region
1	0.25-1.05	0.83	1.08×10^{-6}	Silica/acetonitrile interface: environment with high polarity
2	1.05-1.25	1.15	9.32×10^{-7}	C_{18}/acetonitrile interface: environment with medium polarity
3	1.25-1.65	1.42	7.87×10^{-7}	
4	1.65-2.75	1.99	6.85×10^{-7}	Transitional region: environment with low polarity
5	2.75-8	4.45	6.35×10^{-7}	100% Octane: apolar environment

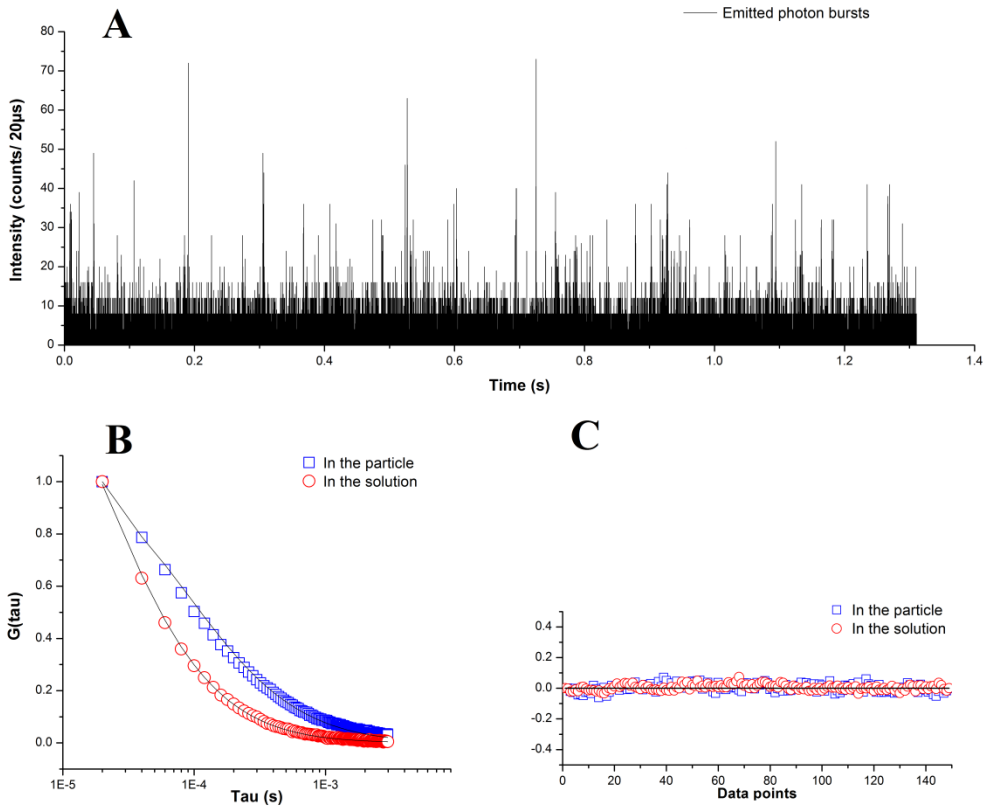

Figure 5. 1 Single molecule fluorescence in nanopores

Note: (A) A fluorescence data trace showing photon bursts; (B) Average autocorrelation functions of 100 data traces and the NLLS fittings to the 3-D diffusion model; (C) Corresponding residual plots.

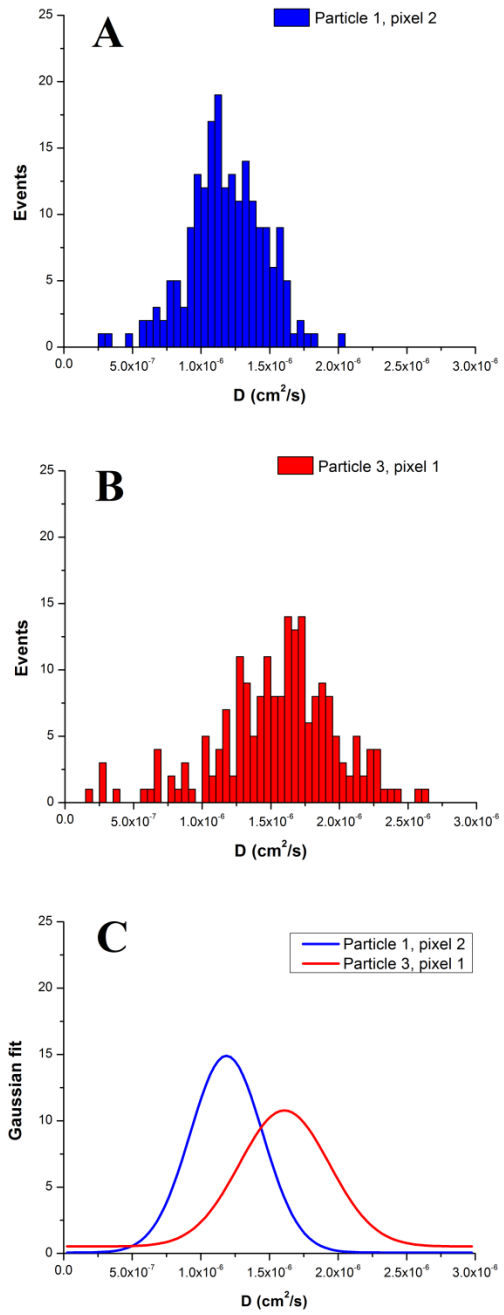

Figure 5. 2 Distributions of diffusion coefficients of Rhodamine 6G for two representative pixels

---

Note: (A) Distribution for particle 1, pixel 2; (B) Distribution for Particle 3, pixel 1; (C) Corresponding Gaussian fitting curves for the two distributions.

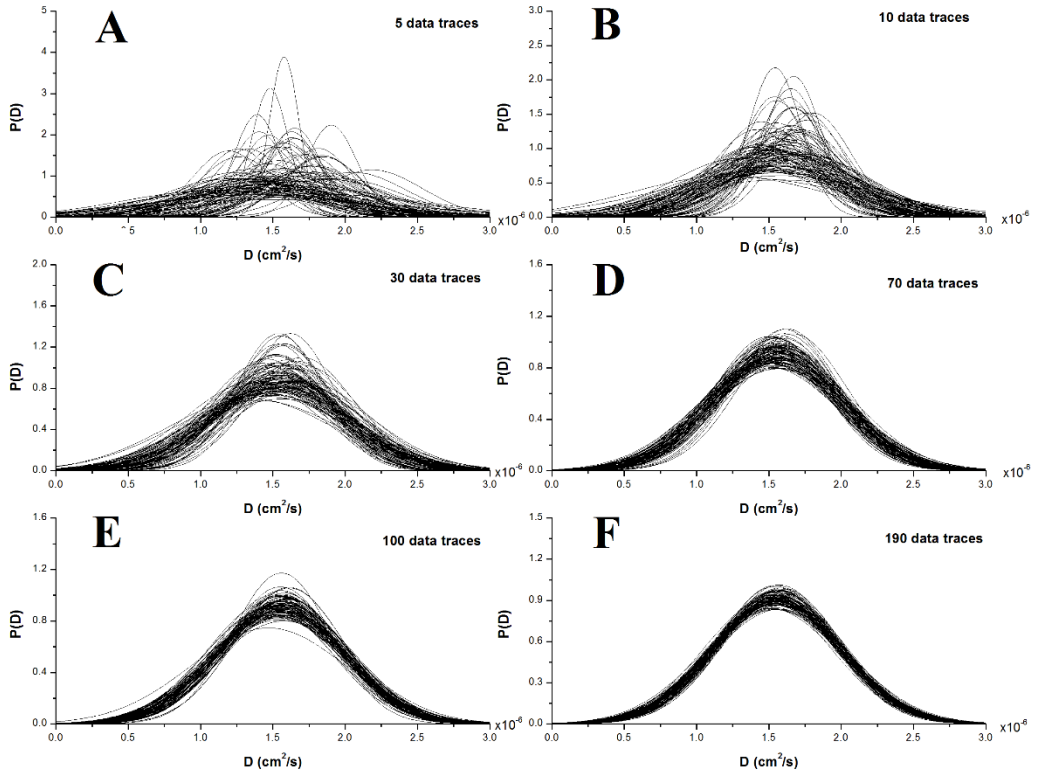

Figure 5. 3 100 replicates of Gaussian distributions of diffusion coefficients

---

Note: 100 replicates of Gaussian distributions of diffusion coefficients for 5 (A), 10 (B), 30 (C), 70 (D), 100 (E) and 190 (F) randomly selected data traces.

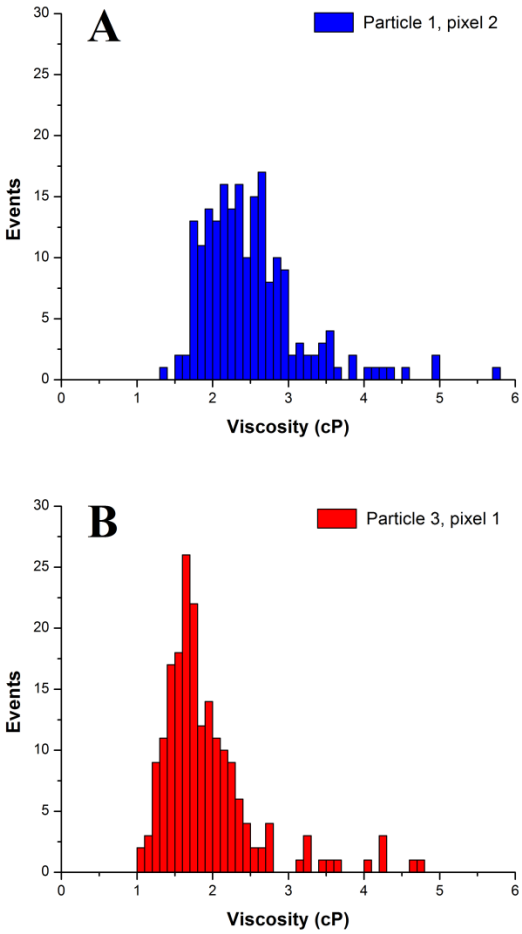

Figure 5. 4 Distributions of nanoviscosities

Note: Distributions of nanoviscosities for particle 1, pixel 2 (A) and particle 3, pixel 1 (B).

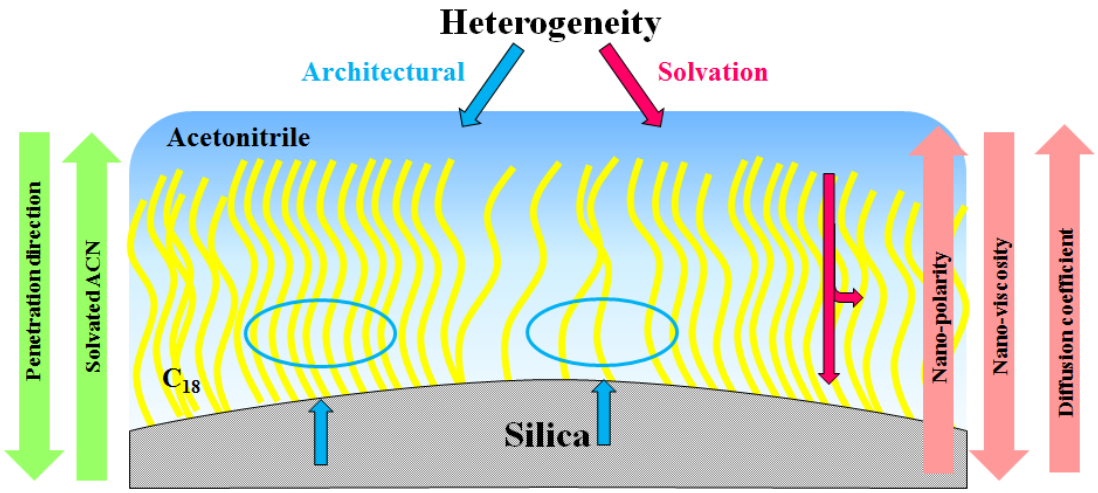

Figure 5. 5 Illustration of architectural and solvation heterogeneities at C_{18}/acetonitrile interface

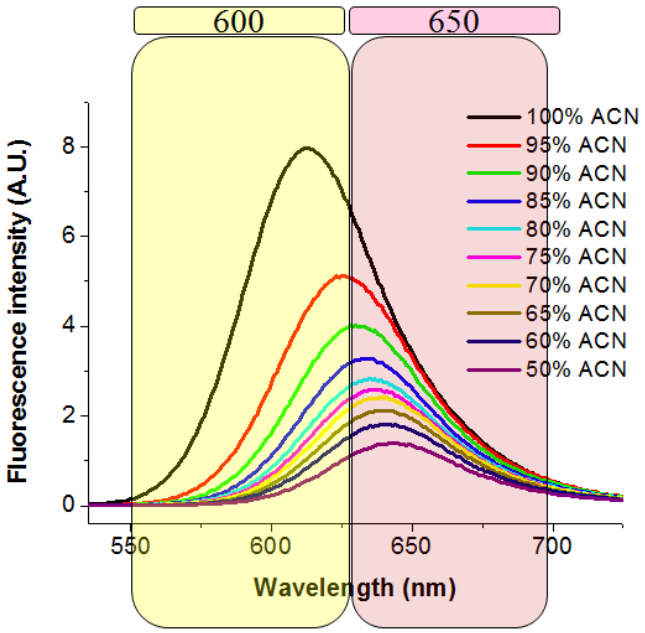

Figure 5. 6 Ratiometric measurement of single molecule fluorescence of Nile Red molecule

---

Note: Red shift in fluorescence emission spectrum of Nile Red when the environmental polarity is increased. The emitted photons are separately collected in two detection channels. One collects photons in short-wavelength region (centered at ~600 *nm*, I_{600}) and the other collects photons in long-wavelength region (centered at ~650 *nm*, I_{650}). The ratio of I_{600} to I_{650}, known as polarity ratio *R*, is inversely proportional to environmental polarity.

Source: adapted from [118].

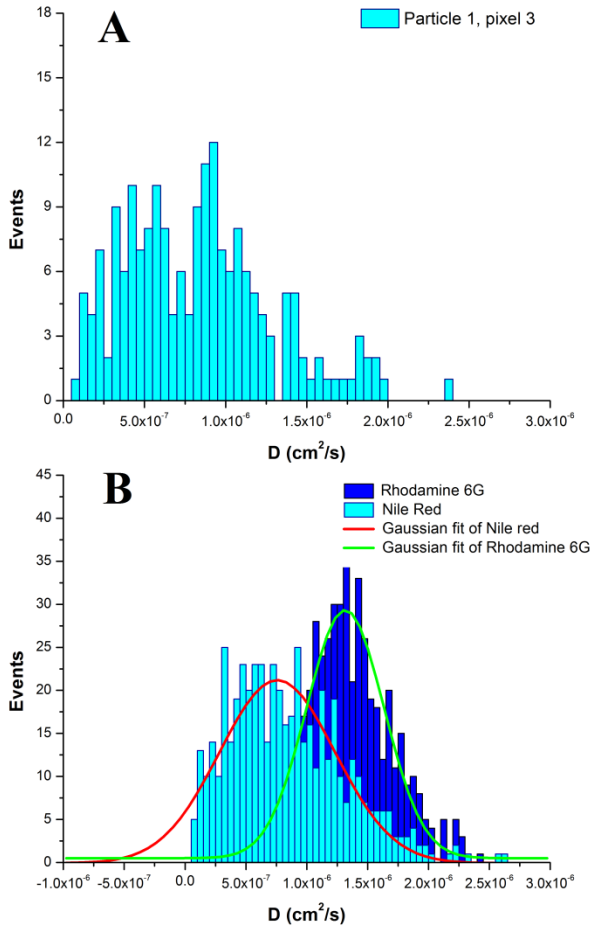

Figure 5. 7 Distribution of diffusion coefficients of Nile Red and its comparison to that of Rhodamine 6G

Note: (A) The distribution of 200 diffusion coefficients of Nile Red at a representative pixel; (B) Comparison between distributions of 500 random-selected diffusion coefficients from entire data pool for Rhodamine 6G and Nile Red at the C_{18}/Acetonitrile interface.

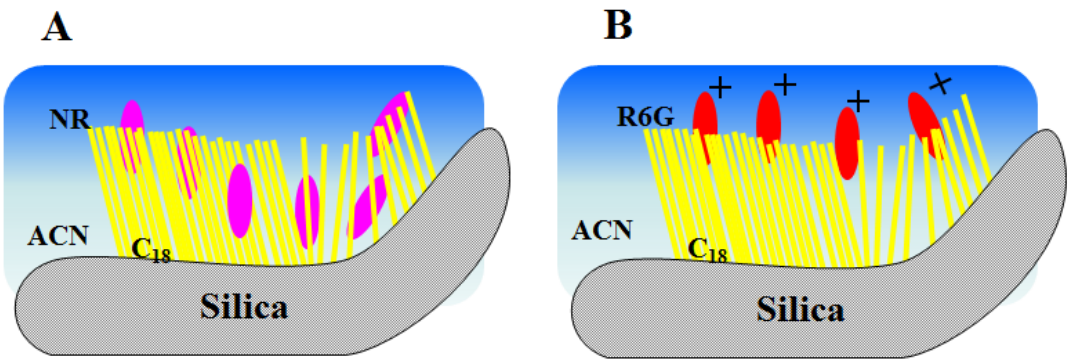

Figure 5. 8 Schematics of molecular behaviors of Nile Red and Rhodamine 6G at C_{18}/Acetonitrile interface

---

Note: Molecular behavior of Nile Red (A) and Rhodamine 6G (B) at C_{18}/Acetonitrile interface. NR and R6G are Nile Red and Rhodamine 6G, respectively. And ACN represents acetonitrile.

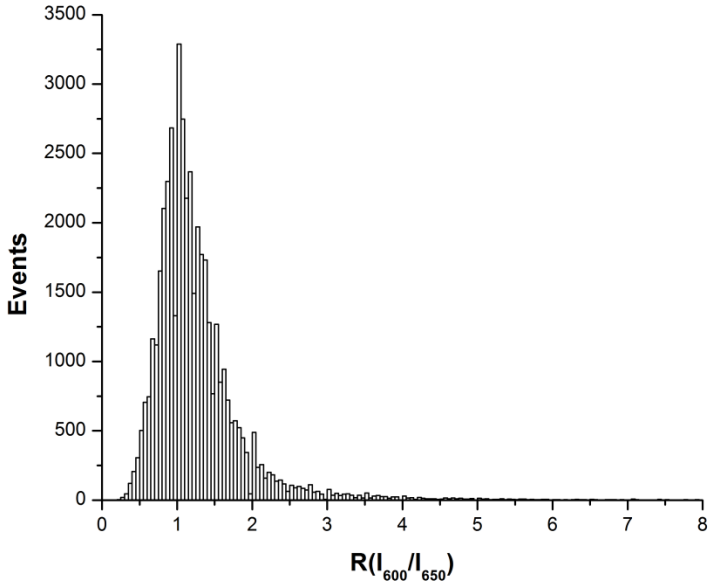

Figure 5. 9 Histogram of fluorescence intensity ratio $R(I_{600}/I_{650})$ of Nile Red photon bursts for 200 data traces collected at a representative pixel

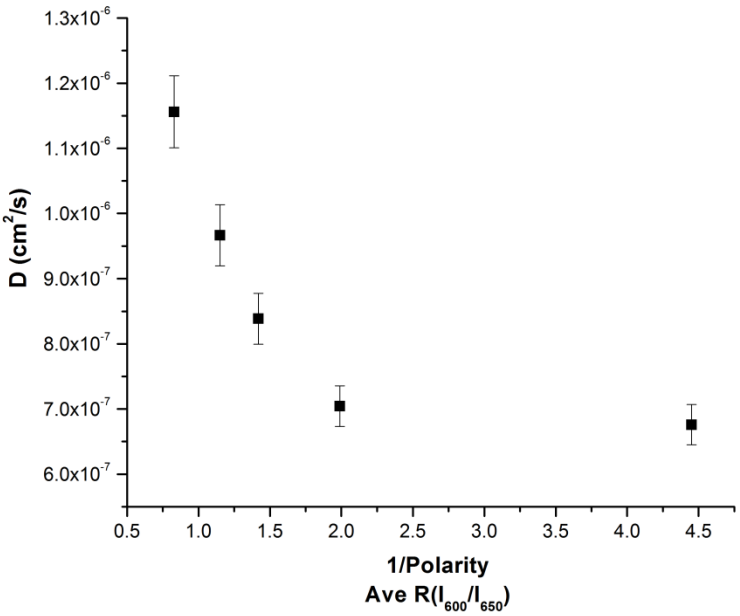

Figure 5. 10 Correlation between diffusion coefficient *D* and nanopolarity indicated by $R(I_{600}/I_{650})$

CHAPTER 6

INVESTIGATION OF ΔG DISTRIBUTION IN NANOPOROUS SILICA PARTICLES WITH CONFOCAL IMAGING

6.1. Introduction

Nanoporous silica materials have attracted great interest in the fields of chemical separation and catalysis due to several remarkable features such as high surface area-to-volume ratio, flexible modification of surface, size-tunable network of nanopores as well as the thermal and chemical stability.

With large contact surface areas which lead to significant improvement of reaction efficiency, nanoporous silica materials have been widely employed as solid support for inorganic, organic, nanoparticle-based and enzymatic catalysis [209-213]. The first application of using nanoporous silica as solid-support in catalysis was reported by Aida in 1999. They developed a modern methodology to synthesize size controlled crystalline nanofibers with high molecular weight by nanoporous silica supported polymerization of ethylene [214]. Ever since the success of this work, more potentials of nanoporous silica materials in catalysis have been continuously discovered and employed in various types of catalytic reactions [215-218]. In recent years, nanoparticle-based catalysts supported by mesoporous silica have drawn significant amount of attention. The catalytic nanoparticles along with mesoporous channels employing the confinement effect and acting as nano-reactors exhibit superior catalytic activities in many types of catalytic reactions such as the aerobic oxidation of alcohols and biomass conversions [219-221]. The most commonly used mesoporous silica materials for this purpose are MCM-41 and SBA-15. Both of them have ordered mesoporous silica (OMS) structures [222]. For the

manufacturing of catalytic Au nanoparticles, for example, the solid support MCM-41 or SBA-15 is firstly mixed into $HAuCl_4$ solution overnight to allow $HAuCl_4$ molecules to diffuse into the network of mesopores and deposit uniformly onto the porous surface. $NaBH_4$ is then subsequently introduced into the pores for the reduction of Au (III). Yang and coworkers investigated the catalytic efficiency of aerobic oxidation of 1-Phenylethanol and its paraderivates by using the home-synthesized mesoporous silica supported Au nanoparticles as the catalyst. [219] According to their results, the conversion efficiency catalyzed by mesoporous silica supported Au nanoparticles was 3 times higher than that catalyzed by soluble palladium complex. In a recent study in 2015, the researchers further adopted the mesoporous silica supported Au and AuCu nanoparticles for plasmonic photocatalysis by investigating the reaction rate improvement of glycerol oxidation assisted by visible light [223]. This work demonstrated that nanoparticles supported by monodisperse mesoporous silica spheres exhibited much higher catalytic activity than that supported by traditional OMS materials.

As demonstrated in these studies, nanoporous silica acts as a superior solid support in catalysis. Its porous structure provides high capacity of reaction sites for reactants to deposit onto the surface of network of nanopores. Each reaction site is then considered as a nano-reactor where catalytic reaction occurs. It has been proposed that the difference in properties of nanoporous silica such as type of functionalized layer, surface coverage density and pore size could significantly contribute to the heterogeneity in overall catalyst and eventually lead to the variation in catalytic activity [224]. Even though the synthesis techniques for nanoporous silica materials have been improving over time, the inherent pore size distribution and the resulting heterogeneity after surface

modification still make the material "inhomogeneous" [225] . These "inter-piece" and "intra-piece" heterogeneities in the microscopic environments of nanoporous silica solid supports for catalysis are of great interests to investigate for addressing the existence of heterogeneity in catalytic activity and its fundamental origins.

On the other hand, nanoporous silica particles are also widely employed as the stationary phase in chromatographic separation. Different separation modes require specific surface modification of nanoporous silica particles. Octadecylsilyl (C_{18})-modified nanoporous silica particle, for instance, is extensively used in reversed-phase liquid chromatography (RPLC). Despite years of developments and applications in both academic and industrial fields, band broadening persistently remains as one big issue. It leads to poor resolution and reduction of separation efficiency. The three well-known sources for band broadening are (1) different paths for molecules' diffusion throughout the column, (2) longitudinal diffusion and (3) insufficient time for target molecules to achieve chemical equilibrium between the mobile phase and stationary phase. An inherent assumption of this theory is that all particles are uniform and chemically and physically identical.

It has been noted that all modified adsorbent surfaces are heterogeneous because foreign elements of the bulk material would tend to segregate at the surface [225]. Gritti revealed the existence of heterogeneous adsorption sites located not only on the exposed silanol groups on the surface but also inside the hydrocarbon chains of the modified nanoporous silica particles. Intuitively, the naturally existing heterogeneity in physicochemical properties of the stationary phase can be a significant origin of band broadening in chromatographic separation. Tremendous researches have been conducted

towards the heterogeneity in physicochemical properties of nanoporous silica particles in order to have deeper understanding of band broadening issue. The polarity of stationary phase – a physical parameter directly related to the retention in chromatographic separation is the most popular area and has been studied in different ways [226-228]. Zhong and Geng reported the polarity distribution in the microenvironment of C_{18} modified stationary phase by using fluorescence confocal ratiometric imaging. They used a polarity-sensitive fluorescent dye molecule as the reporter of local environments. This work well explained the microscopic origins of band broadening in separation.[118] Other imaging techniques such as atomic force microscopy and photographic imaging have been utilized to characterize the outer surface structure of silica particles, and to monitor the separation process at large (mm) scales [229, 230].

In summary, the heterogeneity in physicochemical properties of silica materials plays a significant role on catalytic efficiency of nanoporous silica-supported catalysis as well as the chromatographic separation efficiency. To fully optimize the functional properties and maximize the efficiency of these materials, it is crucial to achieve an in-depth understanding of physicochemical properties and their distributions of nanoporous silica.

In this chapter, the investigation on ΔG distribution of microenvironments of C_{18} modified nanoporous silica particles is carried out by both laser scanning confocal microscopy imaging and stage scanning confocal microscopy imaging. This work brings in-depth understanding of microscopic origin of heterogeneity in nanoporous silica materials and provides a quantitative assessment of the level of heterogeneity.

Furthermore, it fundamentally explains the previous-mentioned phenomenon in catalytic activity and band broadening since ΔG governs the chemical processes at the interface.

6.2. Experimental

6.2.1. Chemicals and materials

Rhodamine 6G was purchased from Sigma Aldrich (Milwaukee, WI) and its chemical structure was shown in Figure 3.1. HPLC grade acetonitrile and microscopic coverslips (12-545-G, size 50×35 *mm*, thickness 0.13-0.17 *mm*) were purchased from Fisher Scientific (Fair Lawn, NJ). The coverslips were thoroughly cleaned and rinsed with deionized water produced by a MilliQ system (MilliQ-Plus, Millipore, Bedford, MA) before use. The optical glue (NOA 68) used for sealing sample slides was obtained from Norland products (Cranbury, NJ). Immersion oil (type LDF) with refractive index of 1.51 (Cargille Laboratories Inc., Cedar Grove, NJ) was used for confocal microscopic imaging.

The Luna C_{18}-derivatized nanoporous silica particles were obtained from Phenomenex (Torrance, CA) as a gift. The physicochemical properties of the particles provided by the manufacturer were summarized in Table 3.1.

6.2.2. Instrumentation and measurements

6.2.2.1. Loading of Rhodamine 6G into C_{18}-derivatized nanoporous silica particles

10 μM Rhodamine solution was freshly prepared with HPLC grade acetonitrile upon use. 0.09949 *g* of particles were weighted out an using analytical balance (Mettler Toledo, AG245, Columbus, OH) and mixed with 3 *mL* of Rhodamine 6G solution in a vial. The vial was vortexed using a vortex mixer (Fisher Scientific, Pittsburgh, PA) at 900

rpm for 1 min, followed by slow mixing with a rotatory mixer (Glas-Col®, Terre Haute, IN) at 100 *rpm* overnight to ensure the equilibrium of Rhodamine 6G molecules between particle interfaces and acetonitrile solvent. The vial was covered with aluminum film to avoid potential photobleaching of the fluorescent molecules.

6.2.2.2. Imaging of the loaded particles

The ΔG distribution of the particles was investigated by two different fluorescent confocal microscopy systems. The preliminary study was performed using the home-built stage-scanning confocal microscope system with capability of single molecule detection. The schematic diagram was shown in Figure 3.2. Generally, the 514.5 *nm* excitation light beam was generated by an air-cooled argon ion laser. Neutral density filters were employed to reduce the laser power to 0.3 *mW*. A 100X oil-immersion microscope objective with numerical aperture (NA) of 1.45 was used as the condenser and for fluorescence light collection. To achieve selection and efficient detection of Rhodamine 6G's fluorescence emission, a 560 *nm* bandpass filter with a bandwidth of 55 *nm* (Omega Optical, 560RDF55) and an avalanche photodiode (APD) (SPCM-AQR, PerkinElmer Optoelectronics) were applied in the emission channel. A 50 μm confocal pinhole provided a lateral image resolution of ~ 250 *nm* and an axial resolution of ~ 1 μm.

The following in-depth investigations were conducted with a commercial confocal microscope Zeiss LSM710 (University of Iowa Central Microscopy Research Facility) for its convenience in operation and image construction. Concisely, this commercial microscope has an upright laser-scanning configuration, and is equipped with a pigtail-coupled laser providing 6 options of excitation wavelength in visible light range from 405 *nm* up to 633 *nm*. The 514 *nm* laser beam and a 63x oil-immersion microscope

objective were selected for fluorescence imaging in this work. A low noise, high sensitivity 32-channel PMT was used for detection.

6.2.2.3. Imaging system calibration

The Zeiss LSM710 confocal microscopic imaging system was calibrated using a series of Rhodamine 6G solutions with a broad range of concentrations, from 3.3 μM up to 250.0 μM. The concentration range of Rhodamine 6G solutions for calibration was determined with consideration to fully cover the concentration range of Rhodamine 6G molecules in particles. The details will be elaborated in a later section.

A standard stock Rhodamine 6G solution with concentration of 1000 μM was freshly prepared. The diluted solution at each specific concentration was then prepared by incrementally adding drops of the stock solution with a pipette (Eppendorf Research, 10-100 μL). In the meanwhile, 30 μL of each diluted solution was dispensed onto a coverslip and immediately imaged by Zeiss LSM710 at the same settings as imaging of particles.

6.3. Results and Discussions

6.3.1. Image formation in confocal microscopy

6.3.1.1. Principles of image formation in confocal microscopy

Different from conventional microscopy technique where the image is instantaneously formed upon detection of entire image from the microscope objective using a multichannel imaging detector, confocal microscopy imaging undergoes a point-by-point and line-by-line scanning process. The laser beam firstly passes through an aperture and objective which focuses the excitation light into specimen as a diffraction-limited focal volume (also called as probe volume) at sub-micron dimension. The emitted

fluorescence from the probe volume is transmitted through a dichroic mirror, focused by the objective lens and reaches the pinhole. The pinhole rejects all out-of-focus fluorescence and only allows the photons coming from the focal plane to pass through to the single-channel detector. The detected photons are transformed into electric signal and presented as the resulting image. The detected signal coming from the probe volume in the specimen constitutes one pixel of the resulting image. As the laser beam is directed to scan over the area of interest in the specimen with point-by-point scanning to form a line and then line-by-line scanning following a zigzag route (Figure 6.1A), the two-dimensional image is achieved. A typical 2-D image represents an optical slice within a certain thickness of specimen and may be composed by 512 lines each comprised 512 pixels. In other words, each 2-D image contains 262,144 digital pixels, shown as the schematic in lower right corner of Figure 6.1A. Each 2-D image corresponds to an image plane in the axial dimension (Z-axis) and therefore, 3-D image of the specimen can be collected by stacking a series of 2-D images taken at different image planes of Z-axis together (Figure 6.1B).

Generally, there are two types of confocal microscopy systems: laser-scanning confocal microscopes (LSCM) and stage-scanning confocal microscopes. Most commercial confocal microscopy systems nowadays, including the Zeiss 710 system employed in this investigation, are laser scanning which achieves the scanning of sample by tuning the laser beam to move the locations of focal volume using one or more mirrors in the excitation light path. While the home-built confocal microscopy system in our research lab is a stage scanning imaging system and its image formation process is discussed in detail in the next section.

6.3.1.2. Image formation in stage-scanning confocal microscopy

The home-built stage-scanning confocal imaging system was constructed by former Geng group members Mark Lowry and Zhenming Zhong. Specifically, the scanning sample stage is consisted of an xy piezoelectric scanning stage (Model: P-527.2CL, Physik Instrumente, Germany) and a piezoelectric objective stepper (Model: P-721CL, Physik Instrumente, Germany) to achieve 3-D scanning (200 μm × 200 μm× 100 μm)[109]. The system possesses several advantages. (1) The number of optics in the light path is significantly reduced since the focal volume of the laser beam stays fixed during the imaging process and there is no need to move the focal point across a three-dimensional space. Therefore, photon collection efficiency can be significantly improved. (2) The scanning stage employed in this system can achieve sub-nanometer resolution in all three dimensions, to ensure that the spatial resolution of the image is truly defined by the diffraction limit.

Similar to laser-scanning confocal microscopy system, image formation in stage-scanning system also follows the principle of point-by-point and line-by-line scanning procedure. However, instead of tuning the laser beam to change the location of focal volume using mirrors, a program (written in LabVIEW) driven digital piezo controller (Model: E-710.P4L, Physik Instrumente, Germany) is used to make the stage move following a zigzag pattern to ensure thorough scanning of sample of interest in a manner of point-by-point along a line and line-by-line across the entire image plane. The scanning speed, integration time and step size of the stage's movement are determined by the program sent to the digital controller.

The multichannel scaler (MCS) (Model: MCS-pci, Ortec, Oak Ridge, TN) utilized to count the time-dependent electronic TTL pulses generated from detected photons is able to collect 65536 channels at maximum (16-bit). Figure 6.2A shows the original time-dependent data trace directly collected during the imaging process. In this imaging experiment, the scanning velocity was set to be 0.5 $\mu m/ms$, the integration time was 1 *ms* and the step size was consequently determined to be 0.5 μm. The image size was 100 μm× 100 μm. As a result, there were 40401 out of 65535 channels were used and the image was composed by 40401 digital pixels in total. Since the image was taken following a zigzag route of point-by-point scanning to form a line and then line-by-line scanning across the entire image plane, there was a correlation between the directly measured time-dependent signal and spatial location of each pixel forming the image. The time-dependent data trace was thus converted to the space-dependent image with size of 201 ×201 pixels (Figure 6.2B).

6.3.2. Preliminary studies on home-built confocal microscopy

6.3.2.1. Conceptual Basis for Imaging ΔG at C_{18}-acetonitrile interfaces

In the field of RPLC, the target molecule represented by A partitions from the mobile phase into the stationary phase and intends to achieve equilibrium during the separation process. The equilibrium is expressed as:

$$A_{mobile} \overset{K_c}{\leftrightarrow} A_{stationary} \qquad [6.1]$$

where K_c is the equilibrium constant. In our case, the equilibrium of Rhodamine 6G molecules between acetonitrile solvent and C_{18}-derivatized interfaces of nanopores inside the chromatographic particles is established along the fluorophore loading process:

$$Rhodamine\ 6G_{acetonitrile} \overset{Kc}{\leftrightarrow} Rhodamine\ 6G_{nanopore\ interfaces\ in\ particles} \quad [6.2].$$

Therefore free energy ΔG at the C_{18}-acetonitrile interface inside the particles is determined by:

$$\Delta G = -RTlnK_c \quad [6.3]$$

where equilibrium constant K_c is assessed by the concentration of Rhodamine 6G in the particle and that in acetonitrile solvent, which is described by:

$$K_c = \frac{[Rhodamine\ 6G]_{interface}}{[Rhodamine\ 6G]_{acetonitrile}} \quad [6.4].$$

In the constructed confocal images, these two concentrations correspond to the fluorescence intensity detected inside the particle and the intensity detected in the solution outside particle, respectively. As a result, the equilibrium constant K_c is evaluated as follows:

$$K_c = \frac{[Rhodamine\ 6G]_{interface}}{[Rhodamine\ 6G]_{acetonitrile}} = \frac{I_{interface}}{I_{solution}} = \frac{I_{particle}}{I_{outside\ particle}} \quad [6.5]$$

and the ΔG at C_{18}-acetonitrile interfaces inside particle is thus calculated by:

$$\Delta G = -RTlnK_c = -RTln\frac{[Rhodamine\ 6G]_{interface}}{[Rhodamine\ 6G]_{acetonitrile}}$$

$$= -RTln\frac{I_{interface}}{I_{solution}} = -RTln\frac{I_{particle}}{I_{outside\ particle}} \quad [6.6].$$

Although the conceptual framework of the ΔG imaging is quite intuitive, the key to the project is in the experimental details. As this is the first pixel-by-pixel and particle-by-particle evaluation of the energetics in nanoporous silica, to our knowledge, it is of crucial importance to make sound analytical measurements to extract the free energy

distribution. Especially, it is known that in imaging experiments the illumination field is not flat so the fluorescence intensity can be quite different for exactly the same concentration of molecules across the entire image field. In confocal microscopy, there can be significant field curvature in laser intensity as the result of mirror scanning (*vida indra*). This broad distribution in intensity, and thus the intensity ratio, can be easily interpreted as an apparent "free energy distribution". The noise level needs to be carefully considered to interpret the statistical confidence in the free energies. The details of the quantitative confocal imaging are described in the following sections.

6.3.2.2. Solution analysis for imaging system evaluations

The primary consideration for imaging ΔG with the home-built confocal system is the flat illumination plane, as the geometry for image formation stays the same in data collection. To test this hypothesis, we used the solution fluorescence as the intensity standard. The fluorophore concentration is expected to be the same in the solvent across the entire image. 12 regions of solution outside particles were randomly chosen across the entire constructed image and their general locations were marked and displayed in Figure 6.2B. The size of each selected spot was 10 ×10 pixels. The key to defining the location of each region was ensuring the selected pixels are completely in the solution phase and representative of the solution environment outside the silica particles. The average fluorescence intensity of each selected region was calculated in order to investigate the intensity uniformity of illumination field and the stability of the piezo flexure stage during the image-scanning process. The calculation results were summarized in Table 6.1.

As shown in Table 6.1, these 12 spots have an average intensity of 36.5 photon counts with a standard deviation of 3.2 counts. The corresponding relative standard deviation (RSD_{all}) which corresponds to intensity variation of all 12 regions is about 8.7%. Figure 6.3A shows the average intensities of the 12 regions. The intensities exhibit a random fluctuation in the image plane (Figure 6.3B) and it demonstrates that there is no intensity drift pattern across the image field. On the other hand, the error bars in Figure 6.3A represent intensity fluctuations among the 100 pixels selected for each region. This intensity fluctuation ranges from 6.8 counts to 10.2 counts and corresponds to relative standard deviation (RSD_{in}) of 17.9% to 27.9% (Table 6.1).

In conclusion, the solution signal analysis manifested (1) there was about 9% intensity variation or non-uniformity across the entire illumination field. This variation was most possibly attributed to the slight drift of the piezoelectric microscope objective stepper along the axial direction during the image-scanning process; (2) there does not seem to exist any intensity drift pattern in the illumination field as the fluctuation of fluorescent intensities at different regions is quite random; And (3) the confocal microscope instrument exhibited quite significant systematic fluctuation during measurements (around 20%) which was estimated by the relative standard deviation of fluorescence intensity fluctuation of the 100 selected pixels for each region—RSD_{in}. The analysis and interpretation of this systematic fluctuation was illustrated in a later section.

6.3.2.3. Particle analysis for construction of ΔG distribution

There were a total of 125 particles counted in the formatted image shown in Figure 6.2B. An inscribed square area was selected within each particle and the fluorescence intensity of each particle was calculated by averaging the intensities of all

pixels in the inscribed square area. As illustrated in Table 6.2, the intensities of the particles show a tremendous fluctuation with an average intensity of 204.8 counts and a standard deviation of 76.8 counts which corresponds to a *RSD* of 16.9%.

In the actual circumstances, the readout (measured) fluorescence intensity was corrected considering the non-negligible scattering of the acetonitrile solvent. In other words, the readout photon counts were the sum of the photon counts of emitted fluorescence from Rhodamine 6G and the photon counts of the scattering from the surrounding environment and depicted as:

$$Photon\ counts_{readout} = Photon\ counts_{Rhodamine\ 6G} + Photon\ counts_{scattering} \quad [6.7].$$

Therefore, the previously derived expression of equilibrium constant K_c was modified to be:

$$K_c = \frac{I'_{Rhodamine\ 6G\ in\ particle}}{I'_{Rhodamine\ 6G\ outside\ particle}} = \frac{I_{readout\ in\ particle} - I_{scattering}}{I_{readout\ outside\ particle} - I_{scattering}} \quad [6.8]$$

and consequently, the ΔG at C_{18}-acetonitrile interfaces inside each particle was delineated to be:

$$\Delta G = -RTlnK_c = -RTln(\frac{I_{readout\ in\ particle} - I_{scattering}}{I_{readout\ outside\ particle} - I_{scattering}}) \quad [6.9]$$

where $I_{scattering\ of\ solvent}$ was the scattering intensity (in photon counts) of the surrounding solvent and assessed by calculating the average intensity of the photon bursts appeared in one data trace of acetonitrile. The average intensity of the scattering bursts was calculated to be 2.5 counts in the integrated time of 100 μs. With an integrated time of 1 *ms* applied in this imaging experiment, the scattering intensity $I_{scattering}$ amounted to 25 counts. Recalling that the average readout intensity of the solution outside of the particles was

about 37 counts, the scattering from the surrounding solvent actually played an important role in accurately estimating the equilibrium constant *Kc* and the corresponding ΔG at the C_{18}-acetonitrile interfaces in the particles.

The ΔGs of all 125 particles were estimated by the corrected intensities and the results were also summarized in Table 6.2. The ΔG distribution of the particles in the image was constructed and shown in Figure 6.4. The figure presents a wide range of the ΔG of particles, from ~ – 4.1 k*J/mol* up to ~ – 9.3 k*J/mol*. To accentuate the shape and width of the distribution, a Gaussian fitting was applied to the distribution and shown in Figure 6.4 as well. The fitting curve demonstrates an average ΔG of ~ – 7.0 k*J/mol* (the center of the curve) and a spread of ~ 2.8 k*J/mol* (the FWHM of the curve).

6.3.3. Imaging system calibration and validation

The preliminary work elaborated above helped to form the conceptual framework for the study of ΔG distribution of the C_{18}-derivatized nanoporous silica particles. To achieve a more comprehensive and in-depth investigation, further studies were performed using the commercial confocal microscope Zeiss LSM710 by taking advantage of its easy operation and convenience in image formation. Several crucial preparation studies of this alternative imaging system were carried out in a way of analytical methodology development before the particle imaging experiments to ensure the justifiability and rationality of the study.

6.3.3.1. Imaging system calibration

We first calibrated the fluorescence intensity of the system. A series of standard Rhodamine 6G solutions with a wide range of concentrations were imaged by the Zeiss

LSM710 confocal microscope. The detailed experimental procedures were described in the Section 6.2.2.3. The images of standard solutions at several representative concentrations were displayed in Figure 6.5.

To build the calibration curve, an area of 20×20 pixels was randomly selected from the image of each solution. The average intensity of the 400 pixels in selected area of each solution and corresponding *RSD* were calculated and summarized in Table 6.3. The calibration curve presented in Figure 6.6 demonstrates an excellent linear dependency between the fluorescence intensity and the solution concentration with R^2 = 0.995. At the most diluted concentration of 3.3 μM, the average intensity of image is 4.5. And at the highest concentration of 250.0 μM, the average intensity increases to about 245.0 which are still below the saturation limit of 255.0. Therefore, it confirms the effectiveness of the instrument to perform imaging experiments within the dynamic range of ~3 μM to ~250 μM. As stated in the results from preliminary studies, the equilibrium constant K_c at C_{18}-acetonitrile interfaces of particle distributed from 5.3 to 24.1. Then the Rhodamine 6G concentration in particles was considered to be 5.3 to 24.1 times higher than that in the solvent outside particles, which was estimated to fall into a range of 53 μM to 241 μM. Indeed, the concentration range depicted in calibration study (Figure 6.6) was demonstrated to completely cover the concentration range of interest and this imaging system was proved to possess sufficient dynamic range for investigating ΔG distribution of the C_{18}-derivatized nanoporous silica particles.

6.3.3.2. Robustness of the imaging system

After demonstrating the dynamic range of the Zeiss LSM710 imaging system using one section of the solution image (20 ×20 pixels), the next consideration was the

robustness of the system. To perform the test of robustness, the image of standard solution at each concentration was divided into 16 sub-images with identical size of 64 ×64 pixels. An example for image division and the corresponding section number was shown in Figure 6.7A.

First of all, the average intensities of all 16 sub-images of each standard solution were all incorporated to re-produce the calibration curve (Figure 6.7B) to explore the robustness of the imaging system, including uniformity of illumination field and stability of the image plane. Figure 6.7B presents a good linear dependence between the average fluorescence intensity of each sub-image versus the concentration with R^2 =0.998. The fitting line shows a slope of 0.93 which is quite close to that of the fitting line in Figure 6.6. On the other hand, all16 data points of each standard solution exhibit great overlap between each other and distribute closely to the fitting line. These facts demonstrated the consistency and reproducibility of signal measured at different locations on the image plane and therefore, evidenced the stability of the imaging system.

Besides testing the stability, the intensity uniformity on the illumination field of the imaging system has also been examined by looking into the intensity distribution of the 16 sub-images for each solution. Even though the intensities of sub-images showed good reproducibility which was demonstrated by the overlap of scatter points in Figure 6.7B, a minor fluctuation in intensity of different sub-image still existed. The average intensity of each sub-image versus the corresponding section number for three representative concentrations were shown in Figure 6.8 A, B and C. Figure 6.8D was an illustration of the general intensity pattern observed on image plane. As clearly shown Figure 6.8D, the intensities at 1^{st}, 4^{th}, 13^{th} and 16^{th} sections (sub-images) which represents

the 4 corners of the image are lowest while the intensities at 6^{th}, 7^{th}, 10^{th} and 11^{th} sections which represents the middle area of the image are brightest. It uncovered a fact that the illumination field of this imaging system has a patterned non-uniform intensity distribution.

To provide further quantitative assessment of the degree of this intensity variation on illumination field, the average fluorescence intensities of all 16 sub-images were evaluated for all available standard solutions respectively. The average intensity, maximum and minimum intensities as well as the corresponding *RSD* of 16 sub-images of each solution were summarized in Table 6.4. As shown in the table, this patterned fluctuation on the illumination plane only leads to ~2% variation in intensity throughout the entire image plane (indicated as *RSD*). And its effect on the particle imaging results was evaluated in a later section.

6.3.4. Method for particle analysis

To improve the efficiency and consistency of data analysis, ImageJ and programs written in Matlab were employed to analyze images of particles. Four slices of the original confocal fluorescence images taken at different areas of the same sample slide were firstly imported into ImageJ and the images displayed by ImageJ were shown as Figure 6.9A, B, C and D. The information of particle in the images was then approached by defining the coordinates of the centroid and radius of each particle. The coordinates and radius of particles were determined by a thresholding procedure in ImageJ. This procedure actually played a decisive role on the analysis results and the details are discussed in the following section.

On the other hand, the original images were also imported into Matlab and presented as matrices. The coordinates of centroid and radius (in μm) of each particle extracted from ImageJ were converted into the pixel indices by dividing the dimension (in μm) by the pixel size of 0.26 μm, and the results were denoted as (X, Y) and R (radius in number of pixels). In this way, the location and size of each particle were transformed into the original image matrices in Matlab. Subsequently, programs written in Matlab were utilized to achieve pixel selection in each particle. Generally, the pixels completely fitting within the circle (particle) defined as $X^2 + Y^2 \leq R^2$ were selected and the pixels partially or completely out of the circle were excluded to avoid edge effect. Figure 6.10 elaborates this method and the selected pixels within one particle are colored in red. With the selected pixels in each particle, the images of particles were reconstructed in Matlab and directly used for further investigation of ΔG distributions.

6.3.5. Thresholding in image reconstruction

As described above, thresholding was an inevitable procedure to collect information of particles in the images. And it actually played an essential role on analysis results by significantly re-orienting the reconstructed images. In ImageJ, there are two ways to perform thresholding of an image: manual and automatic thresholding. The outcomes of these two thresholding methods turned out to be quite different from each other.

Initially, the manual thresholding of the images was employed since this method guaranteed the complete inclusion of the selected pixels of interest inside the particle by manually adjusting the shading areas (the areas to include as the part of particle for

further analysis) of each particle, as illustrated in the green highlighted areas in Figure 6.11. Because of the uneven intensity distribution in the particles, the resulted shaded areas are not all perfect circles since the starting point of thresholding process is the brightest spot of the particle instead of the geometrical center of each particle, as indicated in Figure 6.11A. The ending point is determined by the completion of shading the particle with highest average intensity (Figure 6.11B). At the ending point, the shaded areas of particles with lower average intensities are resulted with skewed shapes due to the incompletion of shading process of itself. The lower the average intensity is, the more skewed the shaded area will be. Several examples of the results of this problematic thresholding method are shown in Figure 6.11C. However, all shaded areas, including the skewed ones were forced to be fitted into circles in ImageJ. This led to an obvious offset in the extracted coordinates of centroid (X, Y) and radius R for the particles with uneven intensity distribution. As a result, there were significant drifts in the circled areas (white circles) defined by ImageJ from the actual positions of particles (yellow circles). And the areas of solution outside particle could be mistakenly included for further analysis, as illustrated in Figure 6.11D.

In the next step, these inaccurate coordinates (X, Y) and R were converted into the pixel coordinates and applied to the original image data matrix stored in Matlab for image reconstruction. One of the four confocal images of particles (Figure 6.11) was used for the presentation of the problematic issues in the pixel selection process in Matlab. Figure 6.12A shows the original image by plotting the data matrix of Figure 6.9B in Matlab. The program written in Matlab forced the selection of pixels to form circled area according to ImageJ-defined pixel coordinates (X, Y) and R. As a consequence of the offsets in the

locations and dimensions of the particles due to the manual thresholding process in ImageJ, some particles in the reconstructed image appeared to be significantly off from the original positions and sizes (Figure 6.12B). Figure 6.12B evidences mistakes in the pixel selections: solution outside some particles is mistakenly included as part of the particles for further analysis (indicated by arrows), while some areas that obviously belong to the particles are excluded (dash circles). The reconstructed image provided inaccurate information of particles and turned out to be inappropriate for further ΔG analysis.

Alternatively, automatic thresholding was utilized. This method offered an auto-shading of the image which provided an auto-selection of shaded areas based on the recognition of particles of ImageJ, shown as the green highlighted areas in Figure 6.13A. The shaded areas were the best approximations to the circles whose coordinates of centroids ((X_a, Y_a)) and radius (R_a) were determined by the actual locations and dimensions of the particles in the image. The circles defined these coordinates (X_a, Y_a) and R_a in Image J were drawn in Figure 6.13B and they accurately reflected the positions and sizes of particles in the original image (Figure 6.9D). In practice, when performing image reconstruction in Matlab, 2 μm was deducted from the R_a, this conservative measure was introduced to ensure that all selected pixels were truly within the interior of particles. The example of areas that were eventually included for image reconstruction was also illustrated in Figure 6.13B. By applying automatic thresholding, the drifts in the positions and sizes of particles in the reconstructed image were effectively avoided and the reconstructed image thus provided accurate information of particles and was able to be directly applied for the further investigation of ΔG distributions.

6.3.6. Construction of ΔG distribution for nanoporous silica particles

A series of studies towards the ΔG distribution at C_{18}-acetonitrile interface of nanoporous silica particles were conducted following the assessments of the imaging system and resolving issues in data processing for particle analysis.

6.3.6.1. Evaluation of scattering from surrounding environments

As elaborated in the preliminary study section, the scattering signal from surrounding solvent had significant effects on the estimation of equilibrium constant K_c. Guided by this finding, the scattering from surroundings of particles on the sample slide was evaluated to ensure the accurate calculations of K_c and corresponding values of ΔG.

Analysis of the image trajectory revealed that the interfering scattering signal was primarily generated by the scattering of the laser beam when it crosses the surface of the coverslip used for sample slide preparation. In order to estimate the overall scattering intensity $I_{scattering}$, a set of 3-D stacked images (16-bit) of particles at the same lateral locations as Figure 6.9 were collected. The imaging scan along the axial dimension started from the surface of the bottom coverslip, moved upwards and ended after the scanning reached the glass surface of the top coverslip. The scanning distance range was 19.87 μm and the interval between two image slices was 0.43 μm, with 47 z-slices collected in total.

The 1st and the 47th slices represented the images taken at the top and bottom glass surfaces of the two coverslips where the scattering was mainly produced. As a consideration of the non-uniformity on the illumination field, 10 spots (10 ×10 pixels) outside particles were randomly selected throughout the two images respectively to make

the estimation of scattering signal originated from the surroundings of particles. The overall intensities of scattering from these two images were indicated as the average of the 10 spots on each slice. The scattering intensity measured at the glass surface of the bottom coverslip (1st image slice) was about 33.5 and that measured at the top coverslip (47th image slice) was about 36.5. Therefore, the overall scattering from the surrounding environments was approximated by averaging these two values and turned out to be 35. The expression of ΔG was corrected as:

$$\Delta G = -RTlnK_c = -RTln(\frac{I_{readout\ in\ particle}-35}{I_{readout\ outside\ particle}-35}) \quad [6.10].$$

6.3.6.2. Effect of intensity fluctuation on illumination plane on particle analysis

As discovered in system calibration studies, there was a patterned intensity illumination field in confocal imaging where the intensity was slightly higher at the center region while dropping off towards the edges. Even though this intensity change did not seem to be significant (~ 2%), we tested its effect on the free energy analysis.

A 20 ×20-pixel area outside particles was randomly selected from the original image to determine the overall average intensity of background $I_{backgound\ (overall)}$ which was 301.5 and had an $RSD_{background\ (overall)}$ of 23.34%. Then, 22 out of 99 particles were randomly chosen from the reconstructed images and their average intensities (*Ave.I*) were calculated individually (Table 6.5). First of all, the average ΔG of each particle was evaluated from $I_{backgound\ (overall)}$ and *Ave.I* of each particle using Eq. [6.10]. The calculated results were also listed in Table 6.5 and denoted as $\Delta G_{(overall).}$ To achieve a more precise measurement of ΔG, as an alternative to applying $I_{backgound\ (overall)}$, the background intensity was respectively estimated for each particle by calculating average intensity of a

20×20-pixel solution area right next to each particle. The average background intensities specifically associating with these 22 selected particles were also summarized in the same table and symbolized as $I_{background\ (local)}$. By substituting *Ave.I* of each particle and the corresponding $I_{background\ (local)}$ into [6.10], the average ΔG of particle ($\Delta G_{(local)}$) was more accurately estimated.

The effect of the intensity non-uniformity of the illumination field on the particle analysis was assessed by calculating the *% difference* between $\Delta G_{(overall)}$ and $\Delta G_{(local)}$ for each particle. Based on the results in Table 6.5, this effect is negligible as it only generates less than 2% error in ΔG measurements. In other words, it is reasonable to apply the overall average intensity of background $I_{backgound\ (overall)}$ for the evaluation of ΔG in different particles in the image. This realization simplifies the analysis tremendously as for some particles, it is difficult to identify an adjacent region in the image that is composed of solution only and there is no out-of-focus contribution from the particle fluorescence.

6.3.6.3. Construction of ΔG distributions inside particles

The signal fluctuation or noise in intensity inside particles needs to be estimated ahead of the investigation on ΔG distributions inside particles. As discussed above, the $RSD_{background\ (overall)}$ which indicated the measurement error in the background solution was determined to be about 23.3%. It was comparable to that measured on the home-built imaging system in preliminary studies. Noise was the predominant contributor to this intensity fluctuation. We characterized the intensity fluctuations or the noise level in the images. The width of the noise distribution will ultimately set the threshold for the smallest range of heterogeneity that can be determined in image analysis. The image

intensities for system calibration (section 6.3.3.1) provide an excellent data set for this evaluation. As demonstrated in Table 6.3, as the solution concentration increases, the average intensity increases while the *RSD* is reduced. The reciprocal of the square root of average intensity ($1/\sqrt{ave.I}$) was calculated at each concentration and shown in the table. Figure 6.14 manifests a good linear relationship between $1/\sqrt{ave.I}$ and *RSD* with R^2 = 0.999. It follows that:

$$RSD \propto \frac{1}{\sqrt{ave.I}}$$

Which leads to

$$\frac{SD}{ave.I} \propto \frac{1}{\sqrt{ave.I}}$$

and thus

$$SD \propto \sqrt{ave.I}$$

In this concentration variation experiment, the *SD* of measurements was proportional to the square root of the average intensity in the image.

With the acknowledgement of the relationship between *SD* of measurement and $\sqrt{ave.I}$, the measurement error of particles ($RSD_{particle}$) was then estimated by the error in the background solution outside of the particles ($RSD_{background\ (overall)}$). According to the results from the preliminary studies, the average equilibrium constant K_c of the particles was about 14. Therefore, the measured fluorescence intensity of particles is 14 times higher than that of background solutions on average:

$$\frac{I_{particle}}{I_{background}} = 14 \quad [6.12],$$

and the measurement error of particles $RSD_{particle}$ is then calculated as:

$$RSD_{particle} = \frac{SD_{particle}}{I_{particle}} = \frac{\sqrt{I_{particle}}}{I_{particle}} = \frac{\sqrt{14I_{background}}}{14I_{background}} = \frac{\sqrt{I_{background}}}{\sqrt{14}I_{background}} = \frac{SD_{background}}{\sqrt{14}I_{background}} =$$

$$\frac{1}{\sqrt{14}}RSD_{backgound} = \frac{1}{\sqrt{14}} \times 23.3\% = 6.2\% \quad [6.13].$$

It indicates that the noise produced during the imaging process will give rise to a 6.2% of relative error or fluctuation in image intensity inside particles.

Subsequently, the intra-particle (pixel-by-pixel) and global Δ*G* distributions were investigated by computing Δ*G* values for all 99 particles in Figure 6.9 and the results are summarized in Table 6.6. The data provided in Table 6.6 demonstrated several important facts that (1) there is clearly a heterogeneity in Δ*G* within individual particles. It is evidenced by the fact that the minimum *RSD* in intensity for individual particle is about 7.2% and greater than expected measurement error of ($RSD_{particle}$) 6.2%; (2) the level of heterogeneity in fluorescence intensity within individual particles varies significantly from 7.2% to 52.8%. In other words, the intra-particle Δ*G* distribution of each particle is remarkably different; and (3) the Δ*G* heterogeneity in all selected pixels of the 99 particles, the global Δ*G* distribution, exists as evidenced by the large *RSD* of fluorescence intensities (~14.4%) and it corresponds to the RSD of Δ*G* of ~5.4%.

The intra-particle Δ*G* distribution of a representative particle as well as the global Δ*G* distribution, which included *ΔG* at each selected pixels of 99 particles in the images were constructed and shown in Figure 6.15A and B. The two distributions were well fitted by Gaussian curves indicating a random distribution of the interaction energies for the solute at the C18 interface on the nanopore surface. Figure 6.15A shows a global

particle ΔG distribution ranging from ~ – 5.0 k*J/mol* to ~ – 8.0 k*J/mol* with a peak width (*FWHM*) of ~ 0.8 *kJ/mol*. Figure 6.15B presents a narrower intra-particle ΔG distribution of a randomly-selected particle, ranging from about – 6.0 k*J/mol* to – 7.3 k*J/mol* with a peak width of ~ 0.4 k*J/mol*. In order to achieve direct observation of the ΔG heterogeneity of the particles, ΔG distributions of particles were mapped and presented in Figure 6.16 A, B, C and D (corresponding to the original confocal images in Figure 6.9 A, B, C and D).

6.4. Conclusions

In this chapter, we demonstrated the existence of heterogeneity in ΔG of the nanoporous C_{18}-derivatized silica particles in a unique and straightforward way by employing confocal fluorescence imaging. The theoretical core of this method is the equilibrium of the target fluorescent molecule – Rhomdamine 6G between the nanoporous particle interface and the solvent acetonitrile. With the derived conceptual framework, the equilibrium constant K and the corresponding ΔG of each particle was individually estimated from the intensity-based fluorescent confocal images of the particles.

We firstly tested the feasibility of the initial conceptual idea with our home-built stage-scanning confocal microscopy system to build up the framework of this study and then employed the commercial Zeiss LSM710 laser scanning confocal imaging system to perform a series of investigations on the ΔG distribution of nanoporous silica particles. After a careful and thorough system calibration and validations, the confocal images of the particles were analyzed. From the analysis results, we confirmed the existence of a

fairly significant ΔG distribution among all sampled particles as well as the ΔG heterogeneity within individual particles.

Table 6. 1 Investigation of uniformity of intensity across the illumination field and the stability of the home-built stage-scanning confocal microscopy system

Region Number	Average intensity (*counts/ 1ms*)	Standard deviation of intensity (*counts/ 1ms*)	RSD_{in} (%)
1	35.3	9.9	27.9
2	39.2	7.0	17.9
3	40.2	10.2	25.3
4	37.4	8.9	23.7
5	35.9	8.5	23.5
6	31.9	6.8	21.2
7	30.7	7.3	23.6
8	35.7	8.7	24.3
9	34.5	7.5	21.7
10	37.7	9.4	25.0
11	38.7	10.0	25.8
12	41.2	8.7	21.2
Global	36.5	3.2	8.7

Table 6. 2 Effects of scattering signal on the ΔG analysis of particles by using home-built stage-scanning confocal microscopy system

	Without correction of solvent scattering	With correction of solvent scattering
Average intensity (*counts/ 1ms*)	204.8	204.8
Standard deviation of intensity (*counts/ 1ms*)	76.8	76.8
RSD of intensity (%)	37.5	37.5
Average ΔG (*J/ mol*)	-4067.2	-6894.4
Standard deviation of ΔG (*J/ mol*)	937.8	1113.5
RSD of ΔG (%)	23.1	16.2

Table 6. 3 Calibration studies of Zeiss LSM710 confocal microscope system

Solution concentration (μM)	Average intensity ($a.u$)	Standard deviation of intensity ($a.u$)	RSD of intensity (%)	$\frac{1}{\sqrt{Ave.intensity}}$
3.3	4.5	1.5	33.2	0.47
6.6	9.2	2.1	22.5	0.33
9.9	11.9	2.4	19.8	0.29
13.2	16.7	2.8	16.7	0.24
16.4	23.1	3.3	14.1	0.21
47.6	50.5	4.7	9.4	0.14
76.9	68.0	5.2	8.8	0.12
104.5	97.5	6.8	7.0	0.10
142.9	136.9	7.9	5.8	0.09
200.0	198.5	9.7	4.9	0.07
250.0	245.0	8.8	3.6	0.06

Table 6. 4 Test of the uniformity of intensity on the illumination field

Solution concentration (μM)	Average intensity ($a.u$)	Minimum intensity ($a.u$)	Maximum intensity ($a.u$)	*RSD* of average intensities of 16 sub-images (%)
3.3	4.4	4.2	4.5	2.1
6.6	9.1	8.8	9.4	2.0
9.9	12.0	11.5	12.4	2.2
13.2	16.3	15.8	16.7	1.9
16.4	19.2	16.2	21.3	5.2
47.6	49.4	47.4	50.9	2.3
76.9	68.0	65.9	69.7	1.7
104.5	95.7	92.1	98.3	1.9
142.9	134.1	128.7	138.0	1.9
200.0	197.8	188.5	203.5	2.0
250.0	244.0	236.7	249.1	1.6

Table 6. 5 Effect of non-uniformity of illumination field on ΔG analysis of particles

Particle number	Average intensity of particles ($a.u$)	Average $\Delta G_{(overall)}$ of particles ($J/\ mole$)	$I_{background\ (local)}$ ($a.u$)	Average $\Delta G_{(local)}$ of particles ($J/\ mole$)	*% difference* (%)
1	4110.3	-6757.2	298.5	-6784.8	0.41
2	4147.6	-6779.7	279.3	-6994.9	3.08
3	4258.4	-6845.6	307.1	-6793.8	0.76
4	4512.6	-6990.4	299.8	-7006.6	0.23
5	3922.5	-6640.3	304.3	-6614.9	0.38
6	4528.9	-6999.4	307.3	-6946.2	0.77
7	4077.3	-6737.0	321.1	-6560.9	2.68
8	3640.6	-6453.8	304.8	-6423.3	0.47
9	4208.5	-6816.1	311.5	-6725.0	1.36
10	3923.7	-6641.0	310.2	-6561.7	1.21
11	4818.9	-7154.3	322.8	-6964.0	2.73
12	3801.5	-6561.9	305.0	-6529.9	0.49
13	4432.1	-6945.5	303.5	-6927.0	0.27
14	4188.4	-6804.2	319.4	-6642.9	2.43
15	3905.8	-6629.6	315.9	-6499.2	2.01
16	4689.0	-7086.1	317.6	-6940.6	2.10
17	3340.0	-6238.1	310.7	-6153.6	1.37
18	3781.1	-6548.5	317.9	-6400.2	2.32
19	4115.1	-6760.1	308.2	-6698.3	0.92
20	4000.7	-6689.6	313.8	-6577.6	1.70
21	3715.3	-6504.6	316.2	-6371.2	2.09
22	3779.6	-6547.5	308.3	-6484.8	0.97

Table 6. 6 Summaries of ΔG distributions of C18-derivatized nanoporous silica particles

	Intra-particle heterogeneity in *ΔG*
Maximum RSD of intensity of individual particle (%)	52.8
Minimum RSD of intensity of individual particle (%)	7.2
	Global heterogeneity in *ΔG*
Average intensity of all particles	4159.0
RSD of the average intensities of all particles (%)	14.4
Average *ΔG* of all particles (*J/ mole*)	-6759.9
RSD of *ΔG* of all particles (*%*)	5.4

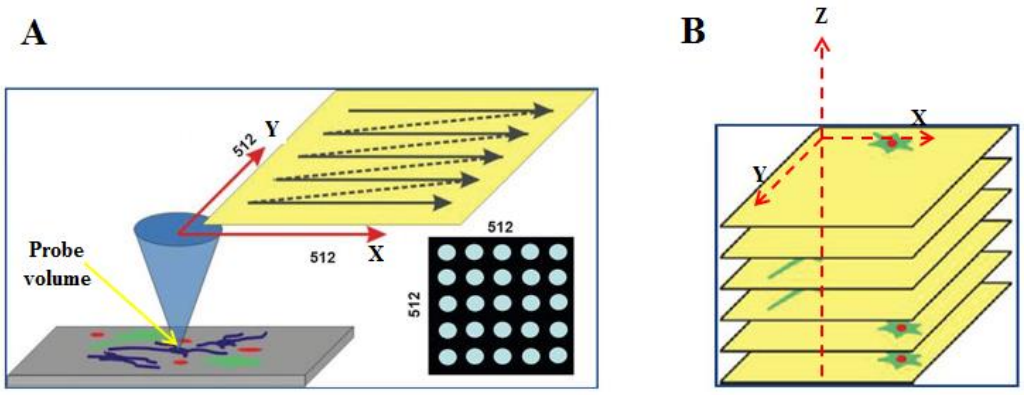

Figure 6. 1 Principles of image formation in confocal microscopy imaging

---

Note: (A) Formation of two-dimensional image in confocal microscopy. The 2-D image is constructed by point-by-point scanning along a line and line-by-line scanning following a zigzag route of the probe volume. The lower right corner represents an image composing 512 ×512 digital pixels; (B) Formation of 3-D image. The 3-D image is achieved by stacking 2-D images taken at different image planes of Z-axis together.

Source: http://www.gum2012.fionastoreydesign.co.uk/confocal_microscopy.html.

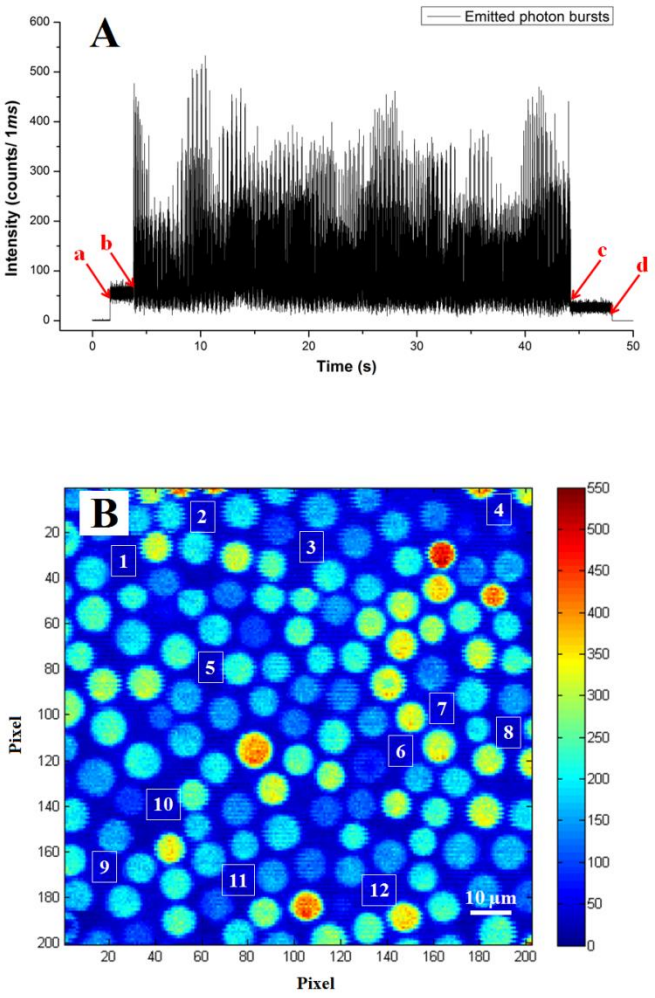

Figure 6. 2 Image construction of home-built stage-scanning confocal microscope

---

Note: (A) The raw data (time-dependent photon counts) collected from detector. a: the time of opening shutter of detection channel, b: the time of starting the scanning of sample stage, c: the time that stage-scanning stops, d: the time of closing the shutter and stopping data collection; (B) The constructed image composed by 201 ×201 pixels. The labels of 1 to 12 indicate the general locations for background analysis.

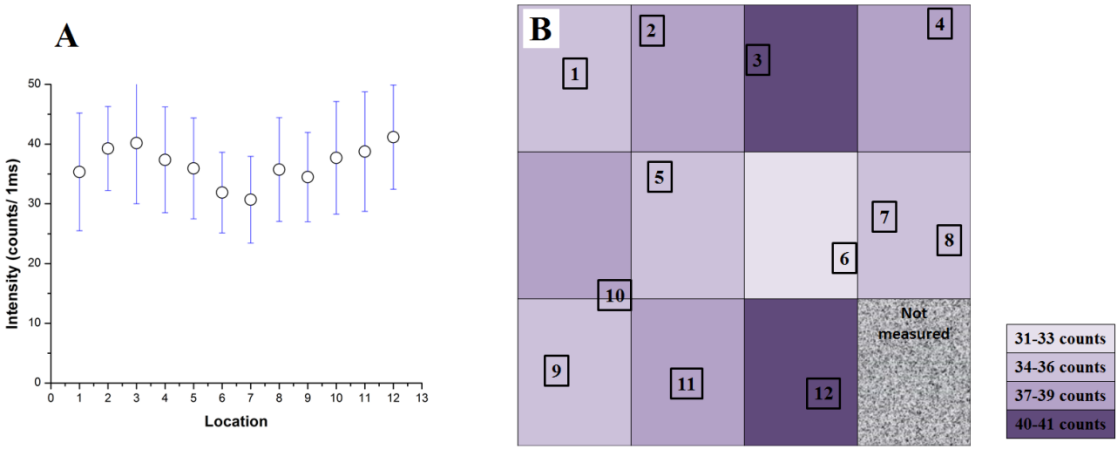

Figure 6. 3 Investigation of illumination field uniformity and stability of the home-built stage-scanning confocal microscope system

---

Note: (A) The average intensity of solution (outside particle) at selected locations; (B) Random fluctuation of intensity shown on image plane: demonstrates that there is no intensity drift pattern on the illumination field.

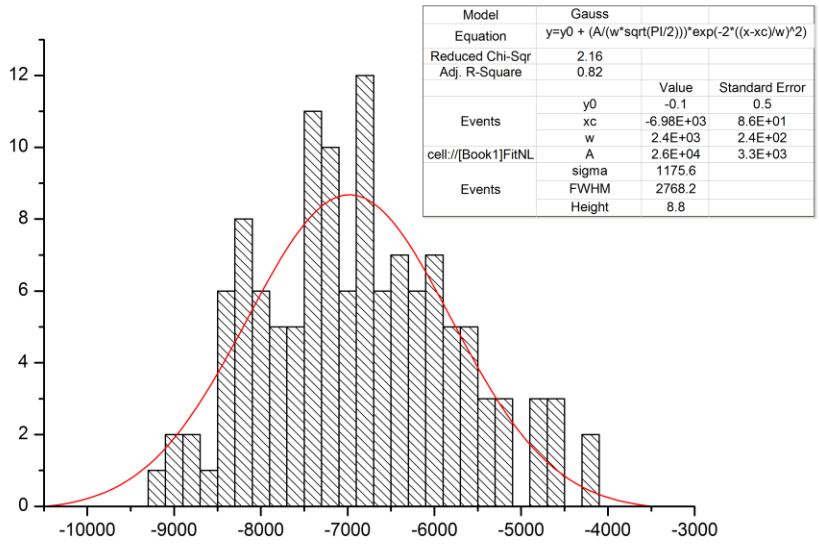

Figure 6. 4 Distribution of ΔG for all 125 particles in Figure 6.2B

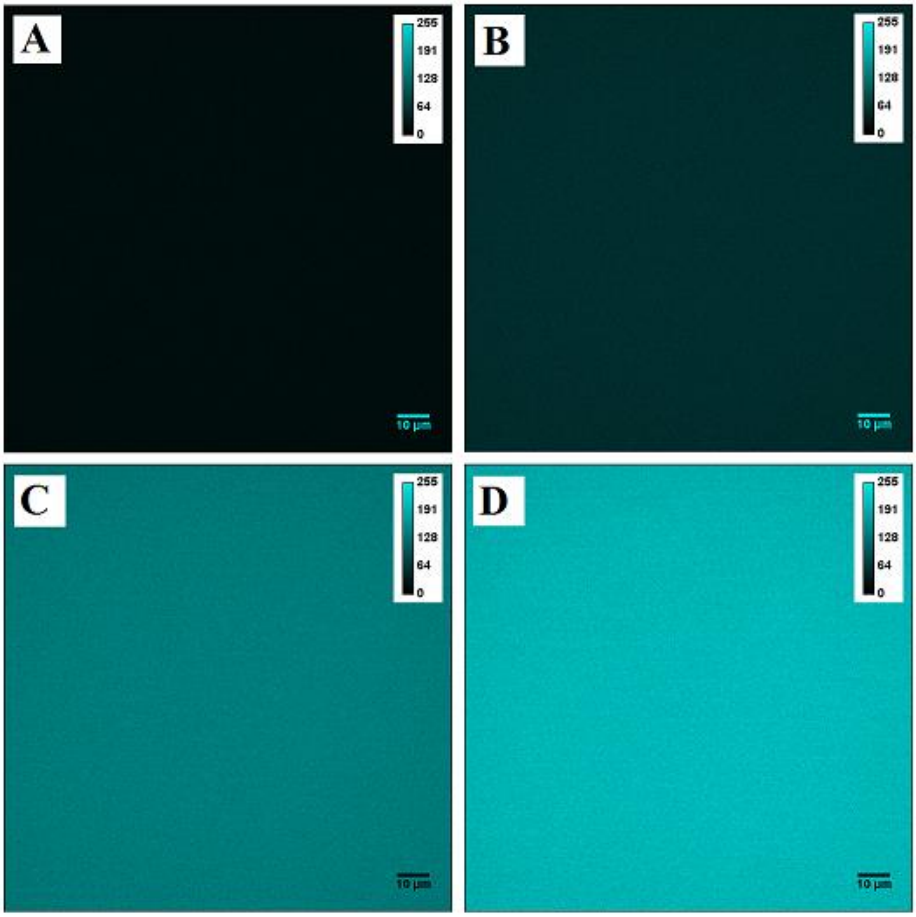

Figure 6. 5 Images (8-bit) of standard solutions at several representative concentrations for imaging system calibration

---

Note: Images of solutions with concentrations of 13.2 μM (A), 47.6 μM (B), 142.9 μM (C) and 200.0 μM (D), respectively.

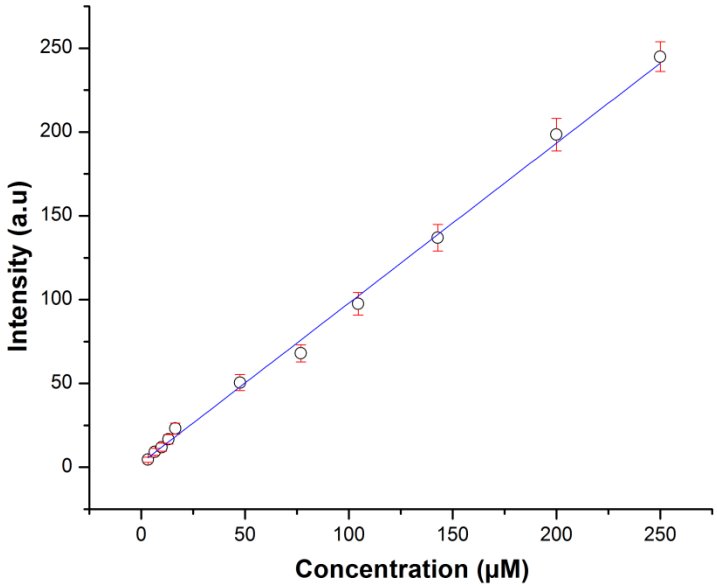

Figure 6. 6 Intensity calibration for Zeiss LSM710 confocal microscope system

---

Note: The fitting line has a R^2 = 0.995, slope of 0.95±0.02 and 2.52±0.89.

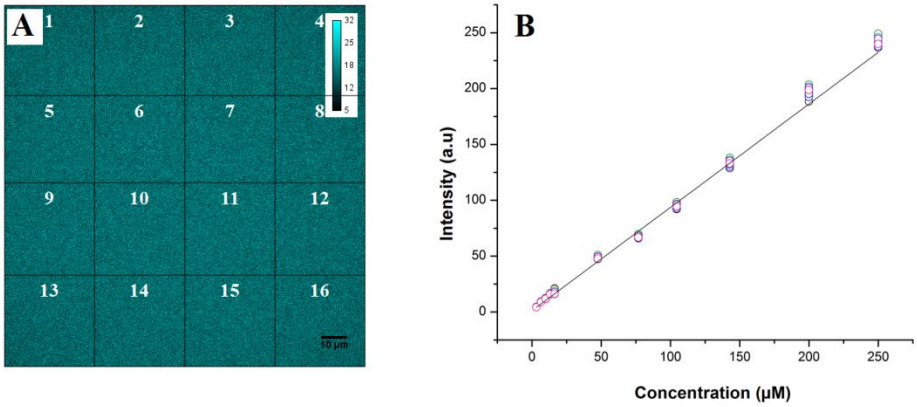

Figure 6. 7 Investigation of robustness of the imaging system

---

Note: (A) Division of solution (13.2 μM) image into 16 sub-images and the corresponding section numbers; (B) Calibration curve that incorporates the average intensities of all 16 sub-images of each standard solution. The fitting line has a R^2 = 0.998, slope of 0.93±0.01 and intercept of 1.16±1.65.

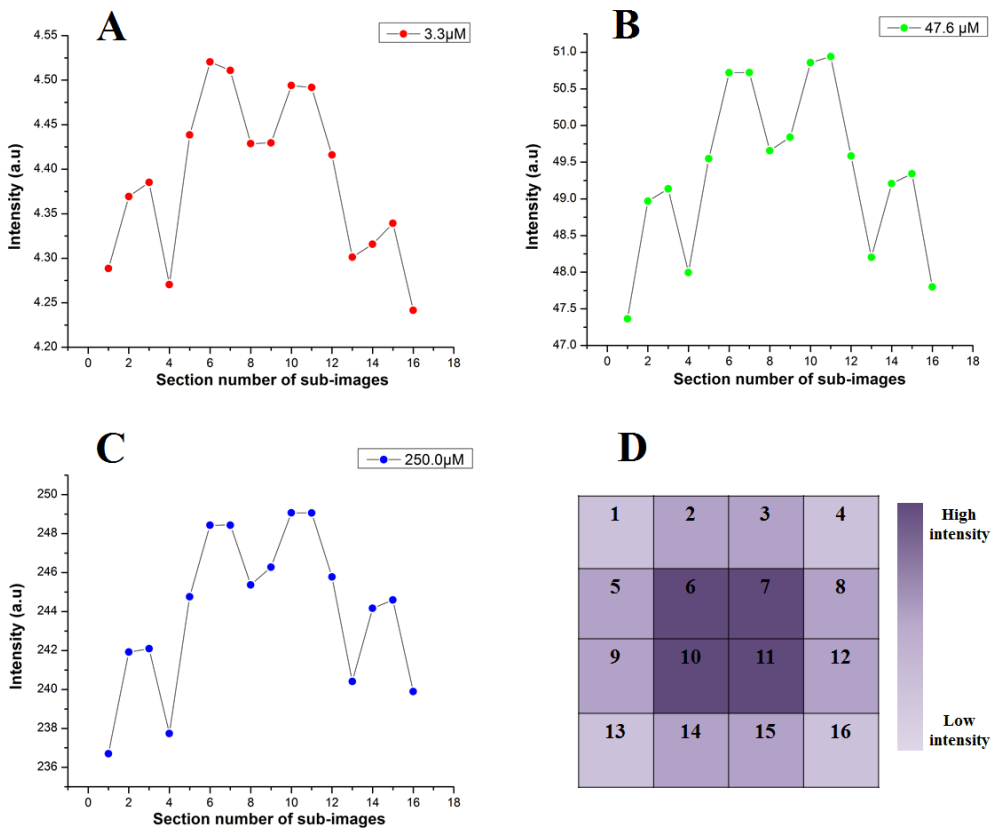

Figure 6. 8 Intensity uniformity on the illumination field of imaging system

---

Note: Average intensities of all 16 sub-images of representative standard solutions with concentrations of 3.3 μM (A), 47.6 μM (B) and 250.0 μM (C); (D): Patterned non-uniformity on the illumination field. The intensity appears to be highest at the center while lowest at the corners.

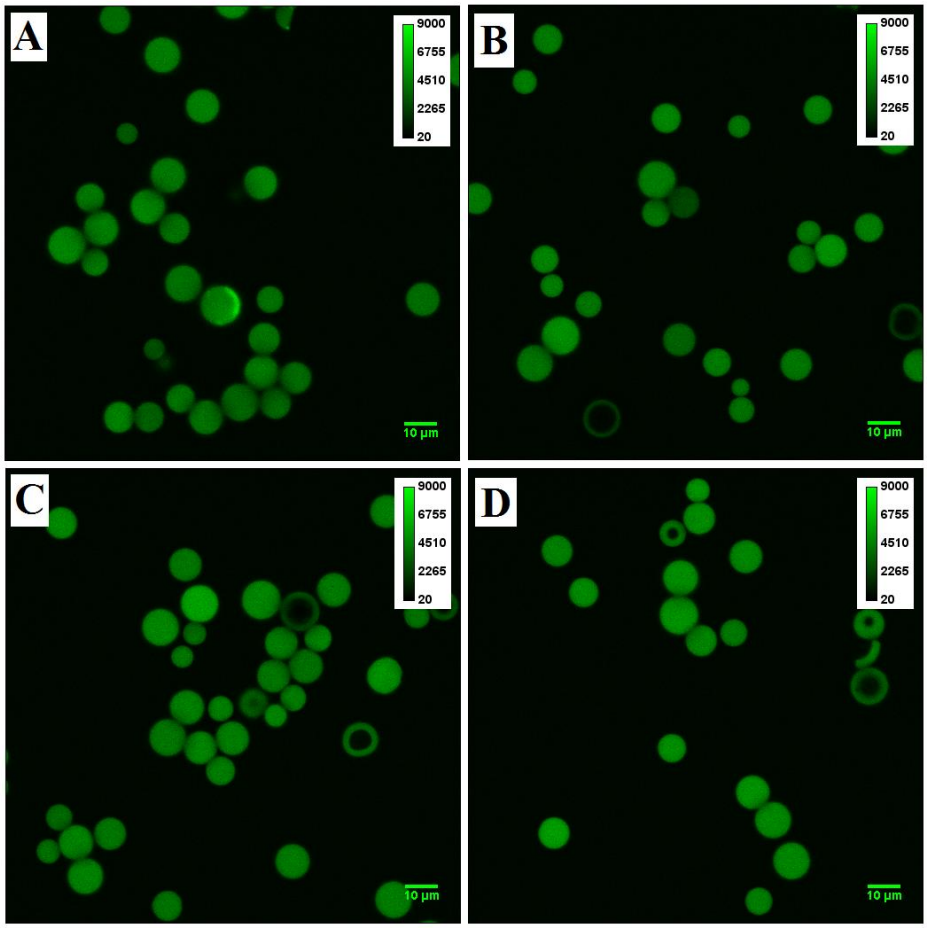

Figure 6. 9 Confocal fluorescence images (16-bit) of C_{18}-derivatized silica nanoporous silica equilibrated with 10 μM R6G/acetonitrile solution

---

Note: The images were taken at different locations of a single sample slide under the same condition and settings of the imaging system.

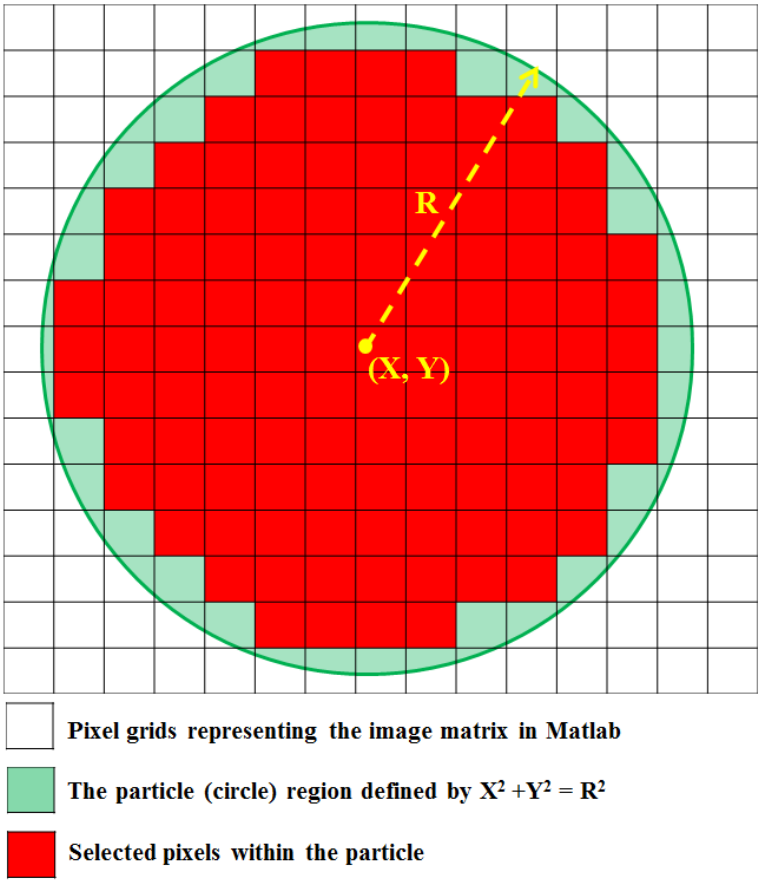

Figure 6. 10 The method of pixel selection for particle analysis of the fluorescence confocal images

---

Note: This is a simplified presentation of pixel selection method. In practice, ~1135 pixels ($Pixel\ number\ = \pi \times \left(\frac{10\ \mu m}{0.26\ \mu m}\right)^2$) can be selected (shown as red) from each particle on average.

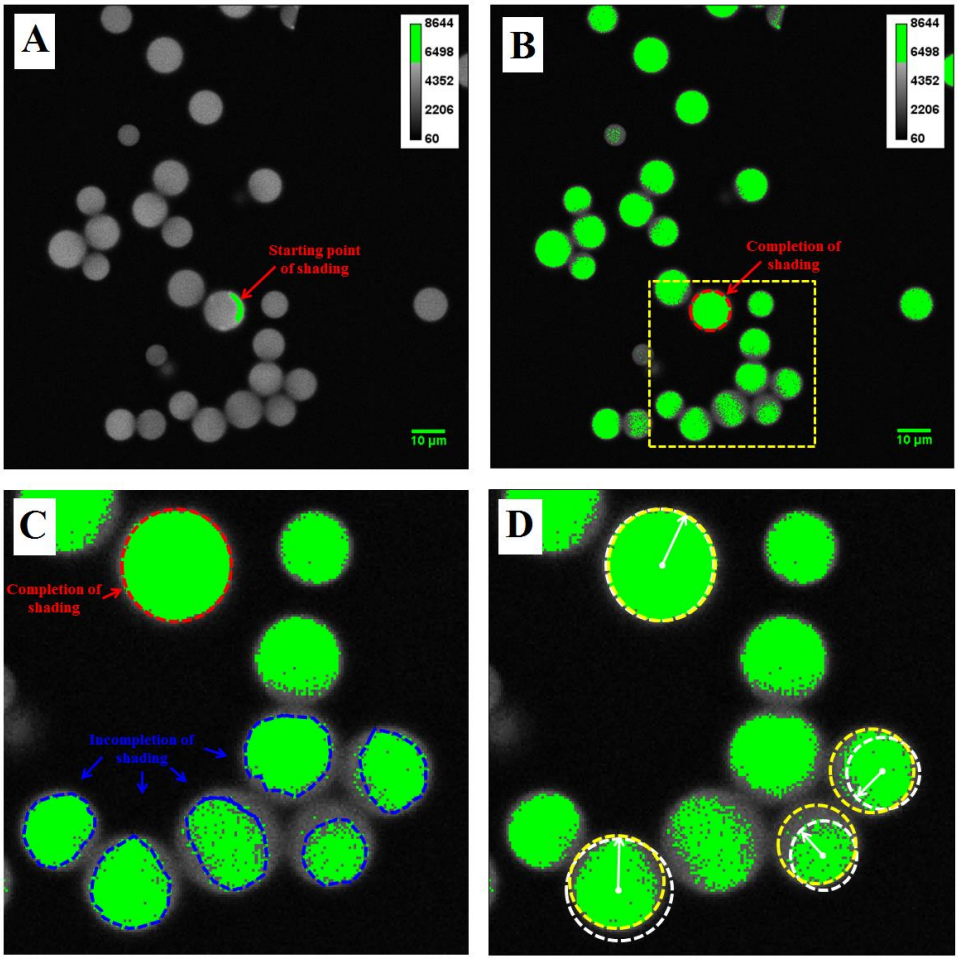

Figure 6. 11 Issues in the procedure of manual thresholding for pixel selection with ImageJ

Note: (A) The starting point of manual thresholding of the image; (B) The ending point of thresholding process as the completion of shading the area of particle with highest average intensity, denoted by red dashed circle; (C) Zoom-in of the area indicated in (B) to specifically show the shaded areas with skewed shapes (emphasized by blue dash lines) of particles with lower intensities at the ending point of thresholding; (D) The offset in the results of pixel selections in ImageJ. Yellow dashed circles: the actual location and size of particles, white dashed circles: the areas selected by ImageJ.

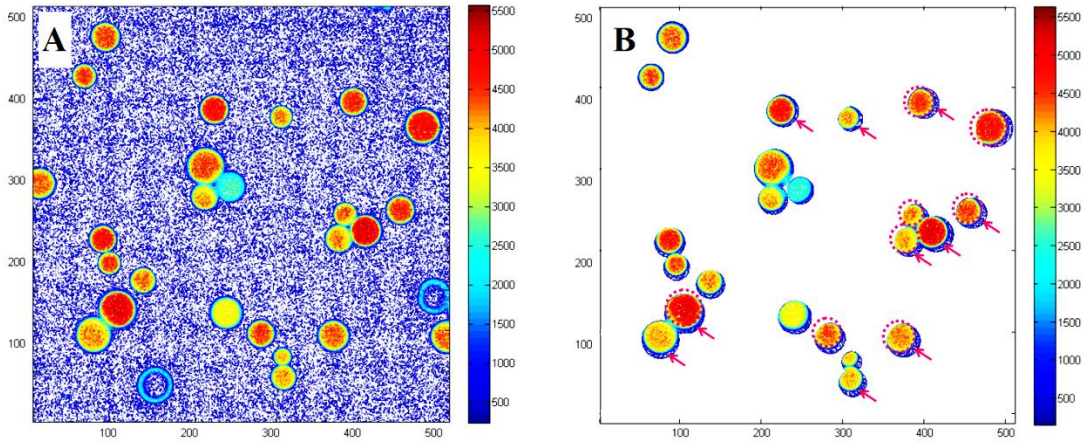

Figure 6. 12 Pixel selection and image reconstruction in Matlab when applying manual thresholding

---

Note: (A) The original image of particles (Figure 6.9B); (B) The reconstructed image of the same particles after pixel selection with inaccurate coordinates (*X*, *Y*) and *R* of particles. Background (unselected region) is defaulted as 1 (white out) for clearity of presentation of the drifts of the reconstructed particles. For some particles, solution is mistakenly included as parts of the particles, as indicated by the arrows. Some areas belonging to particles are excluded and the dash circles show the shapes of actually particles.

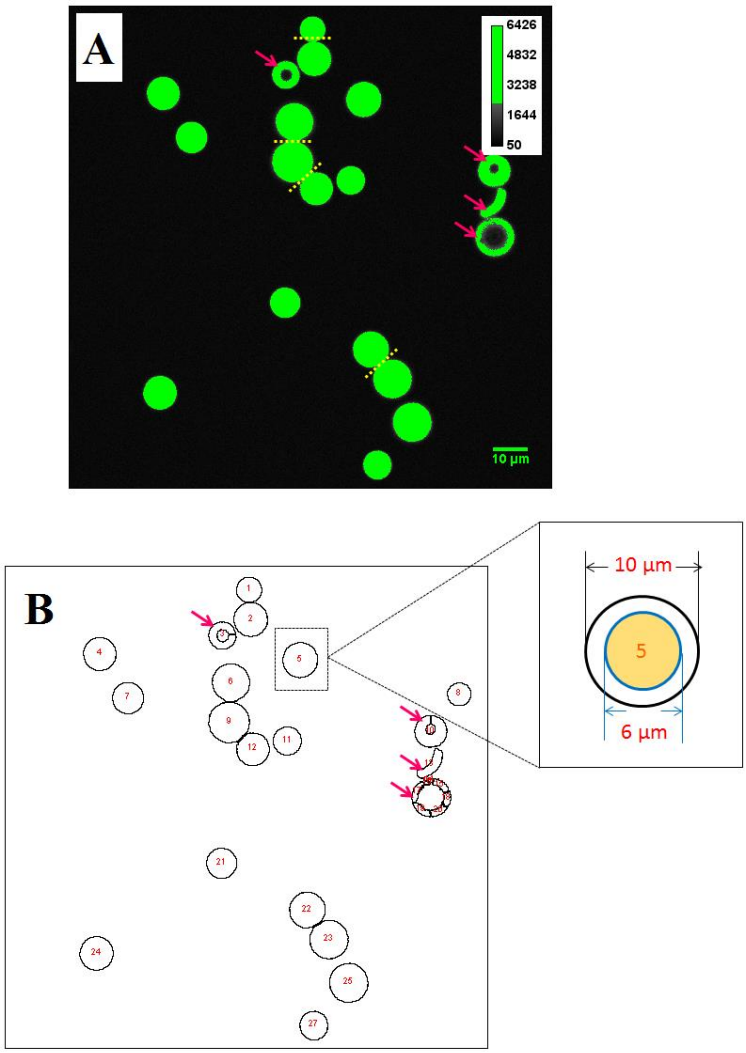

Figure 6. 13 Automatic thresholding for pixel selection in ImageJ

Note: (A) The automatic thresholding of the image of particles (Figure 6.9D). "Watershed" was applied for cutting edges of the touching particles, as indicated by the yellow dash lines. The "core-shell" particles as well as broken fragments of particles (indicated by arrows) were excluded; (B) Circles (shaded areas) generated in ImageJ. They are defined by coordinates of the center (X_a, Y_a) and the radius R_a determined by auto-thresholding process. The zoom-in shows the example of pixel selection of particle in Matlab: a circled area (yellow shaded area) defined by (X_a, Y_a) and (R_a-*2*) was selected for image reconstruction in Matlab.

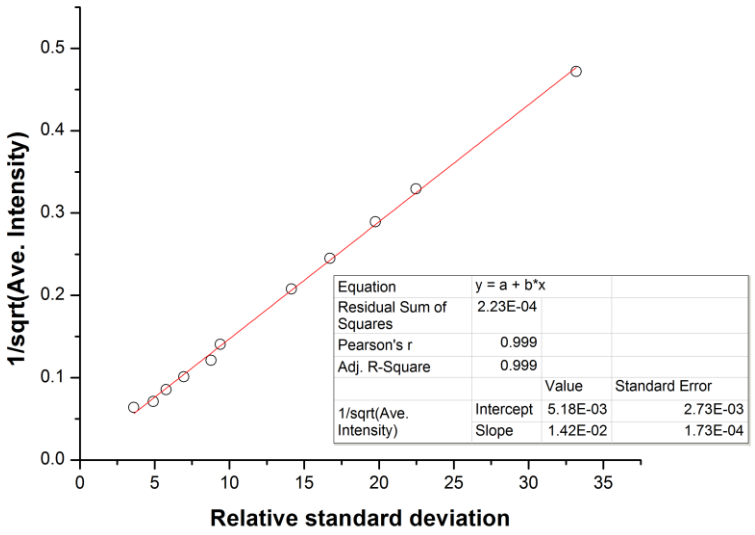

Figure 6. 14 The studies of noise in quantitative confocal imaging

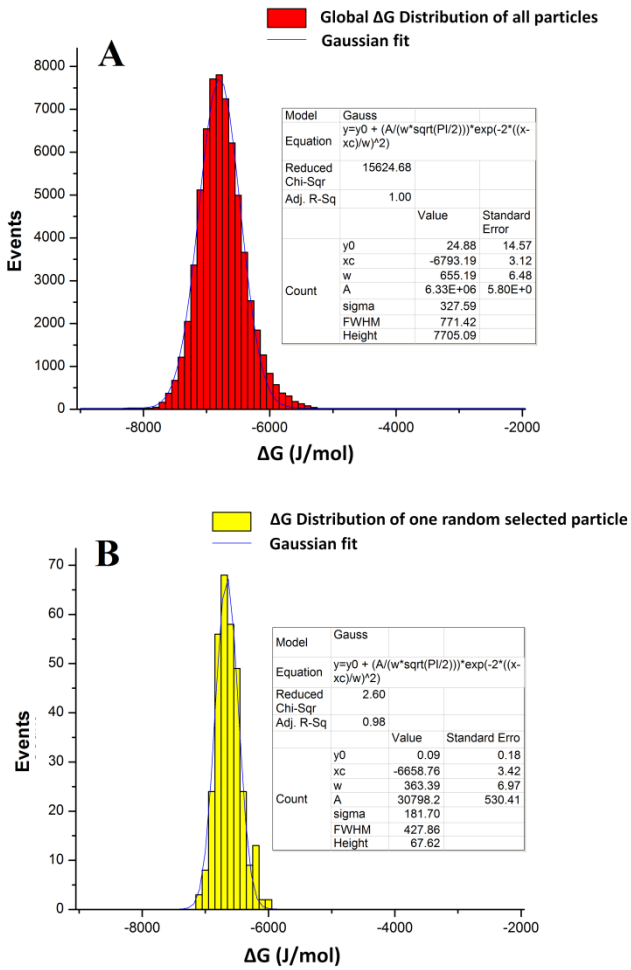

Figure 6. 15 ΔG distributions of C_{18}-derivatized nanoporous silica particles

---

Note: (A) Global ΔG distribution which includes individual ΔGs at all the selected pixels of all 99 particles; (B) ΔG distribution of one randomly selected particle.

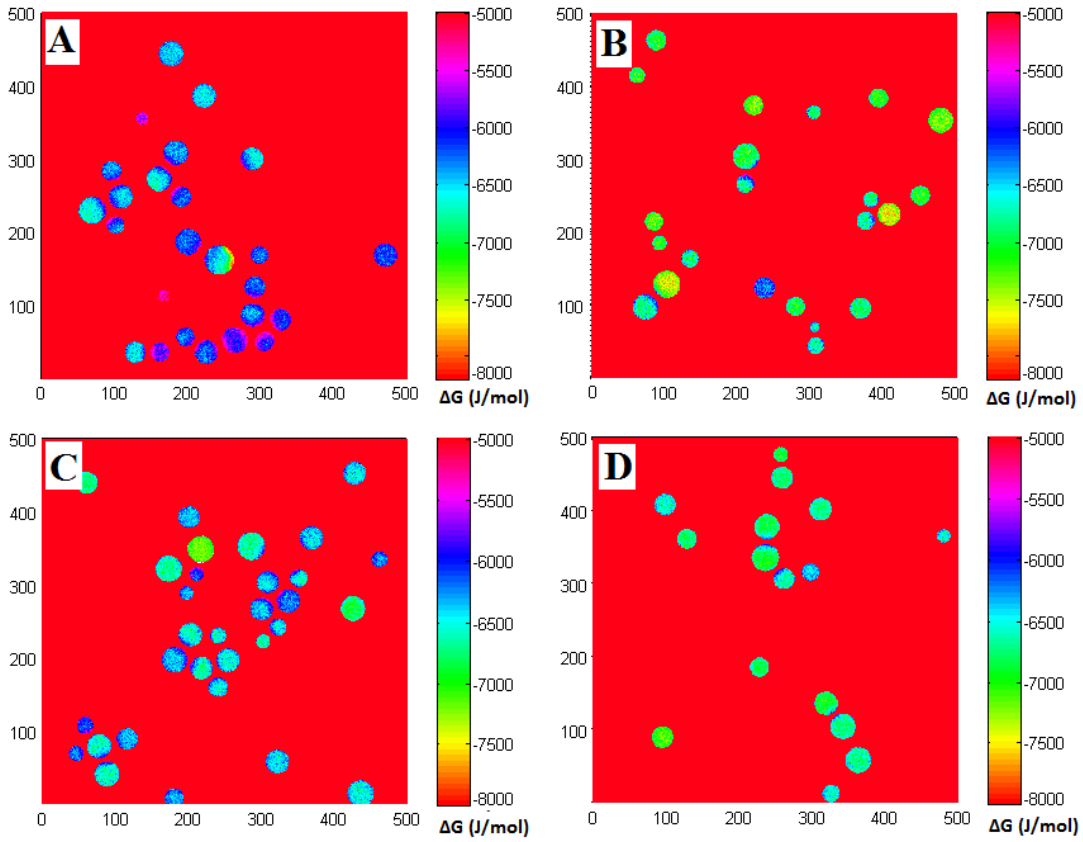

Figure 6. 16 ΔG maps of the particles shown in Figure 6.9

CHAPTER 7

BILE SALTS ASSISTED SOLUBILIZATION OF HYDROPHOBIC NANOPOROUS SILICA PARTICLES

7.1. Introduction

The studies of controlled drug delivery have been facilitated in recent years by the rapid advances in materials science [231]. The goal of controlled drug delivery is to efficiently and accurately transport and release certain amount of drug molecules to specific target sites in human body without decomposition of and the loss of the therapeutic functions of drug molecules. It makes the choice of devices or drug carriers very demanding. A large group of nanoporous materials have been explored as promising candidates of drug delivery vehicles, including porous silicon (Si), aluminum oxide (Al_2O_3), titanium oxide (TiO_2) and mesoporous silica (SiO_2) [232-238]. The nanoporous materials are a type of solid material permeated by a network of connected nanopores. They have a number of outstanding properties that make them popular in the applications of drug delivery, including large surface area to volume ratio, high thermal and chemical stability as well as the flexibility of surface modification[239].

Porous silicon (Si) is one of the most extensively researched materials for developing drug delivery systems with high performance because of its easily tunable morphology and size of pores and low toxicity. Porous Si can be used as carrier of various types of drug molecules, such as proteins, DNAs and enzymes. The loading of drug molecules into the porous structure of this material is often achieved through physical adsorption, trapping and covalent attachment [237]. Its success as the host of

ibuprofen [240], doxorubicin [241] and some other drugs in the applications of controlled drug release has been reported. One most advanced study is to utilize porous Si particles with average diameter of 20 μm as the brachytherapy device for cancer treatment in *vivo*. The drug—radioactive isotope ^{32}P was directly synthesized on the surface of porous silicon particle and then released to specific locations of tumor for radiation [242, 243]. Besides the porous Si, other nanoporous materials have also been employed as the devices in the sustained drug release studies. For example, nanoporous Al_2O_3 is usually developed into the form of capsule to improve its mechanical strength as the vehicle of drug delivery [244]. La Flamme et al. reported a study of loading and transporting glucose, insulin and immunoglobulin G (IgG) for the treatment of diabetes in *vitro* [235]. Popat and co-workers employed TiO_2 nanotubes as drug carrier to treat chronic infection which arises as side-effect after orthopedic implant surgeries. They developed a system to achieve a controlled release of antibiotics from TiO_2 nanotubes to infection sites in the bone tissue. [245]

In recent years, nanoporous silica material has gained its popularity in the applications of drug delivery because of its non-invasiveness, low toxicity, biocompatibility and easy synthesis. The majority of silica-based drug delivery systems are developed by using underivatized nanoporous silica which is hydrophilic in physiological environment where pH is ~ 7.4 and the silanol groups are deprotonated. A central challenge is to efficiently trap drug molecules inside the pores during transport and minimize the leakage. Several approaches were developed to conquer these challenges. Martin group, for instance, applied hollow silica nanotubes with one end closed as drug carrier. After drug loading, they corked the other end of nanotubes with

chemical self-assembled nanoparticles. Imine linkages were attached to several spots between nanotubes and nanoparticles for system stabilization [246]. A method of mechanical capsulation of silica nanotubes was developed by Yu and co-workers. They deposited a thin layer of capping material (Au, Ag) on the surface of open end of nanotubes and hammered it with alumina microbeads for sealing [247]. Zink group created a drug delivery system by applying the pH driven molecular nanopistons at the entrances of nanopores of nanoporous silica particles to achieve efficient trapping and controlled release of guest molecules by operating the pH [248].

All these systems involve complex synthetic or nanofabrication steps to generate a physical cap to block the pore openings. Alternatively, our research group is conducting research of using hydrophobic silica nanoporous particles as the vehicles of drug molecules. The100% efficiency of drug loading and releasing are successfully achieved with open-pore configuration, without any chemical and/or physical modification of the particles. The controlled drug released is also accomplished by switching solvent from water to ethanol where the hydrophobic particles can be wetted [249]. A major challenge in this application is to disperse these hydrophobic drug delivery vehicles in the physiological aqueous phase. In other words, a requirement in this system is to make the hydrophobic particles "soluble" in water. The drug delivery cannot be achieved without the solubilization of the particles since the hydrophobic interactions between particles will makes them clustered together.

Surfactant —sodium dodecyl sulfate (SDS) was explored to assist the particle solubilization in the aqueous phase. The nonpolar tails of SDS molecules are self-organized into the C_{18} chains of particles driven by hydrophobic interaction. The

negatively charged head groups extend out of the hydrocarbon layer and are exposed to the aqueous solution. This renders particles soluble and well-dispersed in water [249, 250]. The experiments on SDS micelles were designed to test the general principle of using surfactants to facilitate the solubilization of hydrophobic particles. However, considering biocompatibility, the SDS-assisted solubilization of the particles is not a choice in *in vivo* studies of drug delivery. SDS molecules can lead to denaturation of proteins by adding extra negative charges to the amino acids which straighten out proteins due to the charge repulsion. In addition, the anionic surfactant molecules can disrupt the interaction between native proteins embedded in cell membranes and therefore destroy the bi-layer structure of membranes.

An alternative system of using bio-compatible surfactant, bile salt, to assist the solubilization of hydrophobic particles was then developed and the preliminary studies are reported in this chapter. Bile salts are organic solutes that naturally exist in bile and participate in the enterohepatic circulation in human body [251]. As the derivatives of cholesterol, the bile acids are synthesized in the hepatocyte (liver cells) and then conjugated to glycine or taurine to form conjugated bile acids, bile salts. Based on the combination between bile acid and amino acids, there are typically 4 types of bile salts—cholate, deoxycholate, glycocholate and taurocholate [252]. Sodium deoxycholate (NaDC) was employed in this preliminary study and its chemical structure is shown in Figure 7.1. All bile salts are naturally amphipathic and thus can form micelles when the concentration is above critical micelle concentration (CMC). For NaDC, specifically, micelles with aggregation number of ~ 5 can be formed when the concentration is above 6 mM (25 ^{o}C). This property determines two important functions of bile salts in human

body: (1) emulsification, which break downs fat globules into small drops through hydrophobic interaction between fat globule and hydrophobic surface of bile salt micelles (Figure 7.1) and (2) solubilization of lipids such as fatty acids and monoglycerides in aqueous phase by forming micelle-lipid constructs and make lipids suspend in water [253]. Inspired by the second function mentioned, we proposed an idea to solubilize the C_{18}-derivatized nanoporous silica in aqueous environment by introducing NaDC micelles into aqueous phase and forming NaDC micelle-C_{18} (particle) constructs in water. Similarly to the situation of lipid solubilization in human body, these hydrophobic drug carriers should be able to be solubilized and well dispersed in aqueous environments.

7.2. Experimental

7.2.1. Chemicals and materials

Kromasil C_{18}-, C_8- and C_4-derivatized nanoporous silica particles were purchased from Akzo Nobel EKA Chemicals (Bohus, Sweden). The fluorophore pyrene and the surfactant sodium deoxycholate (NaDC) were obtained from Sigma Aldrich (Milwaukee, WI) and used as received. The deionized water used in experiments was purified by a MilliQ system (MilliQ-Plus, Millipore, Bedford, MA). For the organic solvents employed in this study, 200 proof ethanol was purchased from Decon Laboratories, Inc., HPLC grade acetonitrile, methanol were from Fisher Scientific. ACS grade hexane and 2-propanol were also obtained Sigma Aldrich.

7.2.2. Instrumentation and measurements

7.2.2.1. Surfactant-assisted solubilization of hydrophobic nanoporous particles

First of all, NaDC aqueous solutions at various concentrations ranging from 0.6 *mM* to 300 *mM* were freshly prepared. The 1.00 μM pyrene/ NaDC aqueous solution was prepared at each concentration of NaDC aqueous solution. Then ~ 0.045 *g* of particles was weighted out and mixed into ~3*mL* of each prepared pyrene/NaDC s solution, followed by thorough handshaking of the mixtures for ~1min.

7.2.2.2. Quantitative fluorescence measurements of the solubilization of particles

The kinetics of NaDC-assisted solubilization of hydrophobic nanoporous silica particles was monitored by collecting fluorescence emission spectra of pyrene in a time period of 72 hours. All fluorescence measurements were performed by using AMINCO-Bowman Series2 Luminescence Spectrometer (Model: FA-354, Thermo Electron, Waltham, MA). The excitation wavelength of Xenon lamp was set to be 274 *nm* for pyrene excitation. The fluorescence spectra were recorded from 340 *nm* to 500 *nm*, with emission bandpass of 2 *nm*. The step size and spectrum scan rate were set to be 1 *nm* and 1 *nm/s*, respectively.

After mixing, the cuvette containing the sample mixture was immediately placed into the fluorescence spectrometer for spectral measurement. Three replicates of spectra were collected at each specified time point of 0 min, 30 min, 1 hour, 2 hours, 3 hours, 4 hours, 5 hours, 24 hours, 48 hours and 72 hours after mixing the particles into the surfactant aqueous solution. With an assumption that the system achieved equilibrium after 72 hours, at the end of this experiment, the cuvette was gently shaken again to re-

suspend all solubilized particles, including the particles floating on the top of solution and those sinking to the bottom of cuvette. Three replicates of fluorescence spectra of this re-mixed sample were acquired after the re-shaking procedure. Various sample mixtures with different combinations of solution concentration and hydrocarbon chain length of the hydrophobic nanoporous particles were measured under the same experimental set-up.

7.3. Results and Discussions

In this chapter, we report the preliminary studies of the bile salt-assisted solubilization of hydrophobic nanoporous silica particles, aiming to initiate the investigation on surfactant-assisted wetting and solubilization of hydrophobic nanoporous particles in biological compatible environment. This will lead to a progress in the development of hydrophobic nanoporous material as drug delivery vehicles in physiological environment.

7.3.1. Qualitative studies of NaDC-assited solubilization of hydrophobic nanoporous silica particles

Sodium deoxycholate (NaDC), the surfactant molecule employed in this research project, has reported critical micelle concentration (CMC) of 2 ~ 6 *mM* at 20 ~ 25 ^{o}C, aggregation number of 5 and fairly high water-solubility of ~1 *M*. The standard aqueous solutions of 0.6, 6, 60, 100, 200 and 300 *mM* were prepared to perform the initial and qualitative assessment of the capability of this surfactant molecule to solubilize and wet the hydrophobic nanoporous particles in aqueous environment over a broad range of NaDC concentrations. After thorough mixing of particles into each solution, the sample vials were left on work bench without any disturbance for 72 hours to let equilibrate.

A picture was taken after 72 hours to show each mixture at equilibrium, as illustrated in Figure 7.2. The particles were also mixed with deionized water (denoted as 0 *mM*) for comparison. Several important facts are demonstrated by Figure 7.2: (1) it is apparent that the hydrophobic particles cannot be solubilized and wetted by water and stay floating on top of water; (2) at very low concentration of NaDC (0.6 *mM*), which is below the CMC of this surfactant molecule, only a small portion of particles is solubilized and dispersed into solution upon mixing, while the majority of particles cannot be dispersed into solution after remixing. At equilibrium, both the solubilized and insolubilized particles are at the top of the solution, indicating that particles cannot be wetted by NaDC aqueous solution at very low concentration; (3) when the concentration of NaDC solution is above ~ 10-fold higher than the CMC ($\geq$ 60 *mM*), all particles are solubilized and can be well dispersed into the aqueous solution. A portion of the particles is completely wetted by the aqueous solution and sink down to the bottom of the vial. The portion of wetted particles increases as the NaDC concentration increases; (4) even with the capability to solubilize all hydrophobic particles in the mixture at fairly high concentrations, the NaDC aqueous solution is not able to completely wet all these particles. As a result, the solubilized particles are separated into three fractions at equilibrium: the first fraction is the portion of particles, with their outer surface wetted but network of nanopores remaining dry, floating on the top of solution; the second fraction indicates the particles steadily suspended in the NaDC solution. For this portion of particles, their outer surface as well as part of the network of nanopores are wetted by the aqueous solution and thus possess an overall density close to that of water (~1 g/cm^3); the third fraction refers to particles that are completely wetted in the pores by aqueous

solution and sink to the bottom of the vials. As clearly illustrated in Figure 7.2, the concentration of NaDC aqueous solution plays a decisive role on the proportion of the three fractions of the mixture at equilibrium. Details regarding to the three fractions and concentration dependence of solubilization process are discussed in the following sections.

7.3.2. Polarity calibration with fluorescence measurement of pyrene

Pyrene, a fluorophore with high sensitivity to its local microenvironment, was used to approach the dynamics of the NaDC-assisted solubilization of the hydrophobic nanoporous silica particles. As has been well noted in the literature, the intensity ratio of the third and first bands ($R(I_3/I_1)$) in the vibronic fine structure of fluorescence emission spectrum of pyrene is sensitive to solvent polarity. The value of $R(I_3/I_1)$ thus can be used to indicate the polarity of local environment where the pyrene molecules are [254, 255].

In order to accurately evaluate the dynamics of environmental polarity of the sample mixture during the solubilization process, polarity calibration was performed by measuring the fluorescence emission of pyrene in various solvents with a wide range of polarity indices (P'). Table 7.1lists the solvents used for the calibration and the corresponding polarity indices. Three replicates of fluorescence emission spectra of pyrene in each solvent were taken and the averaged spectra are plotted in Figure 7.3A with the normalization to peak 1. The $R(I_3/I_1)$ value of each spectrum was calculated and compared to the literature values [254] in Table 7.1. The measured $R(I_3/I_1)$ values are in general agreement with the literature values and the differences might be attributed to differences in the instrument setup in spectral measurements. As the polarity (index) increases, the $R(I_3/I_1)$ decreases, as shown in Figure 7.3B. To assist the visualization of

this trend, the calculated $R(I_3/I_1)$ values were fit to the model of single exponential decay by NLLS.

The calibration study was subsequently conducted for NaDC solutions over a broad concentration range, up to 200 *mM*. The averaged spectrum at each concentration was normalized to peak 1 and plotted in Figure 7.4A. The corresponding fluorescence intensities obtained from the integration of fluorescence emission spectrum was plotted as a function of NaDC concentration in Figure 7.4B. An increasing trend of fluorescence intensity is observed as the NaDC concentration is elevated. And the intensity gets fairly steady when the NaDC concentration is above 8 *mM*. As well known, the fluorescence quantum yield of pyrene is greatly dependent on its environmental polarity. The higher the polarity, the lower the quantum yield will be. The trend shown in Figure 7.4B thus reveals that the polarity of the microenvironment of pyrene molecules stays almost invariable when the concentration of NaDC is above the CMC, which is ~ 6 *mM* at 25 ^oC. This fact was also demonstrated by the plot of $R(I_3/I_1)$ as a function of the NaDC concentration, as presented in Figure 7.4C. According to the plot, polarity of the microenvironments where pyrene molecules are located changes dramatically at lower NaDC concentrations and reaches a constant when NaDC concentration is elevated above ~8 *mM* because of the formation of micelles. In the low surfactant concentration region, when increasing the concentration of NaDC from 0 to 10 mM, micelles form. The pyrene molecules partition into micelles where the polarity is much lower than aqueous phase until achieves equilibrium. Because of this re-distribution of pyrene molecules —the reporters of local environments, the collected fluorescence spectra exhibit dramatic growth in both intensity and $R(I_3/I_1)$ (Figure 7.4 B and C), indicating an increase in

fluorescence quantum yield associated with a decrease in the polarity of microenvironments of pyrene. When the NaDC concentration is above CMC, essentially all pyrene molecules partition into the hydrophobic region of micelles as the result of hydrophobic interactions. The measured fluorescence intensity as well as $R(I_3/I_1)$ are thus dominated by the environmental polarity of micelles and stay fairly constant.

7.3.3. Kinetics studies of NaDC-assisted solubilization of hydrophobic nanoporous silica particles

The kinetics of the solubilization of the Kromasil C_{18}-derivatized nanoporous particles with the assistance of NaDC was approached by conducting a fluorescence measurements of pyrene incorporated in the NaDC-particle system during the solubilization process. The NaDC solution was at a high concentration of 150 *mM* in this investigation to drive the complex formation between the surfactant and hydrocarbon layer for sufficient solubilization of hydrophobic particles.

Upon mixing ~ 0.05g of particles into the NaDC solution, the NaDC micelles partition into the C_{18} hydrocarbon chains of particles through hydrophobic interactions. At the same time, the pyrene molecules that are originally in micelles start to re-distribute between micelles and the newly formed surfactant-C_{18} constructs until the system reaches equilibrium. Therefore, by monitoring the fluorescence emission of the pyrene molecules in the system, the polarity dynamics of the micelle-particle interactions and the kinetics of the entire solubilization process can be approached.

The solubilization process was monitored for 72 hours based on the observation from qualitative studies that the system became stable and reached equilibrium in the

time period of three days. After mixing particles into NaDC aqueous solution, the sample mixture was pictured at several time points and shown in Figure 7.5. The corresponding fluorescence spectra of pyrene in the mixtures were measured and plotted in Figure 7.6A. As shown in Figure 7.5A, a cloudy mixture was immediately observed upon mixing particles into the surfactant solution. It indicates that the exterior of particles with C_{18} hydrophobic layer could be instantly solubilized by NaDC micelles and dispersed into the aqueous phase. Figure 7.5B taken after 30 min shows sediment of particles to the bottom of cuvette and formation of particle layer on the top of solution as well. The system became fairly stable and minimal changes could be observed after 24 hours, as presented by comparing the pictures taken at time points of 24-hour and 72-hour (Figure 7.5D and E). As clearly shown in the picture taken at the time of 72-hour, three fractions of particles exist after the system reached equilibrium: (1) the top fraction, the fraction of particles floating on top of the solution, (2) the suspended fraction, the fraction of particles suspending in the body of solution and (3) the bottom fraction, the fraction of particles that have sediment to the bottom of cuvette. With the knowledge of average density of the porous particles slightly smaller than 1 g/cm^3, the simultaneous existence of all three possible scenarios of the NaDC-assisted solubilization was demonstrated: First, the top fraction indicates the particles whose exterior is covered by NaDC micelles and become soluble and facilely dispersable in aqueous phase but the interior nanopores stay dry; Second, the suspended fraction represents the particles with exterior fully coated by surfactants and the network of nanopores partially wetted, which results in an overall density of particle ~ 1 g/cm^3 and thus suspend in solution; Third, the bottom fraction

signifies the particles completely covered by micelles and the nanopores are fully wetted by water. Therefore they sink to the bottom of the solution due to their high density.

The fluorescence spectra (Figure 7.6A), taken at discrete time points and averaged from 3 replicates of measurements, exhibit an increase in intensity over time. First of all, the dynamics of polarity during the solubilization process was investigated. The spectra were normalized to peak 1 and replotted in Figure 7.6B to examine the trend in the vibronic band intensity ratio $R(I_3/I_1)$. The spectra showed an unexpected but excellent overlap after normalization, which indicates a constant polarity of the system throughout the solubilization process. The insignificance of change in polarity was again clearly presented as a function of $R(I_3/I_1)$ over time in Figure 7.7A. Before addition of particles, the NaDC solution at 150 mM shows a $R(I_3/I_1)$ of 1.520 with a standard deviation of 0.006. The values of $R(I_3/I_1)$ at each time point of 0, 0.5, 1, 2, 3, 4, 5, 24, 48 and 72 hours after addition of particles were summarized in Table 7.2. The closeness of these values indicated the similarity in the polarities of microenvironments created during the interaction between NaDC micelles and the C_{18}-derivatized nanoporous silica particles. Although the dynamics of polarity of the solubilization process was not able to be accurately approached from the measurement of $R(I_3/I_1)$ of fluorescence emission spectra of pyrene, several crucial facts were still discovered by interpreting the $R(I_3/I_1)$ measured at several important states of the solubilization process: no particles, adding particles into solution ("just added"), reaching equilibrium and reshaking the system after equilibrium ("reshaking"). The $R(I_3/I_1)$ of these 4 important states were plotted and indicated in red, blue, purple and green in Figure 7.7B and the corresponding values were listed in Table 7.2. The important discoveries are:

(1) Comparing the states of “no particle” with “just added”:

It was proven by the immediate dispersion of hydrophobic particles into solution (Figure 7.5A), the exterior surface covering of particles by NaDC surfactants occured immediately after mixing particles into the surfactant solution. The pyrene molecules promptly partitioned into C_{18} layers of exterior of particles upon mixing and the measured $R(I_3/I_1)$ thus reflected the polarity of the microenvironments of the newly formed NaDC micelle-C_{18} constructs on the exterior of particles. Upon the addition of particles into solution, the $R(I_3/I_1)$ increases from 1.520 to 1.544 (Table 7.2) and this increase is significant with the consideration of standard deviations of 0.006 and 0.010, shown as the complete discrete from each other of these two data points in Figure 7.7B. The two-tailed *t* test had a *p* value of 0.022. This increase in $R(I_3/I_1)$ revealed a fact that the polarity of the microenvironments of the newly formed micelle-C_{18} construct is on average lower than that of micelle itself.

(2) Comparing the states of “just added” and “reshaking” :

As shown in Figure 7.5E, there are three fractions of particles at equilibrium and it is practically difficult to separate these three fractions and analyze them individually without any mixing between fractions. The system was thoroughly reshaked by hand and three replicates of fluorescence spectra were collected to provide an averaged assessment of the system, including all three fractions of particles, after it achieved equilibrium. The $R(I_3/I_1)$ increases from 1.532 to 1.580 after reshaking (Table 7.2). Comparing this value to the $R(I_3/I_1)$ of “just added”, there is a significant increase in the $R(I_3/I_1)$ value from 1.544 to 1.580 ($p = 0.0082$ for the two-tailed *t* test), which implies a further decrease in

polarity of microenvironments of the system from the beginning to the end of the solubilization process. As demonstrated above, the polarity of surfactant-C_{18} construct is slightly lower than that of micelle, the decrease in polarity observed upon reshaking at equilibrium therefore suggests that the more surfactant-C_{18} constructs are formed during solubilization process. In other words, at the equilibrium of the NaDC-assisted solubilization process, beside the surfactant-C_{18} constructs fully covered the exterior of particles, more constructs formed during the solubilization process and partially covered the interior surface of particles. This conclusion is consistent with the observation of three fractions of particles in Figure 7.5E.

The kinetics of the NaDC-assisted solubilization of hydrophobic particles was investigated by analyzing the scattering signal during the solubilization process. The scattering signal was resulted from the correction of originally collected fluorescence spectra of pyrene (Figure 7.6A). The collected fluorescence signal was composed by the fluorescence emission from pyrene molecules and the scattering of the excitation light at the water-silica interfaces of particles. The scattering intensity is directly proportional to the concentration of particles in the light path of detection. The scattering signal which caused baseline rise in fluorescence spectra was extracted out and excluded from collected spectra by fitting it to Lorentzian scattering peak, as shown in Figure 7.8A. The change in scattering signal over time and the corresponding NLLS fitting to the model of the 1^{st} order exponential decay were both plotted and shown in Figure 7.8B. The small reduced χ^2 indicates the goodness of this model to describe the decay of scattering signal, reflecting the amount of particles in the light path over time. At the starting time ("just added"), all solubilized particles from all three fractions disperse into the body of solution

and therefore results in the greatest scattering signal. The scattering signal decreases drastically in the first several hours due to the sedimentation of wetted particles to the bottom and the rise of the particles with dry interior up to the top of the solution, as shown in Figure 7.5. The scattering signal reaches a non-zero asymptote after 5 hours. It tells that the system reaches equilibrium and is stabilized in hours. More importantly, the non-zero asymptote of the scattering signal demonstrates the existence of suspended particles that are partially wetted by NaDC aqueous solution, with density close to 1 g/cm^3 at equilibrium. The decay constant τ_1 of 1.03±0.19 hours from the fitting provided a quantitative evaluation of the easiness of this solubilization process to achieve equilibrium.

7.3.4. The effects of NaDC concentration on the solubilization

The performance of NaDC micelles in assisting the solubilization of hydrophobic nanoporous particles in aqueous phase was studied at various concentrations to explore the effect of surfactant concentration on the solubilization process. The solubilization of particles (~ 0.05 *g*) assisted by 30, 40, 150 and 200 *mM* NaDC aqueous solutions was investigated. At each concentration, the fluorescence emission spectra were recorded and analyzed in the same way described above. The decays of scattering signal at each concentration, as well as the corresponding pictures of the system taken at equilibrium were shown in Figure 7.9.

The four insets of pictures show that the distribution of particles among each of the three fractions is greatly dependent on the NaDC concentration. As the concentration increases from 30 to 200 *mM*, the bottom fraction of particles becomes thicker and top fraction is thinner. Considering that similar amount of particles was mixed into each

solution for solubilization, this observation of all four systems at equilibrium reveals that at higher concentrations NaDC micelles offers greater efficiencyin pore wetting by infiltrating the nanopores, convering the pore surfaces and rendering the nanopores hydrophilic. It thus leads to the increase in bottom fraction where particles are completely wetted.

The time constants τ_1 s, resulted from the fitting of the decays of scattering signals, are 6.28 ± 1.09, 6.32 ± 1.03, 1.03 ± 0.19 and 0.86 ± 0.24 hours, respectively. By comparing τ_1 obtained at each investigated concentration of NaDC, it can be concluded that (1) the solubilization of the hydrophobic particles reaches equilibrium faster when assisted by NaDC micelles at higher concentration, as demonstrated by the shorter decay time constants of 1.02 and 0.86 hours for 150 and 200 *mM* NaDC solutions;. (2) the non-zero of the scattering signals at equilibrium demonstrates the existence of suspended particles with partially wetted interior in the solution, for all four systems. And furthermore, a growing trend of the amount of suspended particles is observed as the concentration of NaDC aqueous solution increases, evidenced by the increase in scattering signals of the stabilized systems from ~ 1.35 (30 *mM*) to ~ 1.85 (200 *mM*).

7.4. Conclusions

This chapter presented the preliminary investigation of the solubilization of C_{18}-derivatized nanoporous silica particle in aqueous solution, with the assistance of bile salt, sodium deoxycholate (NaDC), a bio-compatible surfactant. The success in NaDC-assisted solubilization of the hydrophobic particles in aqueous solution was demonstrated in the initial qualitative studies. The polarity of microenvironments of the system during the solubilization process was investigated by measuring the peak 3 to 1 ratio ($R(I_3/I_1)$) of

fluorescence emission spectrum of pyrene incorporated in the system. The kinetic information of the solubilization process was approached from the fitting of the decay of scattering signals over time to the model of 1st order exponential decay. Moreover, the effects of the bile salt concentration on the solubilization as well as the stability of the equilibrated system was also evaluated by comparing the decay time constant τ_1s obtained from the fittings of scattering signals measured during the solubilization processes assisted by NaDC micelles at various concentrations.

Table 7. 1 The values of $R(I_3/I_1)$ of fluorescence spectra of pyrene in various solvents

Solvent	Polarity index (P')	$R(I_3/I_1)_{\text{literature}}$[a]	$R(I_3/I_1)_{\text{experimental}}$
Hexane	0	1.54	1.596±0.063
2-propanol	4	0.94	0.971±0.009
Ethanol	5.1	0.91	0.892±0.010
Methanol	5.2	0.80	0.816±0.014
Acetonitrile	5.8	0.61	0.649±0.009
Water	9	0.62	0.614±0.010

Note: [a] The literature values of $R(I_3/I_1)$ are adapted from [254].

Table 7. 2 The changes in $R(I_3/I_1)$ during the process of NaDC-assisted solubilization of the hydrophobic nanoporous silica particles

Time point (during solubilization)	$R(I_3/I_1)$	Standard deviation of $R(I_3/I_1)$
No particles	1.520	0.006
Just added	1.544	0.010
0.5 hour	1.548	0.022
1 hour	1.540	0.006
2 hours	1.531	0.010
3 hours	1.527	0.014
4 hours	1.529	0.015
5 hours	1.519	0.007
24 hours	1.534	0.005
48 hours	1.538	0.003
72 hours (reaching equilibrium)	1.532	0.006
Reshaking	1.580	0.008

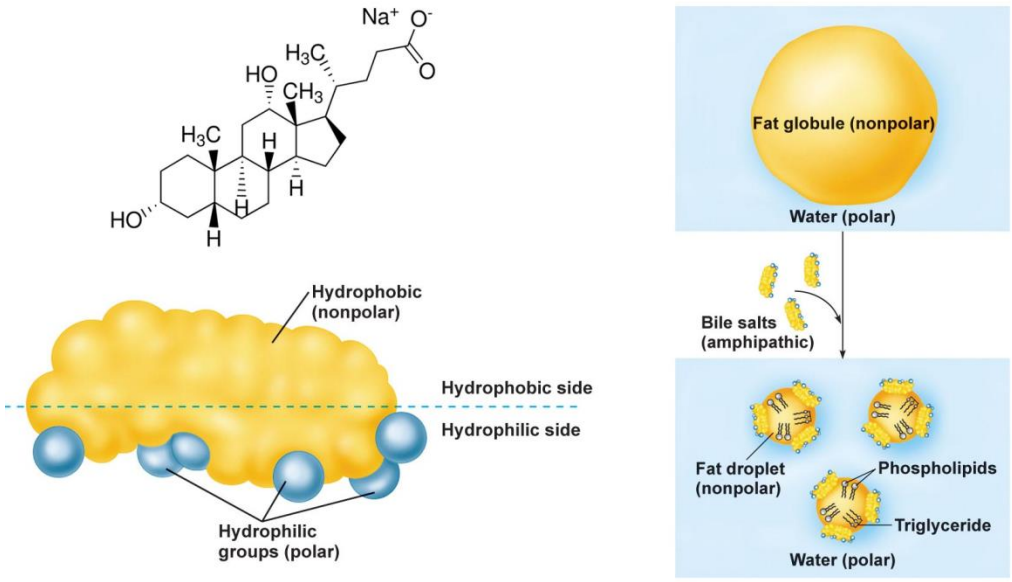

Figure 7. 1 Chemical structure of the NaDC molecule and the emulsification process assisted by NaDC micelles

---

Note: picture source
http://droualb.faculty.mjc.edu/Course%20Materials/Physiology%20101/Chapter%20Notes/Fall%202007/chapter_20%20Fall%202007%20Phy%20101.htm

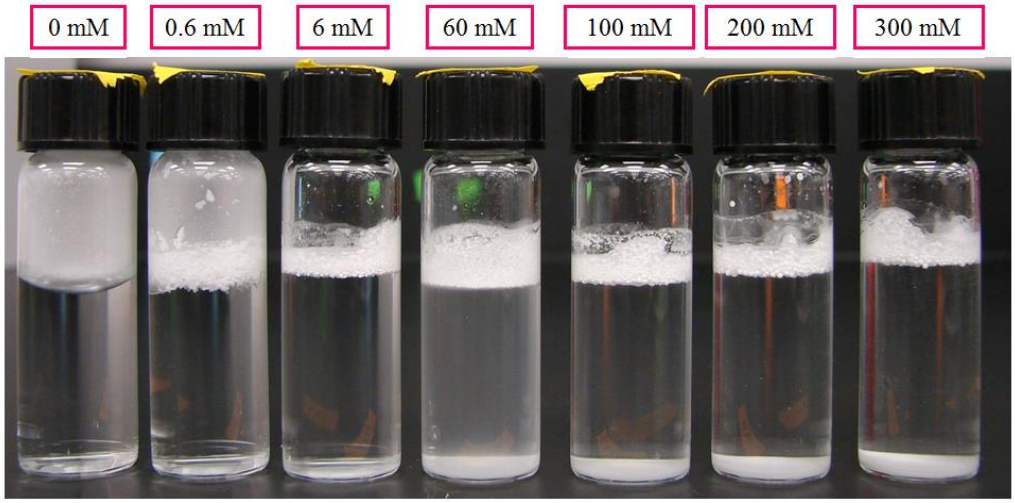

Figure 7. 2 Qualitative studies of solubilization of C_{18}-derivatized nanoporous silica particles with assistance of NaDC at various concentrations

---

Note: The picture was taken 72 hours after sample mixing to show the equilibrium states of solubilization at each concentration of NaDC.

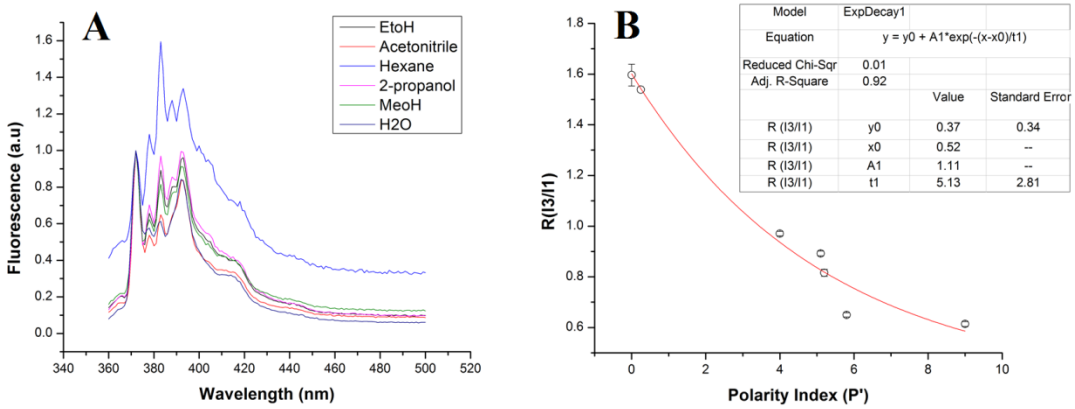

Figure 7. 3 Polarity calibration by fluorescence measurements of pyrene in various solvents

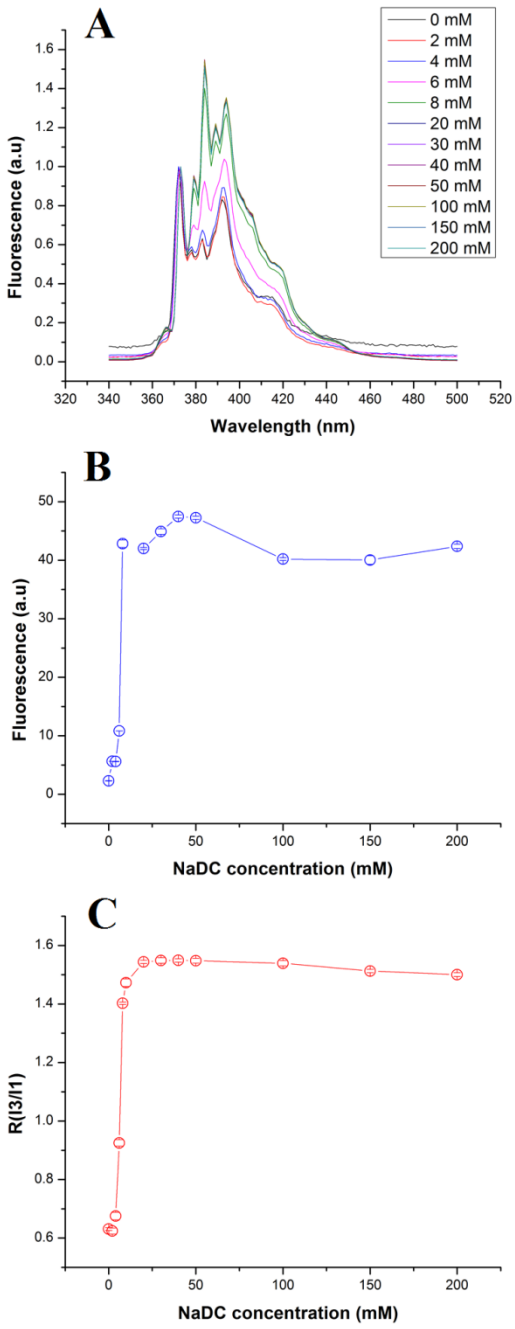

Figure 7. 4 Polarity calibration of NaDC aqueous solutions over a range of concentrations

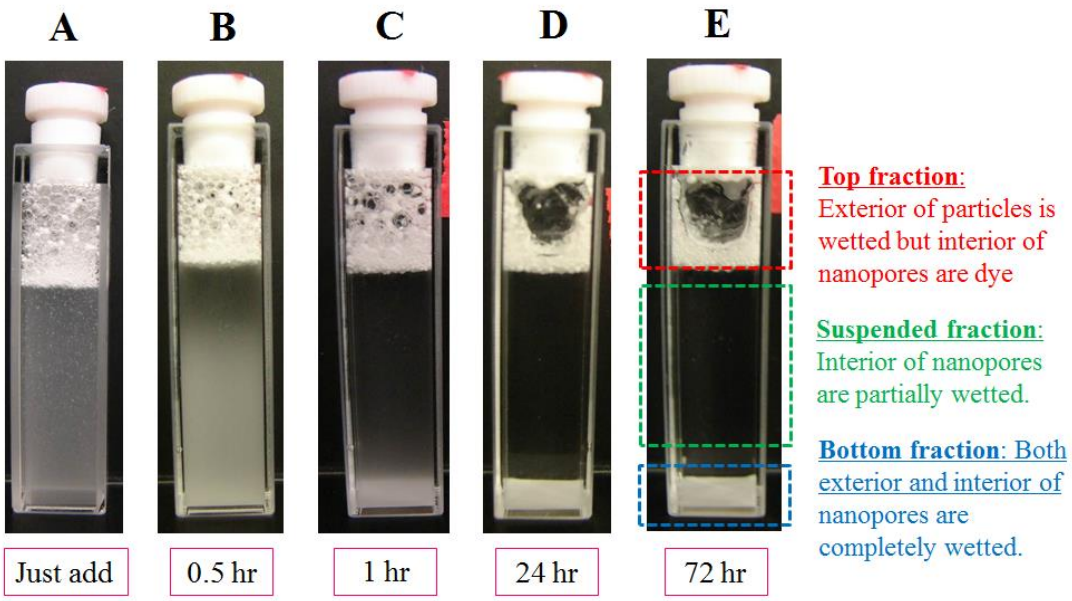

Figure 7. 5 Sample mixture at several time points during the solubilization process

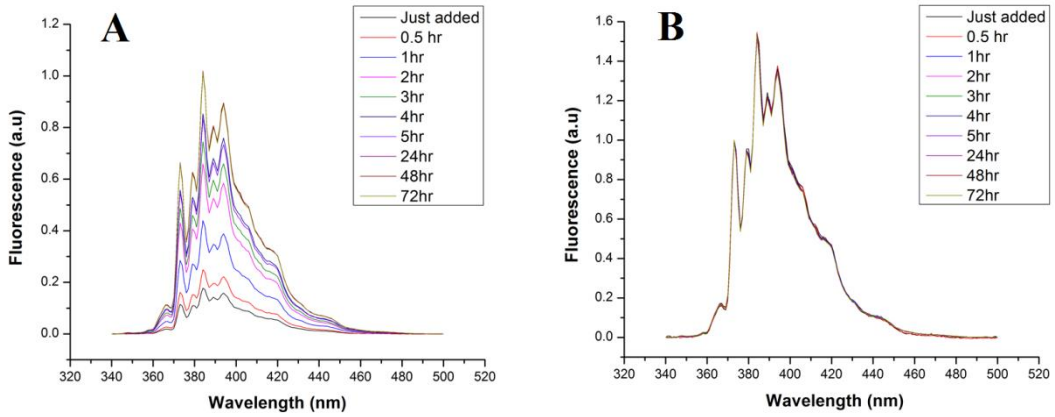

Figure 7. 6 Fluorescence spectra of pyrene in the NaDC micelle-particle system at various time points of solubilization process

---

Note: (A) Original fluorescence emission spectra of pyrene; (B) Fluorescence spectra of pyrene normalized to peak 1.

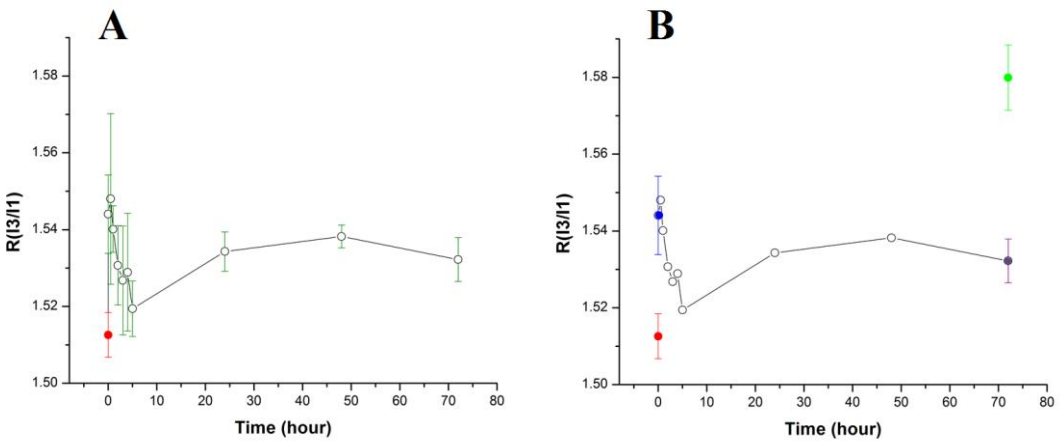

Figure 7. 7 Polarity dynamics of the microenvironments of NaDC micelle-particle system during the solubilization process

---

Note: The error bars in polarity measurement during the solubilization process were excluded in (B) to only signify the polarities ($R(I_3/I_1)$ values) of the system at the beginning and the end of solubilization. Red dot: no particles; blue dot: particles just added; purple dot: system at equilibrium; green dot: remixing sample at equilibrium. Each dot in the plots represents an average of three replicates of measurements.

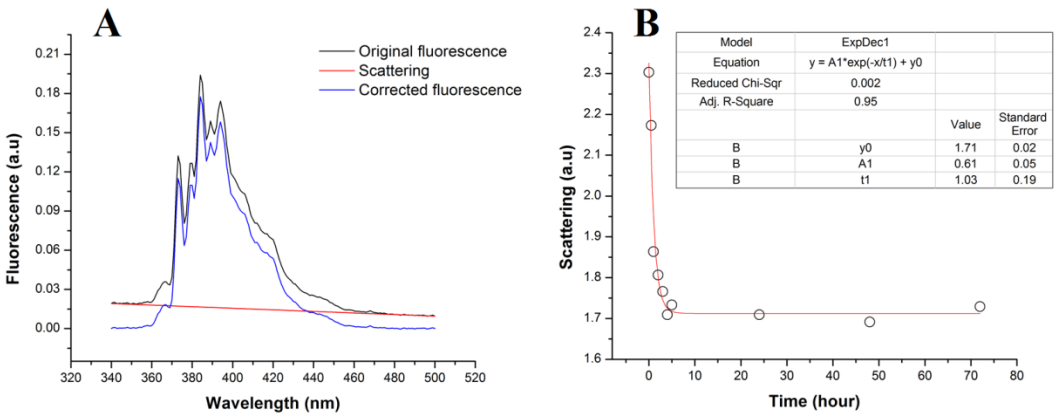

Figure 7. 8 Study of the kinetics of NaDC-assisted solubilization of the particles

---

Note: (A) The correction the fluorescence signal of pyrene emission by subtracting out the scattering signal; (B) Quantitative analysis of scattering signals to approach kinetics of the solubilization process.

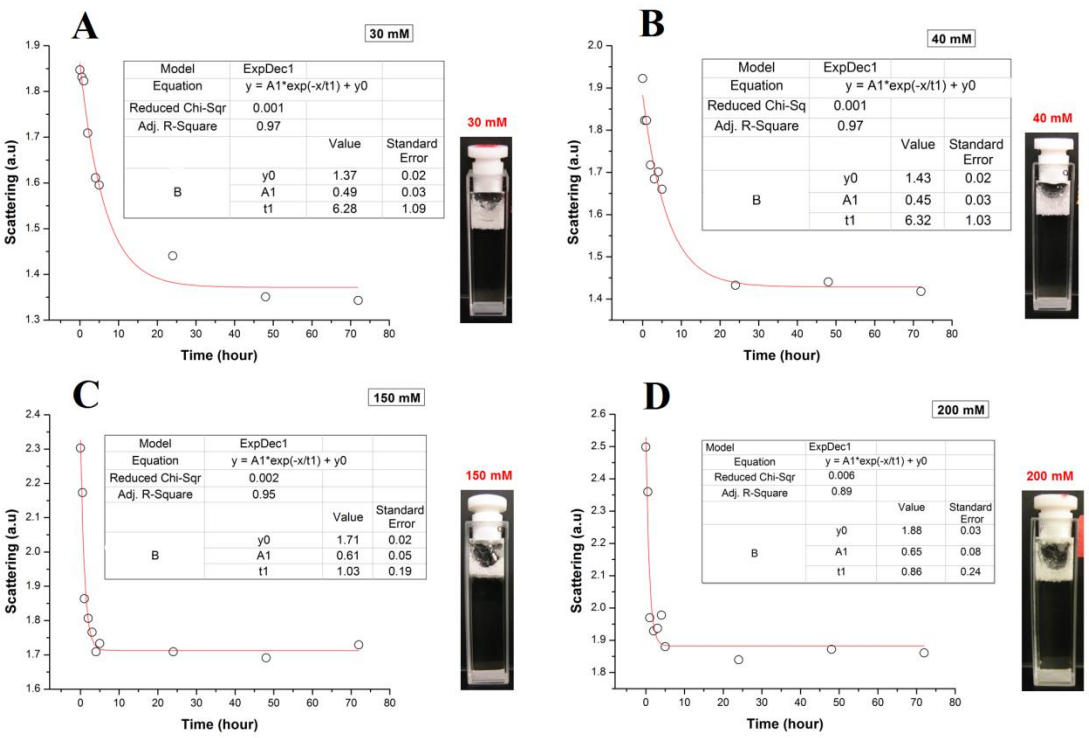

Figure 7. 9 The effects of concentration of NaDC on the solubilization

CHAPTER 8

FUTURE DIRECTIONS

Single molecule counting has been established as a powerful method to characterize molecular transport inside nanoporous silica. Although the research presented in this thesis focuses on probing diffusing molecule in the network of C_{18}-derivatized nanopores, this methodology can be employed to explore various molecular processes in different types of porous materials and biological structures. The measurement of molecular transport will uncover the nature and possible environmental heterogeneity inside the material at which the probe molecules travel since the probe molecule serves as a reporter of local environment.

In the establishment of single molecule counting methodology, a random spatial distribution of single diffusing molecules in the network of nanopores has been demonstrated, as described in Chapter 4. Based on the correlation between the strength of emitted photon burst and the trajectory of molecular diffusing across the Gaussian beam, a probability distribution function has been derived and it enabled the localization of single diffusing molecule at super-resolution. Therefore, as a continuation of this achievement, an innovative technique of super-resolution imaging by localizing individual diffusing fluorophore should be planned. This approach has the advantage of not having to label the structure with fluorophores at very high surface concentration. The success in this work will be a breakthrough in confocal imaging since it offers the observation of single molecules in specimen at super-resolution with accuracy of a few nanometers and most importantly, microsecond kinetics of individual molecules in the

specimen can be approached and these results will directly reveal the micro- and nanoenvironmental heterogeneity in the specimen.

The heterogeneity of ΔG among different nanoporous particles as well as within individual particles has been confirmed, as elaborated in Chapter 6. It plays a decisive role on the performance of fundamental applications of nanoporous particles. For example, it could significantly contribute to the band broadening issue in chromatographic separation. The work presented in this thesis only includes the preliminary studies regarding to method development, system calibration and validation by investigating the ΔG distribution in Luna C_{18}-modified nanoporous silica particles. A comprehensive knowledge of ΔG distribution and the degree of heterogeneity in a variety of nanoporous particles with different pore sizes and surface modifications will be advantageous in making selection for separation applications.

On the basis of the results from the preliminary studies of NaDC-assisted solubilization of the C_{18}-derivatized nanoporous silica particles, alternative methodology is still in need to be developed for further detailed investigation of kinetics and dynamics of physicochemical properties of the system during the solubilization process. This information will be essential for better understanding of the particles as carriers for drug delivery in biology-friendly environments.

REFERENCES

1. G. Ferri, L. Nucara, T. Biver, A. Battisti, G. Signore and R. Bizzarri, *Biophysical Chemistry*, 2016, 208, 17-25.
2. R. M. Martin, J. Rino, A. C. Jesus and M. Carmo-Fonseca, in *Post-Transcriptional Gene Regulation*, ed. E. Dassi, Springer New York, New York, NY, 2016, DOI: 10.1007/978-1-4939-3067-8_22, pp. 335-350.
3. M. Schrader, K. Bahlmann, G. Giese and S. W. Hell*, *Biophysical Journal*, 1998, 75, 1659-1668.
4. W. B. Amos, J. G. White and M. Fordham, *Appl. Opt.*, 1987, 26, 3239-3243.
5. S. Caesar, P.-S. Cynthia and K. Hisato, *Physics in Medicine and Biology*, 1998, 43, 1741.
6. S. Eser, M. Messer, P. Eser, A. von Werder, B. Seidler, M. Bajbouj, R. Vogelmann, A. Meining, J. von Burstin, H. Algül, P. Pagel, A. E. Schnieke, I. Esposito, R. M. Schmid, G. Schneider and D. Saur, *Proceedings of the National Academy of Sciences*, 2011, 108, 9945-9950.
7. Y. Kong, H. Yao, H. Ren, S. Subbian, S. L. G. Cirillo, J. C. Sacchettini, J. Rao and J. D. Cirillo, *Proceedings of the National Academy of Sciences*, 2010, 107, 12239-12244.
8. J.-H. Huang, F.-C. Chien, P. Chen, K.-C. Ho and C.-W. Chu, *Analytical Chemistry*, 2010, 82, 1669-1673.
9. Q.-X. Zhang, R.-W. Lu, Y.-G. Li and X.-C. Yao, *Optics Letters*, 2011, 36, 4692-4694.
10. W. F. J. Vermaas, J. A. Timlin, H. D. T. Jones, M. B. Sinclair, L. T. Nieman, S. W. Hamad, D. K. Melgaard and D. M. Haaland, *Proceedings of the National Academy of Sciences*, 2008, 105, 4050-4055.
11. C. Charalampaki, S. Foersch, A. Heimann, K. Mpoukouvalas and O. Kempski, *Journal of Neurological Surgery Part B: Skull Base*, 2012, 73, A049.
12. P. N. Prasad, 2003, 3.
13. G. M. R. De Luca, R. M. P. Breedijk, R. A. J. Brandt, C. H. C. Zeelenberg, B. E. de Jong, W. Timmermans, L. N. Azar, R. A. Hoebe, S. Stallinga and E. M. M. Manders, *Biomed. Opt. Express*, 2013, 4, 2644-2656.
14. A. A. Michelson, *(The University of Chicago Press, Chicago, Ill.)*, 1927.
15. H. W. Robert, *Reports on Progress in Physics*, 1996, 59, 427.
16. T. W. Jennifer C. Waters, 2014, 123, 20.
17. M. M. Frigault, J. Lacoste, J. L. Swift and C. M. Brown, *Journal of Cell Science*, 2009, 122, 753-767.
18. J. L. K. Y. C. M. Brown, 2013, 61.

19. S. Sharonov, I. Chourpa, H. Morjani, I. Nabiev, M. Manfait and A. Feofanov, *Analytica Chimica Acta*, 1994, 290, 40-47.

20. T. Zimmermann, J. Rietdorf and R. Pepperkok, *FEBS Letters*, 2003, 546, 87-92.

21. M. R. Tadross, S. A. Park, B. Veeramani and D. T. Yue, *Journal of microscopy*, 2009, 233, 192-204.

22. R. B. Sekar and A. Periasamy, *The Journal of cell biology*, 2003, 160, 629-633.

23. C. A. Day, L. J. Kraft, M. Kang and A. K. Kenworthy, *Current Protocols in Cytometry*, 2012, 2.19. 11-12.19. 29.

24. M. Kang, C. A. Day, E. DiBenedetto and A. K. Kenworthy, *Biophysical journal*, 2010, 99, 2737-2747.

25. B. Moomaw, *Methods Cell Biol*, 2007, 81, 251-283.

26. J. Pawley and B. R. Masters, *Optical Engineering*, 1996, 35, 251–262.

27. V. Vukojević, M. Heidkamp, Y. Ming, B. Johansson, L. Terenius and R. Rigler, *Proceedings of the National Academy of Sciences*, 2008, 105, 18176-18181.

28. J. M. Murray, P. L. Appleton, J. R. Swedlow and J. C. Waters, *Journal of microscopy*, 2007, 228, 390-405.

29. D. E. Wolf, C. Samarasekera and J. R. Swedlow, *Methods Cell Biol*, 2007, 81, 365-396.

30. L. R. M. J.K. Stevens, J.E. Trogadis, 1994, 48-90.

31. J. B. Pawley, in *Handbook of biological confocal microscopy*, Springer, 2006, pp. 20-42.

32. S. Wilhelm, 23.

33. J. C. Waters, *The Journal of cell biology*, 2009, 185, 1135-1148.

34. M. S. Robbins and B. J. Hadwen, *Electron Devices, IEEE Transactions on*, 2003, 50, 1227-1232.

35. M. R. Young and S. Singh, *Optics letters*, 1988, 13, 21-23.

36. J. M. Murray, in *Methods in Cell Biology*, eds. S. Greenfield and E. W. David, Academic Press, 2013, vol. Volume 114, pp. 427-440.

37. J. M. Zwier, G. J. Van Rooij, J. W. Hofstraat and G. J. Brakenhoff, *Journal of Microscopy*, 2004, 216, 15-24.

38. D. E. W. Greenfield Sluder, 2007, 365-396.

39. G. Rabut and J. Ellenberg, *Live Cell Imaging—A Laboratory Manual. RD Goldman and DL Spector, editors. Cold Spring Harbor Laboratory Press, Cold Spring Harbor, NY*, 2005, 101-126.

40. R. Ghauharali and G. Brakenhoff, *Journal of microscopy*, 2000, 198, 88-100.

41. B. Rotman, *Proceedings of the National Academy of Sciences*, 1961, 47, 1981-1991.

42. T. Hirschfeld, *Appl. Opt.*, 1976, 15, 2965-2966.
43. W. Moerner and L. Kador, *Analytical Chemistry*, 1989, 61, 1217A-1223A.
44. W. E. Moerner and L. Kador, *Physical Review Letters*, 1989, 62, 2535.
45. W. Moerner and M. Orrit, *Science*, 1999, 283, 1670-1676.
46. E. B. Shera, N. K. Seitzinger, L. M. Davis, R. A. Keller and S. A. Soper, *Chemical Physics Letters*, 1990, 174, 553-557.
47. S. Soper, R. Keller, E. Shera, J. Martin and J. Jett, 1990.
48. W. Moerner, *The Journal of Physical Chemistry B*, 2002, 106, 910-927.
49. W. Moerner and D. P. Fromm, *Review of Scientific Instruments*, 2003, 74, 3597-3619.
50. S. Weiss, *Science*, 1999, 283, 1676-1683.
51. A. Gräslund, R. Rigler, J. Widengren and P. Press, *Single molecule spectroscopy in chemistry, physics and biology*, Springer, 2010.
52. Y. Hou, A. M. Bardo, C. Martinez and D. A. Higgins, *The Journal of Physical Chemistry B*, 2000, 104, 212-219.
53. D. S. English, E. J. Harbron and P. F. Barbara, *The Journal of Chemical Physics*, 2001, 114, 10479-10485.
54. Y. Fu, M. M. Collinson and D. A. Higgins, *Journal of the American Chemical Society*, 2004, 126, 13838-13844.
55. S. A. Martin-Brown, Y. Fu, G. Saroja, M. M. Collinson and D. A. Higgins, *Analytical chemistry*, 2005, 77, 486-494.
56. K. D. Weston, P. J. Carson, H. Metiu and S. K. Buratto, *The Journal of chemical physics*, 1998, 109, 7474-7485.
57. S. Liu, G. Bokinsky, N. G. Walter and X. Zhuang, *Proceedings of the National Academy of Sciences*, 2007, 104, 12634-12639.
58. H. P. Lu, L. Xun and X. S. Xie, *Science*, 1998, 282, 1877-1882.
59. X. S. Xie, *The Journal of chemical physics*, 2002, 117, 11024-11032.
60. L. Edman, Z. Földes-Papp, S. Wennmalm and R. Rigler, *Chemical Physics*, 1999, 247, 11-22.
61. T. Ha, A. Y. Ting, J. Liang, W. B. Caldwell, A. A. Deniz, D. S. Chemla, P. G. Schultz and S. Weiss, *Proceedings of the National Academy of Sciences*, 1999, 96, 893-898.
62. X. Michalet, S. Weiss and M. Jäger, *Chemical reviews*, 2006, 106, 1785-1813.
63. B. Schuler and W. A. Eaton, *Current opinion in structural biology*, 2008, 18, 16-26.
64. B. Schuler, E. A. Lipman and W. A. Eaton, *Nature*, 2002, 419, 743-747.

65. W. Moerner, *Science*, 1997, 277, 1059.

66. W. Ambrose and W. Moerner, 1991.

67. W. Moerner, M. Orrit, U. Wild and T. Basché, *Single-molecule optical detection, imaging and spectroscopy*, John Wiley & Sons, 2008.

68. K. D. Weston and S. K. Buratto, *The Journal of Physical Chemistry A*, 1998, 102, 3635-3638.

69. W.-T. Yip, D. Hu, J. Yu, D. A. Vanden Bout and P. F. Barbara, *The Journal of Physical Chemistry A*, 1998, 102, 7564-7575.

70. R. M. Dickson, A. B. Cubitt, R. Y. Tsien and W. Moerner, *Nature*, 1997, 388, 355-358.

71. T. Basché, S. Kummer and C. Bräuchle, *Nature*, 1995, 373, 132-134.

72. R. Roy, S. Hohng and T. Ha, *Nature methods*, 2008, 5, 507-516.

73. W. P. Ambrose, P. M. Goodwin and J. P. Nolan, *Cytometry*, 1999, 36, 224-231.

74. S. Holland, G. Goldhaber, D. Groom, W. Moses, C. Pennypacker, S. Perlmutter, N. Wang, R. Stover and M. Wei, 1996.

75. W. B. Whitten, J. M. Ramsey, S. Arnold and B. V. Bronk, *Analytical chemistry*, 1991, 63, 1027-1031.

76. L. Q. Li and L. M. Davis, *Review of Scientific Instruments*, 1993, 64, 1524-1529.

77. C. Xu, W. Zipfel, J. B. Shear, R. M. Williams and W. W. Webb, *Proceedings of the National Academy of Sciences*, 1996, 93, 10763-10768.

78. E. Papagiakoumou, A. Bègue, B. Leshem, O. Schwartz, B. M. Stell, J. Bradley, D. Oron and V. Emiliani, *Nature photonics*, 2013, 7, 274-278.

79. T. Basché, W. Ambrose and W. Moerner, *JOSA B*, 1992, 9, 829-836.

80. W. P. Ambrose, P. M. Goodwin, R. A. Keller and J. C. Martin, *Science*, 1994, 265, 364-367.

81. R. M. Dickson, D. j Norris, Y.-L. Tzeng and W. Moerner, *Science*, 1996, 274, 966.

82. M. Paige, E. Bjerneld and W. Moerner, *Single Molecules*, 2001, 2, 191-202.

83. K. I. Willig, B. Harke, R. Medda and S. W. Hell, *Nature methods*, 2007, 4, 915-918.

84. B. Huang, W. Wang, M. Bates and X. Zhuang, *Science*, 2008, 319, 810-813.

85. B. Huang, M. Bates and X. Zhuang, *Annual review of biochemistry*, 2009, 78, 993.

86. X. Qu, D. Wu, L. Mets and N. F. Scherer, *Proceedings of the National Academy of Sciences of the United States of America*, 2004, 101, 11298-11303.

87. A. A. Deniz, S. Mukhopadhyay and E. A. Lemke, *Journal of The Royal Society Interface*, 2008, 5, 15-45.

88. M. W. Holman, R. Liu, L. Zang, P. Yan, S. A. DiBenedetto, R. D. Bowers and D. M. Adams, *Journal of the American Chemical Society*, 2004, 126, 16126-16133.

89. T. Funatsu, Y. Harada, M. Tokunaga, K. Saito and T. Yanagida, *Nature*, 1995, 374, 555-559.

90. E. Rhoades, E. Gussakovsky and G. Haran, *Proceedings of the National Academy of Sciences*, 2003, 100, 3197-3202.

91. Y. Takei, R. Iizuka, T. Ueno and T. Funatsu, *Journal of Biological Chemistry*, 2012, 287, 41118-41125.

92. H. S. Chung, J. M. Louis and W. A. Eaton, *Proceedings of the National Academy of Sciences*, 2009, 106, 11837-11844.

93. C.-B. Li, H. Yang and T. Komatsuzaki, *Proceedings of the National Academy of Sciences*, 2008, 105, 536-541.

94. K. A. Merchant, R. B. Best, J. M. Louis, I. V. Gopich and W. A. Eaton, *Proceedings of the National Academy of Sciences*, 2007, 104, 1528-1533.

95. H. Yang, G. Luo, P. Karnchanaphanurach, T.-M. Louie, I. Rech, S. Cova, L. Xun and X. S. Xie, *Science*, 2003, 302, 262-266.

96. J.-B. Lee, R. K. Hite, S. M. Hamdan, X. Sunney Xie, C. C. Richardson and A. M. van Oijen, *Nature*, 2006, 439, 621-624.

97. L. Gu, C. Li, J. Aach, D. E. Hill, M. Vidal and G. M. Church, *Nature*, 2014, 515, 554-557.

98. I. Konig, A. Zarrine-Afsar, M. Aznauryan, A. Soranno, B. Wunderlich, F. Dingfelder, J. C. Stuber, A. Pluckthun, D. Nettels and B. Schuler, *Nat Meth*, 2015, 12, 773-779.

99. F. T, *Ann Phys*, 1948, 2, 23.

100. A. Gust, A. Zander, A. Gietl, P. Holzmeister, S. Schulz, B. Lalkens, P. Tinnefeld and D. Grohmann, *Molecules*, 2014, 19, 15824.

101. A. Tsai, A. Petrov, R. A. Marshall, J. Korlach, S. Uemura and J. D. Puglisi, *Nature*, 2012, 487, 390-393.

102. P. Milón, C. Maracci, L. Filonava, C. O. Gualerzi and M. V. Rodnina, *Nat Struct Mol Biol*, 2012, 19, 609-615.

103. P. R. Banerjee and A. A. Deniz, *Chemical Society Reviews*, 2014, 43, 1172-1188.

104. E. V. Kuzmenkina, C. D. Heyes and G. U. Nienhaus, *Proceedings of the National Academy of Sciences*, 2005, 102, 15471-15476.

105. T. Ha, T. Enderle, D. F. Ogletree, D. S. Chemla, P. R. Selvin and S. Weiss, *Proceedings of the National Academy of Sciences*, 1996, 93, 6264-6268.

106. P. R. Selvin, *Nat Struct Mol Biol*, 2000, 7, 730-734.

107. F. Hillger, D. Nettels, S. Dorsch and B. Schuler, *Journal of Fluorescence*, 2007, 17, 759-765.

108. J. Lee, Y. Miyanaga, M. Ueda and S. Hohng, *Biophysical Journal*, 103, 1691-1697.

109. Z. Zhong, *Dissertation*, 2007.

110. H. Zheng, L. S. Goldner and S. H. Leuba, *Methods*, 2007, 41, 342-352.

111. P. M. Lundquist, C. F. Zhong, P. Zhao, A. B. Tomaney, P. S. Peluso, J. Dixon, B. Bettman, Y. Lacroix, D. P. Kwo, E. McCullough, M. Maxham, K. Hester, P. McNitt, D. M. Grey, C. Henriquez, M. Foquet, S. W. Turner and D. Zaccarin, *Opt. Lett.*, 2008, 33, 1026-1028.

112. Z. Zhong, M. Lowry, G. Wang and L. Geng, *Analytical Chemistry*, 2005, 77, 2303-2310.

113. A. K. Dutta, K. Kamada and K. Ohta, *Journal of Photochemistry and Photobiology A: Chemistry*, 1996, 93, 57-64.

114. D. L. Sackett and J. Wolff, *Analytical Biochemistry*, 1987, 167, 228-234.

115. J. Hendriks, T. Gensch, L. Hviid, M. A. van der Horst, K. J. Hellingwerf and J. J. van Thor, *Biophysical Journal*, 2002, 82, 1632-1643.

116. C. S. Brumaru, *Dissertation*, 2012.

117. D. Renker, *Nuclear Instruments and Methods in Physics Research Section A: Accelerators, Spectrometers, Detectors and Associated Equipment*, 2002, 486, 164-169.

118. Z. Zhong and M. L. Geng, *Analytical Chemistry*, 2007, 79, 6709-6717.

119. A. N. (company).

120. P. (company).

121. E. M. Freer, L. E. Krupp, W. D. Hinsberg, P. M. Rice, J. L. Hedrick, J. N. Cha, R. D. Miller and H.-C. Kim, *Nano letters*, 2005, 5, 2014-2018.

122. N. K. Raman, M. T. Anderson and C. J. Brinker, *Chemistry of Materials*, 1996, 8, 1682-1701.

123. S. Ito, S. Fukuya, T. Kusumi, Y. Ishibashi, H. Miyasaka, Y. Goto, M. Ikai, T. Tani and S. Inagaki, *The Journal of Physical Chemistry C*, 2009, 113, 11884-11891.

124. J. J. Lange, M. M. Collinson, C. T. Culbertson and D. A. Higgins, *Analytical chemistry*, 2009, 81, 10089-10096.

125. D. A. Higgins and M. M. Collinson, *Langmuir*, 2005, 21, 9023-9031.

126. L. Cai, N. Friedman and X. S. Xie, *Nature*, 2006, 440, 358-362.

127. S. Y. Kim, Z. Gitai, A. Kinkhabwala, L. Shapiro and W. Moerner, *Proceedings of the National Academy of Sciences*, 2006, 103, 10929-10934.

128. G.-W. Li and X. S. Xie, *Nature*, 2011, 475, 308-315.

129. J. C. M. Gebhardt, D. M. Suter, R. Roy, Z. W. Zhao, A. R. Chapman, S. Basu, T. Maniatis and X. S. Xie, *Nature methods*, 2013, 10, 421-426.

130. M. J. Wirth, D. J. Swinton and M. D. Ludes, *The Journal of Physical Chemistry B*, 2003, 107, 6258-6268.

131. M. J. Wirth and M. A. Legg, *Annu. Rev. Phys. Chem.*, 2007, 58, 489-510.

132. S. Kim, C. M. Schroeder and X. S. Xie, *Journal of molecular biology*, 2010, 395, 995-1006.

133. M. D. Ludes and M. J. Wirth, *Analytical chemistry*, 2002, 74, 386-393.

134. O. P. Hamill, A. Marty, E. Neher, B. Sakmann and F. Sigworth, *Pflügers Archiv*, 1981, 391, 85-100.

135. J. Elf, G.-W. Li and X. S. Xie, *Science*, 2007, 316, 1191-1194.

136. I. Golding, J. Paulsson, S. M. Zawilski and E. C. Cox, *Cell*, 2005, 123, 1025-1036.

137. J. Deich, E. Judd, H. McAdams and W. Moerner, *Proceedings of the National Academy of Sciences of the United States of America*, 2004, 101, 15921-15926.

138. M. D. Wang, M. J. Schnitzer, H. Yin, R. Landick, J. Gelles and S. M. Block, *Science*, 1998, 282, 902-907.

139. Y. Taniguchi, P. J. Choi, G.-W. Li, H. Chen, M. Babu, J. Hearn, A. Emili and X. S. Xie, *Science*, 2010, 329, 533-538.

140. J. Yu, J. Xiao, X. Ren, K. Lao and X. S. Xie, *Science*, 2006, 311, 1600-1603.

141. P. J. Choi, L. Cai, K. Frieda and X. S. Xie, *Science*, 2008, 322, 442-446.

142. A. W. Kirkeminde, T. Torres, T. Ito and D. A. Higgins, *The Journal of Physical Chemistry B*, 2011, 115, 12736-12743.

143. J. Clarke, H.-C. Wu, L. Jayasinghe, A. Patel, S. Reid and H. Bayley, *Nature nanotechnology*, 2009, 4, 265-270.

144. C. Ma and E. S. Yeung, *Analytical chemistry*, 2009, 82, 478-482.

145. C. Jung, J. Kirstein, B. Platschek, T. Bein, M. Budde, I. Frank, K. Müllen, J. Michaelis and C. Bräuchle, *Journal of the American Chemical Society*, 2008, 130, 1638-1648.

146. M. Foquet, J. Korlach, W. R. Zipfel, W. W. Webb and H. G. Craighead, *Analytical chemistry*, 2004, 76, 1618-1626.

147. M. Foquet, J. Korlach, W. Zipfel, W. W. Webb and H. G. Craighead, *Analytical Chemistry*, 2002, 74, 1415-1422.

148. L. A. Tessler, J. G. Reifenberger and R. D. Mitra, *Analytical chemistry*, 2009, 81, 7141-7148.

149. A. H. Wu, S. J. Agee, Q. A. Lu, J. Todd and A. S. Jaffe, *Clinical chemistry*, 2009, 55, 196-198.

150. B. Huang, H. Wu, D. Bhaya, A. Grossman, S. Granier, B. K. Kobilka and R. N. Zare, *Science*, 2007, 315, 81-84.

151. C. Zander, K. Drexhage, K.-T. Han, J. Wolfrum and M. Sauer, *Chemical physics letters*, 1998, 286, 457-465.

152. J. Todd, B. Freese, A. Lu, D. Held, J. Morey, R. Livingston and P. Goix, *Clinical chemistry*, 2007, 53, 1990-1995.

153. Y. Gao, Z. Zhong and M. L. Geng, *Applied spectroscopy*, 2007, 61, 956-962.

154. M. P. Gordon, T. Ha and P. R. Selvin, *Proceedings of the National Academy of Sciences of the United States of America*, 2004, 101, 6462-6465.

155. M. J. Rust, M. Bates and X. Zhuang, *Nature methods*, 2006, 3, 793-796.

156. D. S. Heron, M. Shinitzky, M. Hershkowitz and D. Samuel, *Proceedings of the National Academy of Sciences*, 1980, 77, 7463-7467.

157. T. Koike, G. Ishida, M. Taniguchi, K. Higaki, Y. Ayaki, M. Saito, Y. Sakakihara, M. Iwamori and K. Ohno, *Biochimica et Biophysica Acta (BBA) - Molecular Basis of Disease*, 1998, 1406, 327-335.

158. M. A. Haidekker and E. A. Theodorakis, *Organic & Biomolecular Chemistry*, 2007, 5, 1669-1678.

159. S. M. K.Shiraishi, H.Ishida and H.Nakazawa, *Alcohol and Alcoholism* 1993, 28, 6.

160. O. S. Nadiv, M Manu, H Hecht, D Roberts, C T LeRoith, D Zick, Y, *Biochem. J.* , 1994, 298, 8.

161. W. Osterode, C. Holler and F. Ulberth, *Diabetic Medicine*, 1996, 13, 1044-1050.

162. P. Chugha, H. J. Sage and T. G. Oas, *Protein Science*, 2006, 15, 533-542.

163. Y.-C. Chang, W. R. Franch and T. G. Oas, *Biochemistry*, 2010, 49, 9428-9437.

164. C. H. Henkels, Y.-C. Chang, S. I. Chamberlin and T. G. Oas, *Biochemistry*, 2007, 46, 15062-15075.

165. H. J. Dyson and P. E. Wright, *Chemical Reviews*, 2004, 104, 3607-3622.

166. W.-Y. Choy, D. Shortle and L. E. Kay, *Journal of the American Chemical Society*, 2003, 125, 1748-1758.

167. I. H. McColl, E. W. Blanch, L. Hecht, N. R. Kallenbach and L. D. Barron, *Journal of the American Chemical Society*, 2004, 126, 5076-5077.

168. D. M. Korzhnev, K. Kloiber and L. E. Kay, *Journal of the American Chemical Society*, 2004, 126, 7320-7329.

169. D. M. Korzhnev, K. Kloiber, V. Kanelis, V. Tugarinov and L. E. Kay, *Journal of the American Chemical Society*, 2004, 126, 3964-3973.

170. P. Neudecker, A. Zarrine-Afsar, W.-Y. Choy, D. R. Muhandiram, A. R. Davidson and L. E. Kay, *Journal of Molecular Biology*, 2006, 363, 958-976.

171. P. Lundström, D. F. Hansen, P. Vallurupalli and L. E. Kay, *Journal of the American Chemical Society*, 2009, 131, 1915-1926.

172. O. Millet, D. R. Muhandiram, N. R. Skrynnikov and L. E. Kay, *Journal of the American Chemical Society*, 2002, 124, 6439-6448.

173. N. R. Skrynnikov, O. Millet and L. E. Kay, *Journal of the American Chemical Society*, 2002, 124, 6449-6460.

174. J. Yao, H. J. Dyson and P. E. Wright, *FEBS Letters*, 1997, 419, 285-289.

175. D. M. Korzhnev, T. L. Religa, W. Banachewicz, A. R. Fersht and L. E. Kay, *Science*, 2010, 329, 1312-1316.

176. S. Haldar, M. Kombrabail, G. Krishnamoorthy and A. Chattopadhyay, *Journal of Fluorescence*, 2010, 20, 407-413.

177. S. K. Jha, D. Dhar, G. Krishnamoorthy and J. B. Udgaonkar, *Proceedings of the National Academy of Sciences*, 2009, 106, 11113-11118.

178. K. S. G.S. Lakshmikanth1, G. Krishnamoorthy1 & Jayant B. Udgaonkar2, *Nature Structural Biology*, 2001, 8, 6.

179. J. G. Lyubovitsky, H. B. Gray and J. R. Winkler, *Journal of the American Chemical Society*, 2002, 124, 14840-14841.

180. K. Sridevi, G. S. Lakshmikanth, G. Krishnamoorthy and J. B. Udgaonkar, *Journal of Molecular Biology*, 2004, 337, 699-711.

181. R. Swaminathan and N. Periasamy, *Proc. Indian Acad. Sci. (Chem. Sci.)*, 1996, 108, 39-49.

182. S. S. Sarkar, J. B. Udgaonkar and G. Krishnamoorthy, *The Journal of Physical Chemistry B*, 2011, 115, 7479-7486.

183. A. M. Saxena, J. B. Udgaonkar and G. Krishnamoorthy, *Journal of Molecular Biology*, 2006, 359, 174-189.

184. T. Kues, A. Dickmanns, R. Lührmann, R. Peters and U. Kubitscheck, *Proceedings of the National Academy of Sciences*, 2001, 98, 12021-12026.

185. O. Seksek, J. Biwersi and A. S. Verkman, *The Journal of Cell Biology*, 1997, 138, 131-142.

186. D. Grünwald, R. M. Martin, V. Buschmann, D. P. Bazett-Jones, H. Leonhardt, U. Kubitscheck and M. C. Cardoso, *Biophysical Journal*, 2008, 94, 2847-2858.

187. M. A. Haidekker, T. P. Brady, D. Lichlyter and E. A. Theodorakis, *Journal of the American Chemical Society*, 2005, 128, 398-399.

188. X. Peng, Z. Yang, J. Wang, J. Fan, Y. He, F. Song, B. Wang, S. Sun, J. Qu, J. Qi and M. Yan, *Journal of the American Chemical Society*, 2011, 133, 6626-6635.

189. S. Haldar, M. Kombrabail, G. Krishnamoorthy and A. Chattopadhyay, *The Journal of Physical Chemistry Letters*, 2012, 3, 2676-2681.

190. M. K. Kuimova, S. W. Botchway, A. W. Parker, M. Balaz, H. A. Collins, H. L. Anderson, K. Suhling and P. R. Ogilby, *Nat Chem*, 2009, 1, 69-73.

191. P. Verveer and P. H. Bastiaens, *Histochem Cell Biol*, 2008, 130, 833-843.

192. M. A. Digman, C. M. Brown, P. Sengupta, P. W. Wiseman, A. R. Horwitz and E. Gratton, *Biophysical Journal*, 2005, 89, 1317-1327.

193. M. A. Digman, P. Sengupta, P. W. Wiseman, C. M. Brown, A. R. Horwitz and E. Gratton, *Biophysical Journal*, 2005, 88, L33-L36.

194. S. J. Lord, Z. Lu, H. Wang, K. A. Willets, P. J. Schuck, H.-l. D. Lee, S. Y. Nishimura, R. J. Twieg and W. E. Moerner, *The Journal of Physical Chemistry A*, 2007, 111, 8934-8941.

195. N. L. Thompson, A. M. Lieto and N. W. Allen, *Current Opinion in Structural Biology*, 2002, 12, 634-641.

196. M. K. Kuimova, G. Yahioglu and P. R. Ogilby, *Journal of the American Chemical Society*, 2008, 131, 332-340.

197. J. W. Wojcieszyn, R. A. Schlegel, E. S. Wu and K. A. Jacobson, *Proceedings of the National Academy of Sciences*, 1981, 78, 4407-4410.

198. M. Dakanali, T. H. Do, A. Horn, A. Chongchivivat, T. Jarusreni, D. Lichlyter, G. Guizzunti, M. A. Haidekker and E. A. Theodorakis, *Bioorganic & Medicinal Chemistry*, 2012, 20, 4443-4450.

199. M. A. H. Alamiry, A. C. Benniston, G. Copley, K. J. Elliott, A. Harriman, B. Stewart and Y.-G. Zhi, *Chemistry of Materials*, 2008, 20, 4024-4032.

200. M. E. Nipper, S. Majd, M. Mayer, J. C. M. Lee, E. A. Theodorakis and M. A. Haidekker, *Biochimica et Biophysica Acta (BBA) - Biomembranes*, 2008, 1778, 1148-1153.

201. J. A. Levitt, M. K. Kuimova, G. Yahioglu, P.-H. Chung, K. Suhling and D. Phillips, *The Journal of Physical Chemistry C*, 2009, 113, 11634-11642.

202. M. A. Haidekker, A. G. Tsai, T. Brady, H. Y. Stevens, J. A. Frangos, E. Theodorakis and M. Intaglietta, *American Journal of Physiology - Heart and Circulatory Physiology*, 2002, 282, H1609-H1614.

203. L. L. Zhu, X. Li, F.-Y. Ji, X. Ma, Q.-C. Wang and H. Tian, *Langmuir*, 2009, 25, 3482-3486.

204. M. E. Nipper, M. Dakanali, E. Theodorakis and M. A. Haidekker, *Biochimie*, 2011, 93, 988-994.

205. Z. Z. Gao Y1, Geng LM., *Applied spectroscopy* 2007, 61, 7.

206. C. C. Miller, *Proceedings of the Royal Society of London A: Mathematical, Physical and Engineering Sciences*, 1924, 106, 724-749.

207. I. I. Vlasov, A. A. Shiryaev, T. Rendler, S. Steinert, S.-Y. Lee, D. Antonov, M. Voros, F. Jelezko, A. V. Fisenko, L. F. Semjonova, J. Biskupek, U. Kaiser, O. I.

Lebedev, I. Sildos, P. R. Hemmer, V. I. Konov, A. Gali and J. Wrachtrup, *Nat Nano*, 2014, 9, 54-58.

208. S. L. Zulli, J. M. Kovaleski, X. R. Zhu, J. M. Harris and M. J. Wirth, *Analytical Chemistry*, 1994, 66, 1708-1712.
209. D. C.-Y. Lai, *Thermodynamics & Catalysis*, 2013, 5, e124.
210. J. M. Thomas, *Angewandte Chemie International Edition*, 2009, 48, 3390-3391.
211. C. Martínez and A. Corma, *Coordination Chemistry Reviews*, 2011, 255, 1558-1580.
212. A. Corma and H. García, *Chemical Reviews*, 2003, 103, 4307-4366.
213. R. J. White, R. Luque, V. L. Budarin, J. H. Clark and D. J. Macquarrie, *Chemical Society Reviews*, 2009, 38, 481-494.
214. K. Kageyama and J.-i. Tamazawa, *Science*, 1999, 285, 2113.
215. T. Maschmeyer, F. Rey, G. Sankar and J. M. Thomas, *Nature*, 1995, 378, 159-162.
216. C. M. Crudden, M. Sateesh and R. Lewis, *Journal of the American Chemical Society*, 2005, 127, 10045-10050.
217. G. Ma, X. Yan, Y. Li, L. Xiao, Z. Huang, Y. Lu and J. Fan, *Journal of the American Chemical Society*, 2010, 132, 9596-9597.
218. G. Prieto, J. Zečević, H. Friedrich, K. P. de Jong and P. E. de Jongh, *Nat Mater*, 2013, 12, 34-39.
219. X. Chu, C. Wang, L. Guo, Y. Chi, X. Gao and X. Yang, *Journal of Chemistry*, 2015, 2015, 7.
220. D. Shen, L. Chen, J. Yang, R. Zhang, Y. Wei, X. Li, W. Li, Z. Sun, H. Zhu, A. M. Abdullah, A. Al-Enizi, A. A. Elzatahry, F. Zhang and D. Zhao, *ACS Applied Materials & Interfaces*, 2015, 7, 17450-17459.
221. A. Fukuoka and P. L. Dhepe, *The Chemical Record*, 2009, 9, 224-235.
222. M. Kruk, M. Jaroniec, C. H. Ko and R. Ryoo, *Chemistry of Materials*, 2000, 12, 1961-1968.
223. S. Schünemann, G. Dodekatos and H. Tüysüz, *Chemistry of Materials*, 2015, 27, 7743-7750.
224. J. D. Webb, S. MacQuarrie, K. McEleney and C. M. Crudden, *Journal of Catalysis*, 2007, 252, 97-109.
225. F. Gritti and G. Guiochon, *Journal of Chromatography A*, 2005, 1099, 1-42.
226. J. Staahlberg and M. Almgren, *Analytical Chemistry*, 1985, 57, 817-821.
227. J. W. Carr and J. M. Harris, *Analytical Chemistry*, 1987, 59, 2546-2550.
228. S. Nigam, M. Stephens, A. de Juan and S. C. Rutan, *Analytical Chemistry*, 2001, 73, 290-297.

229. R. A. Shalliker, B. S. Broyles and G. Guiochon, *Analytical Chemistry*, 2000, 72, 323-332.

230. K. M. Shakesheff, M. C. Davies, D. E. Jackson, C. J. Roberts, S. J. B. Tendler, V. A. Brown, R. C. Watson, D. A. Barrett and P. N. Shaw, *Surface Science*, 1994, 304, L393-L399.

231. R. Langer and N. A. Peppas, *AIChE Journal*, 2003, 49, 2990-3006.

232. H. Masuda and K. Fukuda, *science*, 1995, 268, 1466-1468.

233. W. Lee, R. Ji, U. Gösele and K. Nielsch, *Nature materials*, 2006, 5, 741-747.

234. L. Sedel, *Clinical orthopaedics and related research*, 2000, 379, 48-54.

235. K. E. L. Flamme, G. Mor, D. Gong, T. L. Tempa, V. A. Fusaro, C. A. Grimes and T. A. Desai, *Diabetes technology & therapeutics*, 2005, 7, 684-694.

236. A. Angelescu, I. Kleps, M. Mihaela, M. Simion, T. Neghina, S. Petrescu, N. Moldovan, C. Paduraru and A. Raducanu, *Reviews on Advanced Materials Science*, 2003, 5, 440-449.

237. E. J. Anglin, L. Cheng, W. R. Freeman and M. J. Sailor, *Advanced drug delivery reviews*, 2008, 60, 1266-1277.

238. P. Yang, S. Gai and J. Lin, *Chemical Society Reviews*, 2012, 41, 3679-3698.

239. I. Brigger, C. Dubernet and P. Couvreur, *Advanced drug delivery reviews*, 2012, 64, 24-36.

240. C. Charnay, S. Bégu, C. Tourné-Péteilh, L. Nicole, D. Lerner and J.-M. Devoisselle, *European Journal of Pharmaceutics and Biopharmaceutics*, 2004, 57, 533-540.

241. L. Vaccari, D. Canton, N. Zaffaroni, R. Villa, M. Tormen and E. di Fabrizio, *Microelectronic Engineering*, 2006, 83, 1598-1601.

242. A. S.-W. Goh, A. Y.-F. Chung, R. H.-G. Lo, T.-N. Lau, S. W.-K. Yu, M. Chng, S. Satchithanantham, S. L.-E. Loong, D. C.-E. Ng and B.-C. Lim, *International Journal of Radiation Oncology* Biology* Physics*, 2007, 67, 786-792.

243. S. Conner, S. Diettrich, A. Goh, R. Lo, T. Lau, B. Lim and P. Chow, 2006.

244. D. Gong, V. Yadavalli, M. Paulose, M. Pishko and C. A. Grimes, *Biomedical Microdevices*, 2003, 5, 75-80.

245. K. C. Popat, M. Eltgroth, T. J. LaTempa, C. A. Grimes and T. A. Desai, *Biomaterials*, 2007, 28, 4880-4888.

246. H. Hillebrenner, F. Buyukserin, M. Kang, M. O. Mota, J. D. Stewart and C. R. Martin, *Journal of the American Chemical Society*, 2006, 128, 4236-4237.

247. J. Yu, X. Bai, J. Suh, S. B. Lee and S. J. Son, *Journal of the American Chemical Society*, 2009, 131, 15574-15575.

248. Y.-L. Zhao, Z. Li, S. Kabehie, Y. Y. Botros, J. F. Stoddart and J. I. Zink, *Journal of the American Chemical Society*, 2010, 132, 13016-13025.

249. C. S. Brumaru, 2013.

250. Y. A. Skvortsova, *Theses and Dissertations*, 2009, 436.

251. P. J. Meier and B. Stieger, *Annual review of physiology*, 2002, 64, 635-661.

252. Y. Liu and K. Wang, *Thermodynamics of Resulting Complexes Between Cyclodextrins and Bile Salts*, INTECH Open Access Publisher, 2012.

253. R. Bowen, 2001.

254. D. C. Dong and M. A. Winnik, *Photochemistry and Photobiology*, 1982, 35, 17-21.

255. K. Ananthapadmanabhan, E. Goddard, N. Turro and P. Kuo, *Langmuir*, 1985, 1, 352-355.